
Doctoral Dissertations

Student Theses and Dissertations

Spring 2024

The Science of Gravitational-Wave Sources and Beyond Compact Binary Coalescences

Yanyan Zheng

Missouri University of Science and Technology

Follow this and additional works at: https://scholarsmine.mst.edu/doctoral_dissertations



Part of the [Physics Commons](#)

Department: **Physics**

Recommended Citation

Zheng, Yanyan, "The Science of Gravitational-Wave Sources and Beyond Compact Binary Coalescences" (2024). *Doctoral Dissertations*. 3301.

https://scholarsmine.mst.edu/doctoral_dissertations/3301

This thesis is brought to you by Scholars' Mine, a service of the Missouri S&T Library and Learning Resources. This work is protected by U. S. Copyright Law. Unauthorized use including reproduction for redistribution requires the permission of the copyright holder. For more information, please contact scholarsmine@mst.edu.

THE SCIENCE OF GRAVITATIONAL-WAVE SOURCES AND BEYOND COMPACT
BINARY COALESCENCES

by

YANYAN ZHENG

A DISSERTATION

Presented to the Graduate Faculty of the

MISSOURI UNIVERSITY OF SCIENCE AND TECHNOLOGY

In Partial Fulfillment of the Requirements for the Degree

DOCTOR OF PHILOSOPHY

in

PHYSICS

2023

Approved by:

Marco Cavaglià, Advisor

Daniel Fischer

Soma Mukherjee

Shun Saito

Thomas Vojta

Copyright 2023
YANYAN ZHENG
All Rights Reserved

ABSTRACT

This work focuses on the field of gravitational-wave astronomy by extending the scope of detectable sources beyond compact binary coalescences. All the gravitational-wave detections so far come from compact binary coalescences. Focusing on core-collapse supernovae as promising sources for short gravitational-wave transients, this work reports optically targeted searches for gravitational-wave emitted by core-collapse supernovae during the third observing run of the LIGO and Virgo detectors. It also predicts the search sensitivity for the ongoing fourth and forthcoming fifth observing runs. Moreover, the work introduces a novel computational framework for testing the spatial distribution of binary black hole sources, allowing for the exploration of their isotropic or potentially anisotropic distribution. This comprehensive study enhances the understanding of core-collapse supernovae as sources of gravitational-waves and offers new insights into the spatial distribution of gravitational wave events relative to the large-scale structure of the universe.

ACKNOWLEDGMENTS

As a child gazing up at the starry sky, I was curious about the dwelling places of the stars. Time flies and now I find myself approaching the end of my doctoral journey. As I look back, I am grateful for all the encounters that life has brought my way.

I am deeply thankful to my advisor, Dr. Marco Cavaglia, for introducing me to the world of gravitational waves. I express my sincere appreciation for his constant support and mentorship. I gained a wealth of knowledge from him through this journey.

I met with Dr. Marek Szczepańczyk at the beginning of my research studies and our collaboration has persisted since then. I express my gratitude for his help which is not limited to the core-collapse supernova work. I am thankful to Dr. Marie-Anne Bizouard, Dr. Jade Powell, and the entire team at the LIGO supernova group for their trust and support.

I am grateful to all my co-authors for their help in the work of testing binary black hole merger distributions. This work has been a significant learning experience for me.

Furthermore, I extend my sincere thanks to all my collaborators for their aid and support. I made great friendships in the LIGO-MST group. LIGO burst group has provided significant insights into identifying burst-like signals. Members of the LIGO Detchar group help enhance my understanding of LIGO data. My horizons were broadened by the people I met in the IPAM program.

I am grateful to Dr. Zhangjin Chen for ushering me into the academic. I can not reach this point without his constant encouragement and help. My deepest thanks go to my parents, Qinkui Zheng and Fengxia Zhang, my brother Yanzhen Zheng, and my beloved cat, Jiujiu Zheng, for their enduring love.



TABLE OF CONTENTS

	Page
ABSTRACT	iii
ACKNOWLEDGMENTS	iv
LIST OF ILLUSTRATIONS	x
LIST OF TABLES	xiv
LIST OF ABBREVIATIONS	xv
 SECTION	
1. INTRODUCTION	1
2. GRAVITATIONAL WAVES: A BRIEF INTRODUCTION	4
2.1. OVERVIEW OF GRAVITATIONAL WAVE DERIVATION	4
2.2. INTERACTION OF GRAVITATIONAL WAVES WITH TEST MASSES ..	7
2.3. ASTROPHYSICAL SOURCES OF GRAVITATIONAL WAVES	9
2.3.1. Compact Binary Coalescence	9
2.3.2. GW Bursts	10
2.4. THE GROUND-BASED DETECTORS	11
2.4.1. Detecting GW	13
2.4.2. Antenna Pattern	13
3. DETECTOR CHARACTERIZATION	16
3.1. NOISE CHALLENGES	16
3.2. SOURCES OF NOISE	18
3.2.1. Seismic Noise	19
3.2.2. Thermal Noise	19
3.2.3. Shot Noise	20

3.3.	DETECTOR CHARACTERIZATION	20
3.3.1.	Data Quality Shifts	23
3.3.2.	Event Validation	25
3.3.3.	Data Quality Flag.....	26
3.4.	FALSE ALARM RATE	28
3.5.	THE ROLE OF FALSE ALARM RATE IN GW SEARCHES.....	29
3.6.	ORIGINAL CONTRIBUTION	32
4.	OVERVIEW OF CORE-COLLAPSE SUPERNOVAE	33
4.1.	FORMATION OF CCSNE	33
4.2.	EXPLOSION MECHANISM	35
4.2.1.	Neutrino-driven Explosion.....	35
4.2.2.	MHD-driven Explosions	36
4.3.	GRAVITATIONAL-WAVES EMITTED FROM CORE-COLLAPSE SUPERNOVES	38
4.3.1.	GW Amplitude	38
4.3.2.	GW Energy	39
4.4.	MULTIMESSAGENER ASTRONOMY OF CORE-COLLAPSE SUPERNOVAE	40
4.4.1.	EM Emissions	43
4.4.2.	Neutrino Emissions.....	44
4.5.	SEARCH FOR GWS FROM CCSNE.....	44
4.5.1.	On-source Window	45
4.5.2.	Coherent WaveBurst.....	47
5.	SEARCH FOR GWS EMITTED FROM CORE-COLLAPSE SUPERNOVAE DURING O3 RUN	50
5.1.	TARGETED CORE-COLLAPSE SUPERNOVAE.....	51
5.1.1.	Source Selection	51

5.1.2.	On-source Window	53
5.1.2.1.	Method 1 - the early observation	54
5.1.2.2.	Method 2 - the quartic interpolation	54
5.1.2.3.	Method 3 - the physics-Based	55
5.2.	METHODOLOGY	55
5.2.1.	Data	55
5.2.2.	Coherent WaveBurst	56
5.2.3.	Search Sensitivity	57
5.2.3.1.	Neutrino-driven explosions	58
5.2.3.2.	Magnetorotational explosions	59
5.2.3.3.	Black hole formation	60
5.2.3.4.	QCD phase transition	60
5.2.3.5.	Extreme supernova models	60
5.2.3.6.	<i>Ad-hoc</i> signals	62
5.3.	SEARCH RESULTS	62
5.3.1.	SN 2020fqv Loudest Event	62
5.3.2.	Detection Efficiency vs Distance	64
5.4.	CCSN ENGINE CONSTRAINTS	67
5.4.1.	Upper Limits On GW Energy And Luminosity	67
5.4.2.	Upper Limits On PNS Ellipticity	68
5.4.3.	Model Exclusion Statements	71
5.4.4.	Ellipticity Constraints For The Bar Model	73
5.5.	SUMMARY AND DISCUSSION	74
5.6.	ORIGINAL CONTRIBUTION	75
6.	DETECTING GWS FROM THE NEXT GALACTIC CORE-COLLAPSE SUPERNOVA IN THE ADVANCED DETECTOR ERA	77

6.1. CCSN MODELS	79
6.2. GWS CALCULATION	80
6.2.1. Energy And Spectra Of GW Signals	82
6.2.2. Characteristic Strains	85
6.3. NOISE RESCALING	85
6.4. RESULTS FROM SENSITIVITY STUDIES	87
6.4.1. Detection Ranges	88
6.4.2. Minimum Detectable SNR	89
6.5. SUMMARY	91
6.6. ORIGINAL CONTRIBUTIONS	93
7. THE ANGULAR POWER SPECTRUM OF GRAVITATIONAL-WAVE TRAN- SIENT SOURCES AS A PROBE OF THE LARGE-SCALE STRUCTURE	94
7.1. SKY LOCALIZATION OF GW EVENTS	96
7.1.1. BAYESTAR	97
7.1.2. Bilby	98
7.2. ANGULAR POWER SPECTRUM	99
7.3. TWO-DIMENSIONAL CORRELATION FUNCTION	100
7.4. METHOD	101
7.4.1. GW Events Selection	102
7.4.2. Synthetic Events Generation	102
7.4.3. Angular Resolution	104
7.5. RESULT	106
7.5.1. Angular Power Spectrum	108
7.5.2. Two-dimension Correlation Function	111
7.6. CONCLUSIONS	113
7.7. ORIGINAL CONTRIBUTION	116

8. CONCLUSIONS 117

REFERENCES 118

VITA 142

LIST OF ILLUSTRATIONS

Figure	Page
2.1. Schematic deformations produced on a ring of freely-falling particles by GWs that are linearly polarized in the “+” (“plus”) and “×” (“cross”) modes. It is modified from [1].	8
2.2. Top: Estimated GW amplitude from GW150914 projected onto Hanford detector. Bottom: The Keplerian effective black hole separation in units of Schwarzschild radii and the effective relative velocity given by the post-Newtonian parameter. Figure is taken from Ref. [2].	9
2.3. Left: the ground-based global detectors. Right schematic showing LIGO’s interferometer. Figure is taken from Caltech/MIT/LIGO Lab.	12
2.4. The relative orientation of the sky and detector frames. Figure is taken from Ref. [3].	14
2.5. Antenna patterns from left to right: F_+ , F_\times and the root square mean value for an interferometer with the two arms aligned to x and y axis. Figure is taken from Ref. [3].	15
3.1. Representative PSD of the three interferometers: LIGO Livingston 4 January 2020 02:53:42 UTC, LIGO Hanford 4 January 2020 18:20:42 UTC, Virgo 9 February 2020 01:16:00 UTC. Figure is taken from Ref. [4].	18
3.2. Noise budget plots for the GW channels of the two LIGO detectors. Figure is taken from Ref. [5].	19
3.3. Example time–frequency spectrograms for a selection of LIGO glitch classes. Figure is taken from Ref. [6].	21
3.4. Top and bottom plot are the observing segments and BNS range evolution of the LIGO and Virgo detectors from the start of O3 run in April 2019 to the end of O3 in March 2020.....	24
3.5. The number of observed events as a function of detection statistic $\hat{\rho}_c$ for GW150914 analysis time. Figure is taken from Ref. [7].	31
4.1. The schematic depiction of the CCSN central engine for the slowly rotating case. Figure is taken from Ref. [8].	37
4.2. Top: GW amplitude of plus mode A_+ [cm], bottom; the characteristic wave strain in the frequency-time domain in a logarithmic scale which is overplotted by the expected peak frequency (black line denoted by “A”). Figure is taken from Ref. [9].	38

4.3. Time evolution of neutrino, GW (thin blue line), and EM (thick black line) signal luminosities for a non-rotating $17 M_{\odot}$ progenitor star. Figure is taken from Ref. [10].	40
4.4. The composite image of supernova 1987A. Figure is taken from Chandra X-ray Observatory.	42
4.5. Top: the three different phases of observing the explosion in the EM regime. Bottom: The early light curves of the two Kepler type II-P supernovae: KSN2011a, KSN2011d. Blue dots are individual Kepler flux measurements with a 30 minute cadence and the red symbols are 6-hour medians. The x axis shows the redshift corrected time since the SBO was estimated from the model fit. Figure is taken from Ref. [11].	46
5.1. Sky locations of CCSNe are analyzed in this section. Figure is taken from Ref. [12].	52
5.2. Visual representation of the on-source windows (see Sec. 5.1.2), the data coverage for each detector, and the detector duty factors (percentage of available data inside the on-source window). Figure is taken from Ref. [12].	54
5.3. SN 2020fqv loudest event with a 2.8σ detection significance. Figure is taken from Ref. [12].	63
5.4. The detection efficiency as a function of distance for SN 2019ejj. Figure is taken from Ref. [12].	66
5.5. The upper limits on the GW energy (E_{GW}) and luminosity (or power, P_{GW}) emitted by a CCSN engine. Figure is taken from Ref. [12].	67
5.6. The upper limits on the PNS ellipticity. Figure is taken from Ref. [12].	70
5.7. Model exclusion probability P_{excl} for long-lasting bar mode instability model. Figure is taken from Ref. [12].	71
5.8. The constraint of the PNS ellipticity for the long-lasting bar model using a population of the CCSNe analyzed in this and the previous [13] search. Figure is taken from Ref. [12].	72
6.1. Color-composite image of SN 2023ixf and its host galaxy M101 taken by the Fred Lawrence Whipple Observatory.	78
6.2. GW energy as a function of peak frequency (maximum of dE_{GW}/df) for 82 analyzed waveforms. Figure is taken from Ref. [14].	83
6.3. Examples of the GW energy evolution. Figure is taken from Ref. [14].	84
6.4. The GW signals from CCSNe are typically broadband with the majority of the energy at higher frequencies. Figure is taken from Ref. [14].	84

6.5.	The projected noise amplitudes of the LIGO, Virgo, and KAGRA detectors for O4 and O5. Figure is taken from Ref. [14].	86
6.6.	Example O2 LIGO Hanford detector sensitivity rescaled to O4 and O5 designs. Figure is taken from Ref. [14].	86
6.7.	Detection efficiency curves for example waveforms are presented in panels (a) and (b). Panel (c) shows the distances at 10%, 50% and 90% detection efficiencies for all waveforms analyzed. Figure is taken from Ref. [14].	89
6.8.	Detection efficiency curves as a function of injected SNR (SNR_{inj}) for example waveforms are presented in panels (a) and (b). Panel (c) shows the SNRs at 10%, 50% and 90% detection efficiencies. Figure is taken from Ref. [14].	90
7.1.	This image is a graphic of masses of announced GW detections and black holes and neutron stars previously constrained through electromagnetic observations. This version contains all events through the end of O3 with $p_{astro} > 0.5$. Figure is taken from Ref. LIGO-Virgo / Aaron Geller / Northwestern University.	95
7.2.	The astrophysical BBH primary mass (top left panel) and mass ratio (top right panel) distributions for the fiducial textttPP model, showing the differential merger rate as a function of primary mass or mass ratio. The bottom left panel shows the distributions of component spin magnitudes. The bottom right panel shows the constraints on the evolution of the BBH merger rate. Figure is taken from Ref. [15]	103
7.3.	Flowchart of the pipeline used for the generation of the synthetic data sets that are used for the comparison with the observed power spectrum.	105
7.4.	The distribution of sky localization area at 90% contour level from the observed events (left) and synthetic events (right). The red curve shows the gamma distribution by fitting the sky localization area.	106
7.5.	Combined sky localization map of the O3 BBH events considered in the analysis. The sky localization of each event is generated with BAYESTAR [16] from the PE posterior samples for the declination and the right ascension. The map is created with the HEALPY package [17, 18]. Figure is taken from Ref. [19].	107
7.6.	Combined sky localization maps from four synthetic sets. Each set contains 34 synthetic events.	107
7.7.	Combined sky localization map of all 3400 synthetic events that are used to build the fiducial power spectrum. Their isotropic distribution in the sky is shown by the map. Figure is taken from Ref. [19].	108

7.8. The plot shows the observed power spectrum of O3 BBH events (blue curve) considered in the analysis and 100 sets of synthetic events (other colors) under the isotropic hypothesis.	109
7.9. The plot shows the observed power spectrum of the O3 BBH events (red curve) and the fiducial power spectrum obtained from the 100 synthetic sets under the isotropic hypothesis (black curve). The gray-filled regions denote $1 - 3\sigma$ deviations from the mean. Figure is taken from Ref. [19].	109
7.10. An example distribution from one of the C_l for the 100 synthetic sets ($l = 14$). .	111
7.11. The cumulative distribution of observed p-values for the C_l . The black solid line indicates the expected distribution under the isotropic hypothesis. The gray-filled regions correspond to $1 - 3\sigma$ deviations from the expected distribution. Figure is taken from Ref. [19].	112
7.12. The observed correlation function of the O3 BBH events (blue curve) and the 100 set of synthetic events (other colors).	113
7.13. The observed correlation function of the O3 BBH events (red curve) and the fiducial correlation function under the isotropic hypothesis (black curve). The gray-filled regions denote $1 - 3\sigma$ deviations from the mean. Figure is taken from Ref.[19].	114
7.14. The cumulative distribution of observed p-values for the CF. The black solid line indicates the expected distribution under the isotropic hypothesis. The gray-filled regions correspond to $1 - 3\sigma$ deviations from the expected distribution.	115
7.15. The distribution of the CF slope at minimum angular resolution $\theta_{\text{res},s}$ for 100 synthetic sets. The red curve is a gamma distribution to fit. The black dashed line indicates the slope computed from the observed events.	115

LIST OF TABLES

Table	Page
5.1. CCSNe selected as optical targets for the GW search described in this section. Δt is the OSW duration. The last column shows coincident data durations T_{coinc} together with duty factors ($T_{\text{coinc}}/\Delta t$).	51
5.2. List of the loudest events for each CCSN.	62
5.3. Distance (in kpc) of the 50% detection efficiency reached for each CCSN with neutrino-driven explosions, magnetorotational explosions (signal_O), black hole formation (s40), and phase transitions (s50) models. Values in bold represent the farthest distance reached for each model. Mark '-' means that the detection efficiency did not reach 50%.	65
7.1. List of selected GW events.....	102

LIST OF ABBREVIATIONS

- BBH Binary black hole. 1
- BNS Binary neutron star. 1
- CBC Compact binary coalescence. 1
- CCSNe Core collapse supernovae. 1
- CMB Cosmic microwave background. 3
- Detchar Detector characterization. 16
- DQ Data quality. 16
- DQR Data quality report. 25
- EM Electromagnetic. 10
- ETG Event Trigger Generator. 27
- FAR False alarm rate. 28
- GR General theory of relativity. 1
- GraceDB Gravitational-Wave Candidate Event Database. 25
- GRBs Gamma ray bursts. 10
- GWs Gravitational-waves. 1
- Hveto Hierarchical veto. 22
- LIGO Laser Interferometer Gravitational-wave Observatory. 1

- LSS Large Scale Structure. 1
- LVAAlert LIGO-Virgo alert system. 25
- OSW On-source window. 45
- PNS Proto-neutron star. 35
- PSD Power spectral density. 16
- SASI Standing accretion shock instabilities. 36
- SBO Shock Breakout. 41
- SNR Signal-to-noise ratio. 2
- SR Special theory of relativity. 4
- UPV Used Percentage Veto. 22
- VET Veto Evaluation Tool. 27

1. INTRODUCTION

Over a century ago, Einstein's general relativity (GR) predicted the existence of gravitational-waves (GWs) [20]. At that time, even Einstein doubted these ripples in space time would ever be measurable. However, this was changed on September 14, 2015. The Laser Interferometer Gravitational-Wave Observatory (LIGO) [21] and Virgo [22] made the first direct detection of a GW emitted from a pair of black hole merger [23]. In August 2017, the discovery of a binary neutron star (BNS) in both GW and electromagnetic spectra [24] began the era of multimessenger astronomy with GWs. The first, second, and third observing runs (O1, O2, and O3) of LIGO and Virgo brought a wealth of binary coalescence discoveries [25, 26]. Now LIGO and Virgo's fourth observing run (O4) are undergoing. More GW detections are being detected with the detector upgrades. Currently, all detected sources are compact binary coalescences (CBC).

The future of GW detection is poised to advance along two main trajectories. First, we expect to detect GWs from other astrophysical sources beyond CBC. Second, we anticipate a growing number of detections from CBCs. In the former case, core-collapse supernovae (CCSNe) stand out as one of the most promising sources for short transient GW signals. In the case of the latter, the increasing number of CBC detections will provide a more robust foundation for studying the large-scale structure (LSS) of the universe.

Given these two anticipated trends, the dissertation seeks to not only extend our current understanding of detectable GW sources beyond binary black holes (BBH) mergers and BNS mergers but also to explore the LSS of the universe through the current CBC detections.

This dissertation reports on the optically targeted searches for GWs emitted by CCSNe during LIGO and Virgo's O3 run. Additionally, the study predicted the sensitivity of these searches in the ongoing O4 run and the future O5 run. Beyond this, the dissertation introduces novel computational methods for probing the spatial distribution of BBH sources, allowing for robust tests of their isotropic or potentially anisotropic nature.

The dissertation is organized as follows: Section Two gives a brief overview of GWs, tracing their origin from solutions of Einstein's field equations to their interactions with test masses. The section also briefly outlines various sources of GWs beyond CBC and introduces ground-based GW detectors. Moving on to the challenges of detection, Section Three focuses on detector characterization. Given that the detectors are highly sensitive, the GW signals are often buried in noise. Data quality becomes a pivotal concern for GW searches. This section presents three methodologies to address the noise challenges and discusses the concept of false alarm rate.

Section Four focuses on CCSNe, which is identified as a promising source of GWs. This section describes the CCSNe formation and different SN explosion mechanisms. The multimessenger astronomy of CCSNe and GW emissions are included. Section Five presents the search results for GWs in coincidence with CCSNe observed optically during the O3 run. Eight CCSNe are included. It also provides generic CCSN engine constraints and those for the extreme emission models. The generic constraints include upper limits on the GW energy, GW luminosity, and PNS ellipticity. In Section Six, the focus shifts to assessing the search sensitivities for a range of CCSN models in the ongoing O4 and future O5 runs. The section outlines the expected detection ranges and minimum detectable signal-to-noise ratio (SNR).

Additionally, the increasing number of BBH detections has raised questions about the spatial distribution of GW sources and their relationship to the universe's LSS. Section Seven introduces a new, simulation-based inference technique for testing this spatial distribution. Drawing from methodologies used in the study of cosmic microwave background radiation

(CMB), this section discusses how to compute the angular power spectrum of GW events. This method is applied to check if the BBH events are distributed isotropically. Section Eight serves as the conclusion, providing a comprehensive summary of the key findings, methodologies, and contributions presented throughout the dissertation.

Some sections in this dissertation build upon previous research papers. Here are the details:

- Section Three builds upon the research presented in the paper by Y. Zheng et al., titled “A Needle in (Many) Haystacks: Using the False Alarm Rate to Sift Gravitational Waves from Noise,” published in *Significance*, vol. 18, no. 1, 2021.
- Section Five is based on the research carried out by myself and colleagues, reported in the paper titled “An Optically Targeted Search for Gravitational Waves Emitted by Core-Collapse Supernovae during the Third Observing Run of Advanced LIGO and Advanced Virgo,” available as an arXiv preprint, arXiv:2305.16146, 2023.
- Section Six is built on the collaborative work with M. Szczepańczyk and others, reported in the paper “Detecting and Reconstructing Gravitational Waves from the Next Galactic Core-Collapse Supernova in the Advanced Detector Era,” published in *Physical Review D*, 104(10), 102002, 2021.
- Section Seven is based on the paper co-authored by Y. Zheng and others, titled “The Angular Power Spectrum of Gravitational-Wave Transient Sources as a Probe of the Large-Scale Structure,” published in *Physical Review Letters*, 131, 171403.

This dissertation is partially supported by the U.S. National Science Foundation (NSF) through awards PHY-1921006, PHY-2011334, and PHY-2308693.

2. GRAVITATIONAL WAVES: A BRIEF INTRODUCTION

“Spacetime tells matter how to move; matter tells spacetime how to curve”, said John Wheeler (Misner et al., 1973), which aptly described the essence of Einstein’s theory of GR. Before the advancements by Einstein, gravity was described by Newton as an attractive force between masses, diminishing with the square of the distance separating them. Einstein’s insights expanded upon this foundation, accounting for interactions at high speeds and within intense gravitational fields. In 1905, Einstein’s special relativity (SR) revolutionized our understanding that space and time are interchangeable, giving rise to the concept of space-time. A decade later, in 1915, he further developed this into GR, portraying gravity as an intrinsic property of the curvature of spacetime. The curvature of spacetime is shaped by the distribution of mass and energy within it. Meanwhile, it influences the motion of objects, manifesting what we commonly understand as gravity. GWs emerge as ripples or perturbations in spacetime curvature. GWs are generated by the acceleration of massive objects, such as merging black holes or neutron stars. Once generated, these waves propagate through spacetime at the speed of light. As a GW traverses through space, it induces distortions proportional to its amplitude. While I touch upon the derivation of GWs as the solution to the field equation in the subsequent sections, a comprehensive discussion can be accessed in (Maggiore, 2008).

2.1. OVERVIEW OF GRAVITATIONAL WAVE DERIVATION

GWs are predicted from Einstein’s gravitational field equation. This seminal equation describes the dynamics of how matter and energy interact with and influence the curvature of spacetime. In its mathematical representation, the field equation is expressed as:

$$R_{\mu\nu} - \frac{1}{2}g_{\mu\nu}R = \frac{8\pi G}{c^4}T_{\mu\nu}. \quad (2.1)$$

Here, G is Newton's universal gravitational constant and c is the speed of light in the vacuum. $g_{\mu\nu}$ is the metric tensor for curved spacetime. $R_{\mu\nu}$ is the Ricci tensor and R is the Ricci scalar. $T_{\mu\nu}$ is the energy-momentum tensor of matter. It describes the distribution and flow of energy, momentum, and stress in spacetime, thereby conveying the dynamical properties of matter and fields present. The details and derivation of this field equation are extensively covered in the literature, particularly in (Misner et al., 1973).

When the observer is sufficiently far from a specific source, and in regions where spacetime approximates flatness, the metric tensor $g_{\mu\nu}$ can be decomposed as

$$g_{\mu\nu} = \eta_{\mu\nu} + h_{\mu\nu}, \quad |h_{\mu\nu}| \ll 1. \quad (2.2)$$

Here, $\eta_{\mu\nu}$ represents the metric of flat spacetime, and $h_{\mu\nu}$ is the small perturbation describing the deviations in the geometry of flat spacetime induced due to matter distribution $T_{\mu\nu}$.

In the weak gravitational fields, by defining

$$\bar{h}_{\mu\nu} = h_{\mu\nu} - \frac{1}{2}\eta^{\mu\nu}h. \quad (2.3)$$

where $h = \eta^{\mu\nu}h_{\mu\nu}$ represents the trace of the perturbation $h_{\mu\nu}$ with respect to the flat spacetime metric $\eta^{\mu\nu}$, Eq. 2.1 can be simplified by selecting the Lorentz gauge:

$$\square \bar{h}_{\mu\nu} = -\frac{16\pi G}{c^4}T_{\mu\nu}. \quad (2.4)$$

In Vacuum, the energy-momentum tensor $T_{\mu\nu}$ is zero. Eq. 2.4 takes the form:

$$\square \bar{h}_{\mu\nu} = 0. \quad (2.5)$$

With a suitable choice of gauge (the TT gauge), a plane-wave solution of Eq. 2.5 propagating in the $\hat{\mathbf{n}}$ direction can be written as

$$h_{ij}^{TT} = e_{ij}(\mathbf{k})e^{ikx}. \quad (2.6)$$

where $k^\mu = (\omega/c, \mathbf{k})$ is the wave vector and $\mathbf{k} = |\mathbf{k}|\hat{\mathbf{n}}$. The tensor e_{ij} is called the polarization tensor. Eq. 2.6 shows the non-zero components of h_{ij}^{TT} are in the plane that is perpendicular to $\hat{\mathbf{n}}$. For specificity, let's select $\hat{\mathbf{n}}$ along with the z-axis. With our choice of gauge, h_{ij} is both symmetric and traceless. The metric perturbation can be represented as

$$h_{ij}^{TT}(t, z) = \begin{pmatrix} h_+ & h_\times \\ h_\times & -h_+ \end{pmatrix}_{ij} \cos[\omega(t - z/c) + \phi_0].$$

Here, $i, j = 1, 2$ denote indices confined to the transverse (x, y) plane. ϕ_0 is the phase. The quantities h_+ and h_\times are defined as the amplitudes associated with the plus and cross polarizations of the GW, respectively.

Einstein demonstrated that GWs are generated by the dynamic variations of the quadrupole (and higher) momentum [20]:

$$h_{ij}^{TT}(x^\alpha, t) = \frac{2G}{c^4 r} \frac{\partial^2}{\partial t^2} I_{ij}(t - r/c). \quad (2.7)$$

where the quadrupole moment tensor, I_{ij} , is expressed as:

$$I_{ij} = \int d^3x' \rho(t, \mathbf{x}) (x_i x_j - \frac{1}{3} x^2 \delta_{ij}). \quad (2.8)$$

Here, $\rho(t, \mathbf{x})$ is the mass density of the GW source and r represents the distance from the gravitational source to the observer.

Eq. 2.7 and Eq. 2.8 show that the wave amplitude is directly proportional to the second time derivative of the quadrupole moment of the source. Not all accelerated mass distributions emit GWs. Only accelerated mass distributions that lack spherical and

rotational symmetry emit GWs. Eq. 2.7 and Eq. 2.8 are valid under the assumption that r is much larger than the wavelength of the GW and $T_{\mu\nu}$ must not change very quickly. While these assumptions might seem limiting, Eq. 2.7 and Eq. 2.8 apply to a wide array of sources as long as the wavelength of the GW is much larger than the characteristic size of the emitting source.

2.2. INTERACTION OF GRAVITATIONAL WAVES WITH TEST MASSES

The trajectory of a free-falling test mass in a curved spacetime is described by the geodesics equation:

$$\frac{d^2 x^\mu}{d\tau^2} + \Gamma_{\nu\rho}^\mu \frac{dx^\nu}{d\tau} \frac{dx^\rho}{d\tau} = 0. \quad (2.9)$$

Here, τ is the proper time defined as the time measured by a clock carried along the time-like geodesics and $\Gamma_{\nu\rho}^\mu$ denotes the Christoffel symbols. In the TT gauge, the Christoffel term vanishes. Therefore, if the test masses are stationary at $\tau = 0$, i.e., the four acceleration $d^2 x^\mu / d\tau^2$ is zero, then it remains zero at all times. Given two test masses initially separated by a coordinate distance, they will remain at the same coordinate distance provided that their separation is small with respect to the GW wavelength $\bar{\lambda}$. However, their physical distance may change if a GW is present. The effect of a GW on mass distribution can be illustrated by considering a simple case of a GW propagating along the z direction, and a ring of test masses located in the (x, y) plane.

To study the motion of the test particles in the (x, y) plane, we first consider the + polarization. Then, at $z = 0$ (choosing the origin of time so that $h_{ij}^{\text{TT}} = 0$ at $t = 0$), the metric perturbation due to the GW can be expressed as:

$$h_{ij}^{\text{TT}} = h_+ \sin \omega t \begin{pmatrix} 1 & 0 \\ 0 & -1 \end{pmatrix}. \quad (2.10)$$

where $i, j = 1, 2$ corresponds to the transverse plane. The displacement induced by GW in

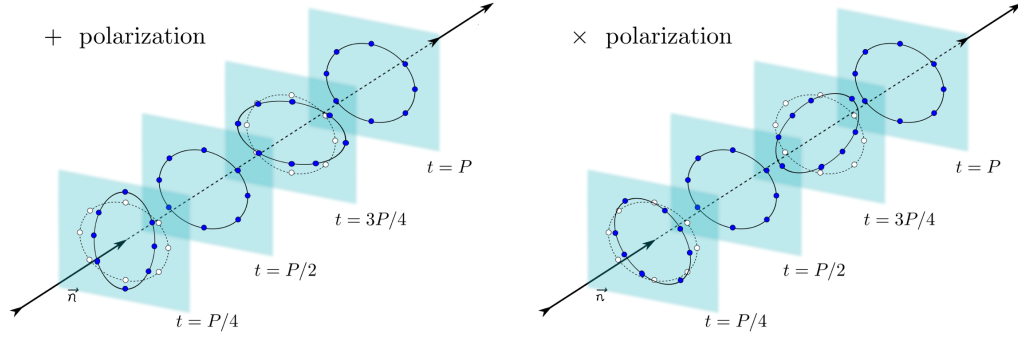


Figure 2.1. Schematic deformations produced on a ring of freely-falling particles by GWs that are linearly polarized in the “+” (“plus”) and “x” (“cross”) modes. It is modified from [1].

the plus polarization is:

$$\begin{aligned}\delta x(t) &= \frac{h_+}{2} x_0 \sin \omega t, \\ \delta y(t) &= -\frac{h_+}{2} y_0 \sin \omega t.\end{aligned}\tag{2.11}$$

Similarly, the displacement resulting from the cross-polarization is:

$$\begin{aligned}\delta x(t) &= \frac{h_+}{2} y_0 \sin \omega t, \\ \delta y(t) &= -\frac{h_+}{2} x_0 \sin \omega t.\end{aligned}\tag{2.12}$$

The effect of the two polarizations on a ring of particles is shown in Figure 2.1. The continuous lines and the dark-filled dots show the positions of the particles at different times, while the dashed lines and the open dots show the unperturbed positions. The positions of a ring of freely falling particles are schematically represented at different fractions of an oscillation period. As the wave propagates along the axis, the ring is deformed.

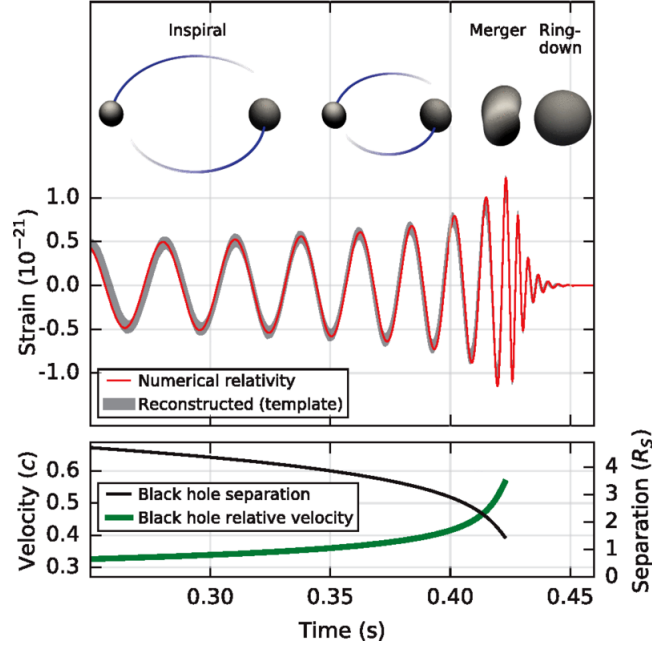


Figure 2.2. Top: Estimated GW amplitude from GW150914 projected onto Hanford detector. Bottom: The Keplerian effective black hole separation in units of Schwarzschild radii and the effective relative velocity given by the post-Newtonian parameter. Figure is taken from Ref. [2].

2.3. ASTROPHYSICAL SOURCES OF GRAVITATIONAL WAVES

The successful detection of GWs has ushered in a new era for both GW research and multi-messenger astronomy. These spacetime perturbations are emitted from some of the most violent and energetic phenomena. The main astrophysical sources of GWs encompass a wide variety of events, each carrying its unique features and consequential insights.

2.3.1. Compact Binary Coalescence. The coalescence of the binary compact objects is the most common source of GW detections so far. The only detected GWs are emitted from the CBC events. A pair of compact objects, black holes or neutron stars, spiral towards one another until they eventually merge. As these compact objects get closer, their orbital radius decreases, and the system releases energy in the form of GWs. As a result, the GW waveform increases in amplitude and frequency with time, producing what is commonly called a “chirp-like signal”.

Since the first detection of GWs from a binary black hole merger [23], LIGO and Virgo have detected more than 100 CBC events [4]. To detect these events, researchers employ the matched-filter technique [27]. This method is a signal processing technique specifically designed for identifying weak signals buried within noisy data. Scientists predict how the waveforms of GWs from CBC events should appear. These waveforms are formed into the waveform template bank and used in the matched-filter method. If the observed data contains a GW signal that matches the waveform in the template bank, it will produce a peak in the SNR, marking a potential GW detection. A typical GW from the CBC event can be seen in Figure 2.2.

2.3.2. GW Bursts. Except for the GWs produced from CBC events, we also expect to detect the GWs from other astrophysical sources. GW bursts are the transient signals derived from the universe’s most energetic phenomena. The progenitors usually coincide with bright and high-energy electromagnetic (EM) counterparts. GW bursts target either the predicted GW sources with poorly modeled waveforms or unknown sources producing GWs that have not yet been predicted. Several anticipated sources are described below.

The core-collapse supernovae are the violent explosions of massive (above $8 M_{\odot}$) stars at the end of their life, giving birth to neutron stars and black holes. During the explosion, GWs, neutrinos, and the electromagnetic spectrum, are emitted. The explosion mechanism of CCSNe is not yet fully understood. GWs emitted from CCSNe carry information about their engine’s dynamics, providing insights into the explosion mechanism. A detailed discussion of CCSNe is presented in Section 4. Gamma-ray bursts (GRBs) are cosmologically sourced, transient emissions of gamma radiation observed more than once daily [28]. These bursts are thought to be powered by highly relativistic jets formed from the interaction of matter with a central compact entity [29]. Magnetars, a variant of neutron stars, possess intensities that can surpass those of their regular counterparts by a thousand-fold. They are postulated to evolve from the remnants of supernovae explo-

sions [30]. Cosmic strings, in turn, represent topological defects reminiscent of vortices in certain condensed matter systems, emerging from spontaneous symmetry-breaking phase transitions.

The GW waveforms emitting from these sources are typically irregular, rendering the modeled search methods that are commonly used for CBC detections ineffective. As a result, we employ the unmodeled search techniques. In these approaches, EM detections serve as triggers, prompting us to investigate the corresponding time window for potential gravitational wave signals in the data.

2.4. THE GROUND-BASED DETECTORS

The design of current GW detectors is based on a modified Michelson interferometer scheme, characterized by their distinctive L-shaped arms. The LIGO laboratory operates two such detectors in the US, one in Livingston, LA, and the other in Hanford, WA. Two additional interferometers are operating worldwide: Virgo, a 3-kilometer interferometer located in Cascina, Italy, and KAGRA, an underground IFO located in the Kamioka mines in Japan. A detector on the model of the LIGO interferometers is currently under construction in India. These observatories form the global network of the detectors, as shown in Figure 2.3. They are commonly referred as the 2nd generation, or advanced detectors. The progression of GW detection has been monumental, and the horizon looks even more promising with the conceptualization of third-generation detectors. Two prime candidates leading the charge in this new era are the Einstein Telescope (ET) and the Cosmic Explorer (CE). The ET proposal calls for an underground detector in Europe with the design of a triangular layout with arms approximately 10 km. CE proposal calls for one or two detectors to be built in the United States with arm lengths that stretch up to 40 km. As detector technology advances, these new generations of detectors will allow us to probe much deeper into the universe and detect GWs from more and more astrophysical sources.

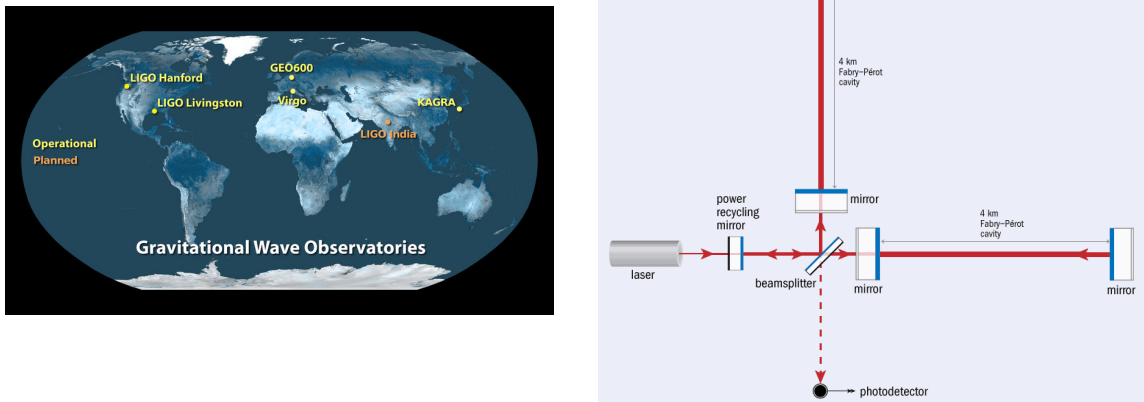


Figure 2.3. Left: the ground-based global detectors. Right schematic showing LIGO's interferometer. Figure is taken from Caltech/MIT/LIGO Lab.

In the standard Michelson interferometer setup, a pre-stabilized laser emits light that hits a beamsplitter, directing half of the light down each arm. After traveling down the arms, the light reflects off mirrors at the arm ends and returns to the beamsplitter. Upon its return, the beamsplitter merges the two light beams. Half of this combined light returns to where it is further injected back into the interferometer, while the other half proceeds to a photodetector. As these light beams merge, they interfere based on any phase discrepancies due to differing optical path lengths in the two arms. If the arms move differentially as when a GW is passing through the detector, the interference pattern changes. This results in alterations in the interference pattern. The photodetector detects these changes, which can then be converted into strain measurements. The GW detectors are typically adjusted to operate near a dark fringe within the interference pattern. Additionally, they incorporate Fabry-Perot cavities within the arms. These cavities feature partially reflective input test masses positioned between the end test masses and the beamsplitter. This configuration results in the light traveling the arm's length approximately 300 times before it returns to the beamsplitter, effectively extending the detector arm's length. It's crucial to ensure that these

arm cavities remain in resonance. This guarantees that the light within an arm undergoes constructive interference, preserving a consistent phase across multiple passes down the arms. A schematic of the interferometer is depicted in Figure 2.3.

2.4.1. Detecting GW. For an L-shaped detector with one arm aligned with the x-axis and the other with the y-axis, the impact of a GW propagating along the z-axis can be described in terms of the motion of the end mirror, derived from the geodesic equation of GR, Eq. 2.13. Assuming the positions of the test mirrors are at $(0, L)$ for one arm and $(L, 0)$ for the other in the unperturbed configuration, a GW with plus polarization approaching the interferometer perpendicularly from the z direction produces the differential strain:

$$\frac{\delta L(t)}{L} = \frac{\delta x(t) - \delta y(t)}{L} \approx h_+(t). \quad (2.13)$$

A significant insight from this relation is that the longer the arms of the interferometer, the smaller the GW strain that can be detected. Kilometer-scale GW detectors such as LIGO, can detect perturbations as small as $h \sim 10^{-21}$, corresponding to absolute displacements on the order of 10^{-18} meters.

2.4.2. Antenna Pattern. Gravitational waves arriving at an interferometer will generally be composed of the plus and cross polarizations and come from a generic direction. The way each polarization affects the detector strain is described in terms of the antenna patterns. For a wave traveling in the direction given by \hat{n} , the induced strain on the detector due to the combined effects of these polarizations can be expressed by:

$$\frac{\delta L}{L} = F_+ h_+(t) + F_\times h_\times. \quad (2.14)$$

In this equation, F_+ and F_\times denote the antenna pattern functions. Eq. 2.14 represents how an interferometer's response to the GW is related to the polarization of the incoming wave and the orientation of the detector.

The antenna pattern can be written as

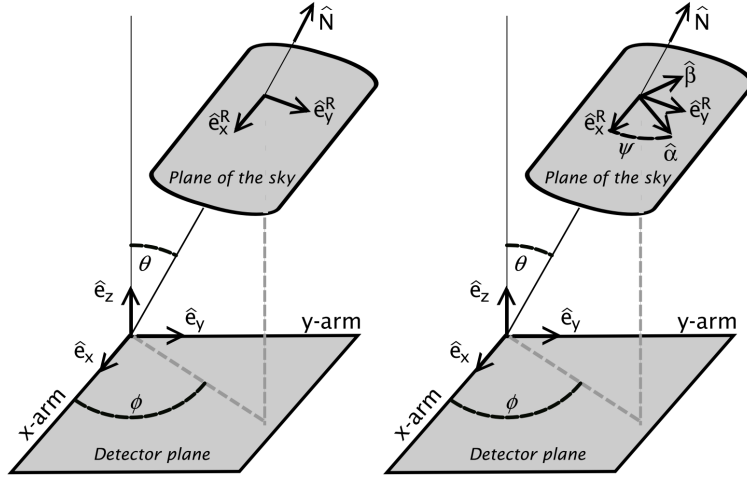


Figure 2.4. The relative orientation of the sky and detector frames. Figure is taken from Ref. [3].

$$\begin{aligned}
 F_+ &= \frac{1}{2} \left(1 + \cos^2 \theta \right) \cos 2\phi \cos 2\psi - \cos \theta \sin 2\phi \sin 2\psi \\
 F_\times &= \frac{1}{2} \left(1 + \cos^2 \theta \right) \cos 2\phi \sin 2\psi + \cos \theta \sin 2\phi \cos 2\psi .
 \end{aligned}
 \tag{2.15}$$

where the polar angles θ and ϕ represent the orientation of the wave with respect to the detector and ψ is the rotation angle in the sky frame, as shown in Figure 2.4. The importance of this mathematical representation becomes evident when considering the Earth's rotation. While the antenna pattern remains static in the detector's frame, its sensitivity to different parts of the sky varies with time due to the Earth's rotation, thus affecting the rate of detections for sources at different sky positions. GW detectors like LIGO, despite their remarkable sensitivity, have regions in the sky to which they are less sensitive, colloquially termed blind spots. For example, for GWs with a + polarization, these blind spots occur at angles $\phi = \pi/4$. In these regions, the gravitational wave induces identical displacements in both the X and Y arms of the interferometer, leading to no relative phase shift and thus no detectable interference pattern. This results in the inability to detect GWs coming from that specific direction. This is graphically illustrated in Figure 2.5, which

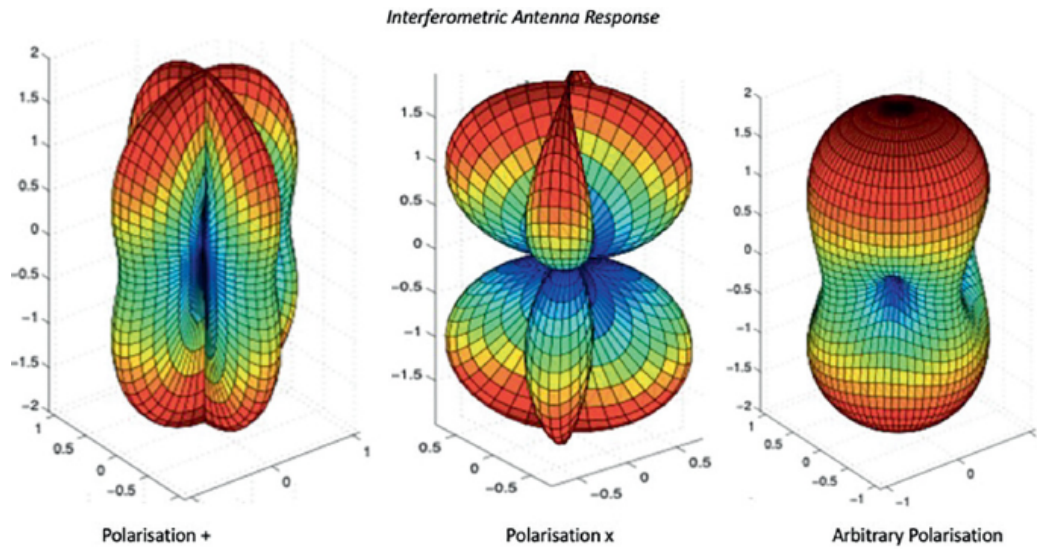


Figure 2.5. Antenna patterns from left to right: F_+ , F_\times and the root square mean value for an interferometer with the two arms aligned to x and y axis. Figure is taken from Ref. [3].

maps out the sensitivity of the LIGO detector to both plus and cross-polarized GWs. The root mean squared antenna pattern showcased in the figure provides an averaged sensitivity profile over various sky positions and polarizations, revealing regions where the detector's sensitivity is diminished.

3. DETECTOR CHARACTERIZATION

As part of my engagement with the LVK collaboration, my contributions to the Detector Characterization (Detchar) group have been active and focused. In this section, I will provide an overview of the Detchar group, detailing its objectives and the tools commonly employed within the group, which are also integral to my research. Subsequently, I will describe my principal activities within Detchar: data quality (DQ) shifts and production of DQ vetoes. Finally, this section will introduce the concept of the false alarm rate, which is an essential metric in GW detection and applied in the following sections.

3.1. NOISE CHALLENGES

GW detectors are designed to detect minuscule changes in differential arm length caused by passing GWs. While designed to detect incredibly faint ripples in spacetime, the same high sensitivity makes them susceptible to an array of non-gravitational signals. These signals can either mimic a GW event or overshadow real signals, making it challenging to differentiate true GW signals from noise. These noises stem from a variety of physical phenomena, ranging from seismic activity to thermal vibrations and electronic fluctuations. Various real-world factors can introduce unpredictable variations in the noise, such as seismic disturbances from daily traffic, nearby trains, earthquakes, or activities like logging. The noise is non-stationary and non-Gaussian distributed in the collected data. Understanding and mitigating these sources of noise are vital for enhancing the reliability and precision of GW detections.

To account for these fluctuations, the power spectral density (PSD) is frequently recalculated over shorter intervals, ensuring it remains relevant to the changing nature of the noise. The time-dependent data in GW detectors can be written in terms of an astrophysical signal and excess noise. Represented as $s(t)$, the data is the sum of the GW

signals $h(t)$, and the noise term $n(t)$:

$$s(t) = h(t) + n(t). \quad (3.1)$$

Given that the noise is inherently stochastic, its ensemble average value over many realizations is zero:

$$\langle n(t) \rangle = \lim_{N \rightarrow \infty} \frac{1}{N} \sum_{i=1}^N n^{(i)}(t) = 0. \quad (3.2)$$

Here $n^{(i)}(t)$ denotes the realization of the noise at the time t and N is the total number of the total number of these realizations.

Similarly, when considering the Fourier transform of the noise, its ensemble average is also zero:

$$\langle \tilde{n}(f) \rangle = \left\langle \int_{-\infty}^{\infty} n(t) e^{-2\pi i f t} dt \right\rangle = \int_{-\infty}^{\infty} \langle n(t) \rangle e^{-2\pi i f t} dt = 0. \quad (3.3)$$

While the noise events are random and unpredictable, their structure can be described by the covariance in the frequency domain. This covariance is captured by the PSD:

$$\langle n(f) \tilde{n}^*(f') \rangle = \frac{1}{2} S_n(|f|) \delta(f - f'). \quad (3.4)$$

where $\delta(f - f')$ is the Dirac delta function, ensuring that the noise at different frequencies is uncorrelated.

The PSD, therefore, serves as an important tool for GW detections, allowing us to discern the nature and characteristics of the noise across different frequency bands. It provides insights into the various noise sources, enabling the development of strategies to mitigate them and improve the sensitivity and accuracy of GW detection. Figure 3.1 shows the PSDs of LIGO Livingston, LIGO Hanford, and Virgo during the third observing run.

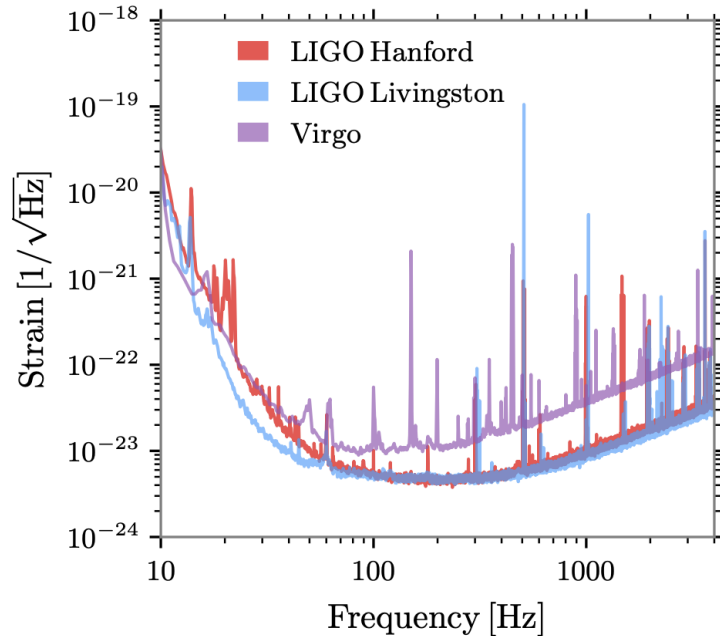


Figure 3.1. Representative PSD of the three interferometers: LIGO Livingston 4 January 2020 02:53:42 UTC, LIGO Hanford 4 January 2020 18:20:42 UTC, Virgo 9 February 2020 01:16:00 UTC. Figure is taken from Ref. [4].

3.2. SOURCES OF NOISE

Instrumental noise in LIGO presents a considerable challenge for the accurate detection and analysis of GWs. This form of noise originates from various sources and can interfere with the signals that the observatory aims to detect. The sources of noise in GW detectors are complex and pervasive. They vary from diverse contributors. The noise sources can be classified into fundamental, technical, and environmental noises. Fundamental noises determine the ultimate design sensitivity of the instrument. These can only be mitigated through major instrument upgrades like installing a new laser or improving optical coatings. Technical noises originate from various system components like electronics, control loops, and charging noise. This kind of noise can be mitigated with investigation. Environmental noises contain seismic activity, acoustic, magnetic noise, and so on

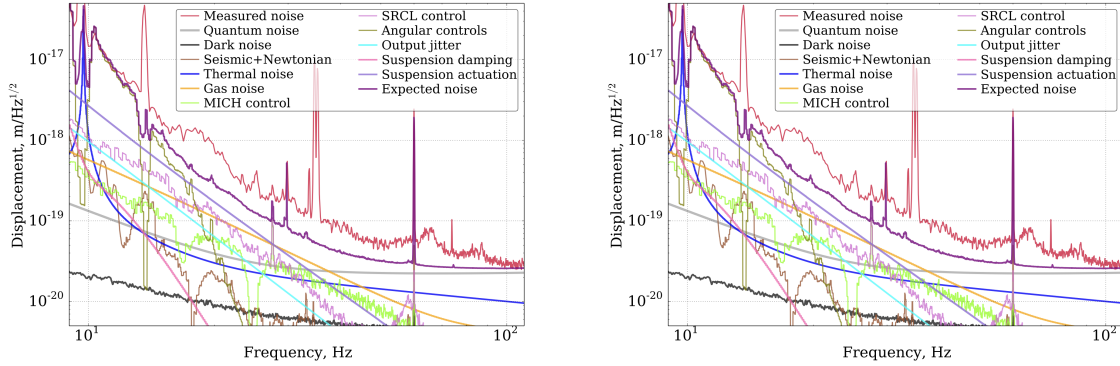


Figure 3.2. Noise budget plots for the GW channels of the two LIGO detectors. Figure is taken from Ref. [5].

[5]. LIGO’s design aims for both technical and environmental noises to have a minimal impact on the GW detection channel when compared to fundamental noises. However, the detector’s sensitivity can be reduced due to unforeseen noise source couplings. Figure 3.2 displays an array of noise sources present in the LIGO detector. The left plot shows the low-frequency curves for L1, whereas the right plot shows the high-frequency curves for the H1 detector. As examples, we discuss the following types of noise.

3.2.1. Seismic Noise. In the lower frequency range, LIGO’s noise primarily arises from terrestrial disturbances that affect the end test masses of the interferometer. Such ground activities induce changes to arm lengths by causing physical displacements of these end test masses. The spectrum of these disturbances is broad, encompassing effects from daily vehicular congestion, and seismic events, to even the subtle oscillations of a fan within the control facility. To counter this seismic noise, a pendulum system designed to stabilize and dampen the movements of the end test masses is implemented.

3.2.2. Thermal Noise. Thermal noise, often termed Brownian noise, arises from the thermal kinetic energy inherent to the detector’s atoms. This molecular Brownian movement within both the end test masses and the suspension wires results in alterations in

the interferometer arm's length. Given that the focus is on spacetime deviations at the scale of sub-atomic particles, this thermal noise significantly affects GW detection sensitivity, especially within the mid-frequency range, spanning from tens to hundreds of Hertz.

3.2.3. Shot Noise. Photons impinge upon the photodiode according to a poisson distribution, a stochastic process inherently subject to statistical fluctuations. This randomness gives rise to noise, stemming from the uncertainties and irregularities associated with counting these individual photons as they arrive at the photodiode. This form of noise is an inherent challenge when working with photon detection systems and can affect the precision of measurements in the high-frequency range.

3.3. DETECTOR CHARACTERIZATION

In addition to the persistent background noise, non-astrophysical disturbances corrupt the detector data with transient noise bursts of different durations, known as *glitches*. Glitches pose a major challenge in detecting and analyzing GW signals. While some of them can be traced back to environmental or instrumental causes, the origins of others remain ambiguous or unidentified. Glitches typically last just a few seconds and significantly contribute to the noise background that impacts GW searches. They can either mimic true GW signals or introduce false positives, complicating the accurate estimation of astrophysical parameters, such as the source's luminosity distance, its position in the sky, and intrinsic source parameters. Figure 3.3 displays examples of common glitches from the specific time-frequency transforms. "Tomte" and "Blip" are both short-duration glitches, distinguished by their morphologies and frequency coverage. "Tomtes" exhibit a characteristic triangular shape, while "Blips" have a tear-drop morphology and span a broader range of frequencies. "Whistle" glitches, on the other hand, are marked by their V, U, or W shapes that sweep through frequencies higher than 128 Hz. "Fast Scattering" glitches, also known as "Crown" glitches, manifest as one or more arch-shaped features, each lasting between 0.2 and 0.3 seconds. In contrast, "Scattered Light" glitches produce

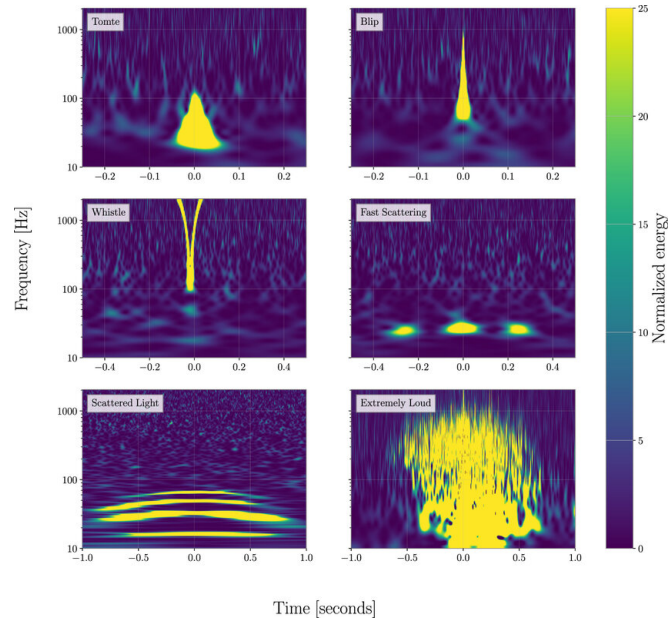


Figure 3.3. Example time–frequency spectrograms for a selection of LIGO glitch classes. Figure is taken from Ref. [6].

longer-duration arches, typically between 2.0 and 2.5 seconds, and these arches can often be seen stacked upon one another. “Extremely Loud” glitches are high-SNR events that result in the saturation of the spectrogram. These glitches manifest with variations in frequency and duration. Pinpointing the origins of these glitches is crucial for enhancing the quality of GW data.

To ensure the accuracy and reliability of data in comparison to what is expected from an ideal GW interferometer, LIGO detectors, and their associated data are subjected to stringent monitoring. This process occurs both before and during observation periods and utilizes numerous supplemental data streams, termed auxiliary channels. These channels record the output of sensors that survey the surrounding environment of the detectors and monitor the detector control systems. In the LIGO system, the two interferometer’s arms define the X and Y arms, and the mirrors act as the sensitive components that react to GWs. The primary interferometer mirrors, situated at the ends of the arms as well as the corner station, reside within Basic Symmetric Chambers. The chambers, combined with the

Horizontal Access Modules and the arms, create an extremely high vacuum environment, crucial for precise measurements. The sensors associated with these structures feed data into the auxiliary channels, aiding in identifying potential noise sources. Strategies can be devised to reduce their impact on GW detection.

However, challenges persist. Ground-based GW detectors, like LIGO, are exposed to diverse environmental noises. Moreover, as they undergo frequent modifications during an observation run and benefit from the periodic introduction of advanced technologies to improve sensitivity, the nature of these detectors remains dynamic. This ever-changing landscape presents ongoing challenges in the realm of noise characterization, as the source, shape, frequency, and intensity of various noise factors are perpetually shifting.

The Detchar team plays a crucial role in identifying and mitigating sources of noise in GW detectors. Operating both remotely and directly on-site at LIGO facilities, they monitor the instruments, tracking the emergence of new noise disturbances.

A variety of tools and methods are developed in Detchar to investigate detector noise and its origin. Omicron [31] serves as the main event trigger generator for Detchar studies, functioning as an unmodeled transient detection pipeline. Specifically, the Omicron pipeline executes a multi-Q transform [32] on a given data stream. Omicron not only refines the understanding of transient noise events but also contributes to more effective noise mitigation strategies. Another of the main data visualization tools is the Omega scans [31, 33, 34]. Omega scans facilitate the identification and visual depiction of glitches through the depiction of their time-frequency morphology associated with various transient noise sources. Furthermore, machine learning algorithms are increasingly being incorporated into the DetChar framework [35].

To ensure DQ and minimize the impact of transient noise, veto algorithms are employed. These algorithms work by identifying and vetoing data that is corrupted by noise. Among these are the Hierarchical Veto (Hveto) [36, 37] and the Used Percentage Veto (UPV) [38]. Hveto computes the correlation of auxiliary channels that is potentially

significant coincidences between Omicron [31] triggers in the GW strain channel. UPV identifies auxiliary channels that exhibit statistical correlation with the GW channel. To gauge this correlation, KleineWelle (KW) triggers [31] are employed. While UPV is adaptable to various trigger generation algorithms, KW is favored due to its accessibility across numerous channels and its relatively swift response time. Both of these algorithms filter out triggers in the GW strain channel. They do this by correlating the triggers from the strain channel with those from auxiliary channels, which are set up to monitor environmental variances.

Beyond the methods highlighted earlier, additional services employ these techniques specifically to improve GW detections. In the following sections, I will provide an overview of two main services in DetChar: DQ shifts and event validations.

3.3.1. Data Quality Shifts. DQ shifts serve as an effective mechanism for monitoring the DQ from the LIGO interferometers. These shifts address both instrument-related aspects and those related to search operations. By employing DQ shifts, weekly feedback can be relayed to on-site commissioners if an event arises that compromises DQ. Detector engineers and data analysts have developed the Detcharsummary pages [39]. Detchar summary pages enable automated daily assessments of the GW strain data as well as multiple interferometer subsystems. This routine analysis helps to continuously monitor the system's performance and identify potential issues in a timely manner.

Two examples of products included in summary pages are shown in Figure 3.4, summary pages provide an illustrative breakdown of the observing segments and the evolution of the binary neutron star range for both LIGO and Virgo during their O3 runs. It is worth noting that there are factors influencing the duty cycle. Environmental factors, such as weather conditions, can play a role.

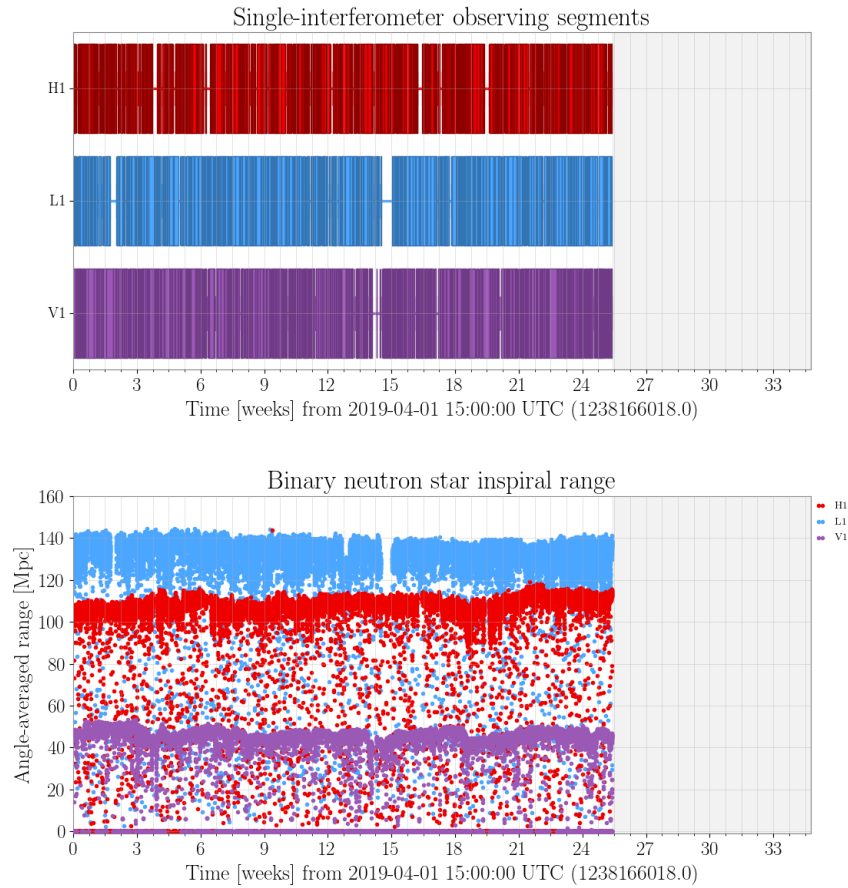


Figure 3.4. Top and bottom plot are the observing segments and BNS range evolution of the LIGO and Virgo detectors from the start of O3 run in April 2019 to the end of O3 in March 2020.

Another significant metric for evaluating the efficacy of a GW detector is the BNS revolution range. This range quantifies the average distance over which a standard binary system, consisting of two neutron stars each with a mass of 1.4 solar units, can be identified with an SNR of 8 and above. The BNS range considers all potential sky locations and inclinations but excludes cosmological adjustments.

More information about both the environment and the instruments can be found on the summary page. Various other DetChar tools, including Hveto and UPV, which were previously mentioned, are also cataloged there. Armed with this comprehensive set of data, the condition of the detectors can be effectively monitored and assessed by the DQ shifts.

Typically, DQ shifts are studies of seven days duration of data from one of the LIGO interferometers undertaken by a designated individual. The individual is expected to study the output of one detector every day to look for DQ changes that may adversely affect a GW search or indicate an instrumental malfunction. The assigned DQ shifter maintains regular communication with the LSC Fellow allocated for that particular shift. Every day, the DQ shifter logs their findings in a DQ Shift Report, which is subsequently shared with the Detchar group shortly after the shift concludes. Daily studies of the interferometer are necessary to promote rapid feedback with commissioners should a significant change occur. The immediacy of daily assessments ensures that any major changes are promptly addressed in coordination with commissioners. To wrap up their duties, the DQ shifter summarizes their most significant observations in an aLOG entry, which gets posted to the relevant site.

During the first observing run, DQ shifts offered invaluable feedback, crucially contributing to the validation process for both GW150914 and GW170817. It also played a significant role during O2 and O3 runs. Given the notable modifications to the instruments post-O3, the relevance of DQ shifts in the O4 run has become even more pronounced.

3.3.2. Event Validation. DetChar also plays a crucial role in the validation of events by distinguishing actual astrophysical GW signals from instrumental artifacts. This service is provided by the event validation team with the tool DQ Report (DQR) [40]. DQR is an internal collection of convenient analysis routines used to support and enable the verification of potential GW event candidates. This system operates seamlessly with both the LIGO-Virgo Alert System (LVAlert) and the Gravitational-Wave Candidate Event Database (GraceDB). Upon the detection of a potential GW signal by the online GW search pipelines, the event gets logged in GraceDB. Subsequently, the LVAlert framework sends notifications

to all its subscribers, inclusive of the DQR system. Upon receiving this notification, the DQR activates a set of analyses executed across three LIGO computing nodes. Some examples of the analyses conducted include omega scans, statistical evaluations such as HVeto, and checks against known DQ flags in the DQ segments database. The structure of the DQR is modular, thereby facilitating the addition of more tools as required.

Within minutes of an automated alert being sent to the Gamma-ray Coordinates Network [41], the DQR system begins uploading web-based summaries and associated data to GraceDB for internal evaluation. A designated individual is tasked with validating the preliminary findings reported by the DQR system. This validation process includes checking the status of the detector, the presence of any noise, and the glitch rate among other factors around the event time. Based on this internal review, decisions are made about whether to issue additional GCN Notices and Circulars or retract a previously declared candidate. If excess noise is found to overlap with the event, additional noise mitigation steps may be necessary.

3.3.3. Data Quality Flag. Low-latency searches are crucial for quickly detecting GW signals, but comprehensive analyses of these events are carried out offline. Moreover, the data is used for various types of searches, making offline DQ vital. To this end, specific time segments or periods tainted by noise or glitches that may render true signals undetectable are flagged. These indicators are known as DQ flags. The purpose of the DQ flag is to flag the sufficiently well-understood noise artifacts from the data so that they can be removed in offline searches.

These flags are generated based on auxiliary channels, which could capture the noise from the instruments and their surrounding environment. They act as an initial safeguard against potential data anomalies. The flags serve to highlight periods that may be affected by instrumental disturbances, thereby alerting researchers to remove periods for their search purpose.

DQ flags capture essential metadata about the conditions and states of each interferometer, including its various subsystems and components. DQ flags are used at all current GW observatories. Each flag in the database corresponds to specific periods, known as segments, during which the flag's status (either on or off) is verified. These segments are defined by clear start and end times, measured in whole seconds.

DQ flags are categorized based on the severity of these disturbances, and each category provides valuable insights into their potential impact on specific types of searches. Generally speaking, a lower category number implies a more severe disturbance. For instance, a flag marked as CBCLOW Category 1 indicates that the data segment in question is significantly compromised, making it unsuitable for analyzing low-mass CBC events. On the other hand, a CBCLOW Category 4 flag suggests a less critical issue. A Category 2 flag is commonly used for GWs from burst transient sources with the unmodeled search method.

To generate the DQ flag, different methods are implemented. The Veto Evaluation Tool (VET) is instrumental in assessing the performance of a DQ flag by analyzing its efficiency, dead time, and utilization against a predefined set of events. To illustrate, the following outlines how the Category 2 flag is generated using VET. The process of identifying and handling glitches in the strain data involves multiple steps. Initially, auxiliary channels are examined to identify potential sources of glitches. Subsequently, Event Trigger Generator (ETG) is employed to isolate noise segments or specific times of noise occurrence. Finally, the VET is utilized to assess whether the identified noisy times are appropriately flagged in the strain data. When employing the VET, it is vital to focus on specific evaluation metrics to ensure effectiveness. The primary metrics commonly used are:

- **Efficiency:** This metric quantifies the proportion of events identified by the ETG that are successfully vetoed.
- **Deadtime:** This measures the fraction of the total analyzed time that is vetoed due to noise events.

Additionally, the composite metric formed by dividing efficiency by deadtime is of particular importance. This ratio serves as a more comprehensive measure of the system's performance, balancing the need to veto as many false events as possible (efficiency) against the desire to minimize the amount of valuable data lost due to vetoes (deadtime). In essence, this composite metric offers a more nuanced view of the trade-offs involved in the veto process, allowing for more informed decisions in optimizing GW detection.

3.4. FALSE ALARM RATE

Even with the advanced techniques and tools mentioned above, it's important to recognize that noise cannot be entirely eradicated from the system. As we delve into the realms of GW searches, this residual noise can pose challenges in distinguishing signals from the background noise. Hence, a critical metric in our GW searches is the false alarm rate (FAR). The FAR helps gauge the noisiness of the background by quantifying how often the system would mistakenly identify noise as a genuine GW event. By continuously monitoring and adjusting for the FAR, we can refine our detection methods and bolster our confidence in the signals we identify as true GW events.

The effect of noise transients on GW searches is mitigated by implementing time-coincident searches between detectors. Because GWs are expected to travel at (or close to) the speed of light, a GW signal must occur in two separate detectors within their light time of flight. Detection candidates that pass the time-coincident check are further ranked according to their statistical significance. The ranking statistic for a GW candidate depends on the search. For example, template-based matched filter searches [42, 43] for modeled GW signals from BBH and BNS mergers rely on SNR and consistency chi-square tests [44]. Unmodeled searches, such as the searches for GW signals from CCSNe, rely on coherence tests of excess power in the detectors. In both modeled and unmodeled searches, the significance of a candidate event with respect to the background is given in terms of the

FAR:

$$\text{FAR} = \frac{N}{T_{\text{BKG}}}. \quad (3.5)$$

where N is the number of background noise events with ranking statistics equal to or above that of the candidate event, and T_{BKG} is the total duration of the background. The duration of the background in a multi-detector search can be increased by time shifting the data of a detector with respect to other detectors in the network by any amount larger than the light travel time between the detectors. The time-shift technique is a standard technique that LIGO has been using since 2005 [45, 46]. Any transient signal event found in time-shifted data must be caused by instrumental or environmental noise. Under the assumption that the detector noise is stationary, the time-shifted background is representative of the time-coincident “zero-lag” detector background and can be used to estimate the FAR of a GW candidate. The smaller the FAR of a candidate event, the less likely the background is expected to produce false events at the given value of the ranking statistic, i.e., the more likely the candidate event is an astrophysical GW signal. The inverse false alarm rate (IFAR) provides another way to measure the significance of the coincident triggers. Typically, a confident detection requires a value of the probability less than 5.8×10^{-7} , corresponding to a 5σ confidence level.

3.5. THE ROLE OF FALSE ALARM RATE IN GW SEARCHES

A template bank containing approximately 250,000 waveforms was used to cover the parameter space of the search that confirmed GW150914 [7, 23]. The SNR distribution of single-detector triggers was then re-weighted with the χ^2 statistic and coincident events were selected by implementing a 15-ms time coincidence test between the LIGO-Handford and LIGO-Livingston observatories. The network ranking statistic was then calculated as a quadrature sum of the individual, re-weighted detector SNRs, resulting in a network SNR of 23.6 [47]. Figure 3.5 shows how the event compares to a search background of 608,000

years from time shifts [7]. Orange markers indicate “zero lag” GW candidates. The black and purple lines denote the background. As the SNR of the event is larger than the SNR of any background event, only a lower bound can be placed on its FAR. The background triggers were divided into three search classes based on their morphology. Thus the FAR of the event is multiplied by a trial factor of three [23], giving a final lower bound for the FAR of 2.7×10^{-7} Hz, or less than 1 in 203,000 years. This translates into a probability larger than 5.1σ with 16 days of analysis time from September 12 to October 20, 2015 [23].

The high-SNR tail of the GW150914 search background in Figure 3.5 (black line) is due to accidental coincidences between GW150914 in one detector and noise in the other detector. The purple line shows the background distribution without the contribution of GW150914. In this case, the second most significant event has a FAR of 1 per 2.3 years [7, 48]. Unmodeled searches [49] build the detection statistic from coherent excess power signatures in the detectors [50, 51]. For example, the ranking statistic of the cWB pipeline is [50, 52]

$$\eta_c = \left[\frac{E_c K}{(K-1)(1 + E_n/E_c)} \right]^{1/2}. \quad (3.6)$$

where K is the number of detectors, E_c is the coherent energy and E_n is the energy of the null data stream after subtracting the reconstructed waveform. The cWB detection ranking statistic of GW150914 was $\eta_c = 20$, resulting in a FAR of 1 in 22,500 years with a trial factor of three and a detection significance $\sigma > 4.6$ [7]. The FAR statistic is also LIGO-Virgo preferred method to set upper limits on rates of GW signals from yet undetected transient sources, such as nearby CCSNe. In the latest LIGO-Virgo search for CCSN signals [53], the FAR of each event was computed by comparing the on-source ranking statistic to the time-shifted background estimation from off-source data. For example, the type-Ib/c supernova SN2017gax was discovered by DLT40 at a luminosity distance of 19.7 Mpc on August 14th, 2017. Although the exact time of the supernova explosion is unknown, theoretical models based on CCSN luminosity curves provide a rough estimate

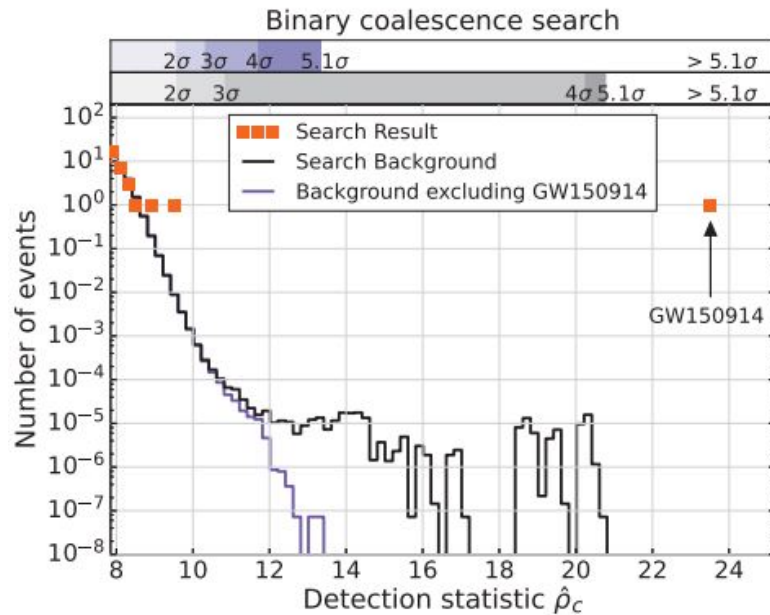


Figure 3.5. The number of observed events as a function of detection statistic $\hat{\rho}_c$ for GW150914 analysis time. Figure is taken from Ref. [7].

of 1.66 days for the time window when the explosion likely occurred. One day of off-source LIGO data was then used to produce a background of 16.2 years [53]. The FAR of the loudest SN2017gax GW candidate trigger was estimated to be 0.59 per year at a 3σ confidence level, a value not significant enough to claim a detection. The FAR provides a measure of the significance of GW detections. Reduction of the search background is crucial to improve the detection of GW signals. This goal can be obtained by improving the detector, mitigating environmental instrumental noise sources, and improving data analysis algorithms. Thus many LIGO and Virgo students and scientists currently work to make detection techniques increasingly efficient, bring the detectors to design sensitivity, and develop the next generation of GW interferometric detectors. LIGO and Virgo GW searches employ a plethora of other statistical tools that could not be covered in this brief article [54]. Bayesian methods are typically used to estimate the posterior distribution of source parameters. Likelihood functions [55] are applied, for example, in searches for GWs

from cosmic strings [56] and gamma-ray burst triggered searches [57]. The \mathcal{F} -statistic [58] is implemented in continuous-wave GW searches to characterize signals. Over the years statistical tools have become essential tools in GW research. Statistics played a fundamental role in the detection of GWs and the birth of multi-messenger astrophysics and enabled scientists to look deeply into the universe and understand some of its most fascinating mysteries. As we continue into the future, this emergent branch of science will continue to rely upon and benefit from statistical science.

3.6. ORIGINAL CONTRIBUTION

DQ serves as the cornerstone for GW searches. Given the high sensitivity of the detectors, noise reduction is a constant focus in these efforts. This section discusses the false alarm rate drawn from a paper I co-authored, titled “A Needle in (Many) Haystacks: Using the False Alarm Rate to Sift Gravitational Waves from Noise,” published in *Significance*, vol. 18, no. 1, 2021.

My contributions include performing seven one-week DQ shift reports and conducting event validation for two candidate events during the O3 observing run. My involvement continues in the ongoing O4 run, where I have mentored others in DQ shifts and completed multiple event validations. Additionally, I am responsible for generating the DQ Category Flag 2 utilized in GW burst transient searches.

4. OVERVIEW OF CORE-COLLAPSE SUPERNOVAE

The term “nova” in astronomy originates from the Latin phrase “nova stella”, which translates to the new star. This refers to the sudden appearance of a bright star in a region of the sky where no such star previously existed. The word “supernova” was first introduced in 1931 to describe stellar eruptions that are far more powerful than novae [59]. By 1938, supernovae had become a term designated for a specific class of explosive stars that were observed in multiple galaxies [60]. Supernovae mark the dramatic end of a massive star’s life cycle, culminating in a powerful explosion that usually leaves behind an ever-expanding gaseous remnant [59]. These remnants influence the surrounding circumstellar and interstellar medium. They may also lead to the formation of a compact stellar core [61]. Supernovae have significant impacts on localized galactic sectors, the host galaxy at large, and even the intergalactic medium [61]. With an estimated average frequency of two events per galaxy per century [62], supernovae serve as rich sources of scientific information, providing invaluable insights across various fields of astrophysics. Observations from these phenomena span a wide range of scientific domains, encompassing photometric and spectroscopic measurements across the entire electromagnetic (EM) spectrum [63]. Additionally, they provide valuable insights into new fields such as neutrino physics [64], cosmic rays [65], and GW astronomy [12, 13]. A comprehensive introduction to CCSN physics can be found in the book [59].

4.1. FORMATION OF CCSNE

Stars spend most of their life in the main sequence phase, burning hydrogen into helium through nuclear fusion [60]. Once the hydrogen fuel is depleted, they transition to subsequent phases, engaging in the fusion of progressively heavier elements [59]. These later stages of nuclear fusion occur at an accelerated pace, resulting in the formation of increasingly dense and tightly bound atomic nuclei. This transition in the rate of nuclear

fusion and the complexity of the elements involved represents a pivotal moment in a star's evolutionary path, ultimately determining its final state: be it a white dwarf (WD), neutron star, or supernova [66]. I will briefly describe the main aspects of stellar evolution that are useful for the dissertation.

For stars with initial masses less than approximately $8M_{\odot}$, electron degeneracy pressure prevents the achievement of densities and temperatures high enough to ignite their carbon-oxygen cores, causing them to evolve into carbon-oxygen WDs [66]. Following the discussion in Ref. [59], stars with initial masses between $8 - 9M_{\odot}$ evolve into oxygen-neon-magnesium (ONeMg) WDs. In contrast, stars with initial masses between approximately $9 - 10M_{\odot}$ may also develop ONeMg cores but are more likely to undergo supernova explosions. The core collapse in these stars is often triggered when degenerate electrons are captured by neon and magnesium nuclei, thereby reducing the core pressure. For stars with initial masses ranging from approximately $9 - 100M_{\odot}$, nuclear burning continues past silicon, resulting in an iron core. The pressure of the core is further reduced, resulting in a dynamic collapse of the core. For stars with initial masses above $\sim 100M_{\odot}$, thermonuclear reactions may be sufficiently powerful to prevent gravitational collapse, leading to pair-instability supernovae. Or the gravitational collapse is inevitable, expected to continue until the formation of a BH [67].

Upon reaching the end of its evolutionary journey, a star's core collapses and might lead to one of the most awe-inspiring phenomena in the universe: a CCSN. The intricate mechanisms behind this explosive event hinge on the complex interplay between nuclear physics, thermodynamics, and gravitational forces, all of which are set in motion during the core collapse. As we transition from discussing the formation of CCSNe, it's essential to delve into the various models that aim to explain their subsequent explosive mechanisms.

4.2. EXPLOSION MECHANISM

Following the work in Ref. [59], the star's core collapse typically lasts for approximately 0.3 s. During this phase, the outer core falls at supersonic speeds while the inner core descends subsonically. When the inner core reaches supranuclear densities, the nuclear matter stiffens, causing the collapse to halt abruptly. This bounce of the inner core launches a shockwave into the infalling outer.

This shockwave loses its energy through the dissociation of iron nuclei and becomes a stalled accretion shock approximately 150 km away from the core within 10 ms of its creation. To trigger an explosion and create a stable neutron star, this shock needs to be revived within a few hundred milliseconds to expel the outer shell. If the shock wave fails to revive in time, the Proto-Neutron Star (PNS) exceeds its stability threshold, leading to the formation of a BH [67].

The mechanism behind the revival of the stalled shock wave is not yet fully understood and remains a subject of intense research focus. Various theories and models are being explored to understand this complex process [8, 68, 69, 70, 71, 72, 73, 74]. Two leading theories propose distinct explosion mechanisms: neutrino-driven [75] and magneto-hydrodynamically (MHD) [76] driven explosions, each yielding unique dynamical behaviors and operating on specific timescales. These theories are intrinsically connected to the nature of their stellar progenitors, either slowly or rapidly rotating massive stars.

4.2.1. Neutrino-driven Explosion. The neutrino-driven explosion is considered one of the leading models to explain how the explosion in CCSNe occurs [77, 78, 79]. In the case of a slowly rotating progenitor star, neutrino heating is generally considered to be the key factor that revives the initially stalled shock wave. This mechanism plays a crucial role in facilitating the progression of the shock front, leading to a successful supernova explosion.

When the core collapses and rebounds, a shock wave is initiated that travels outward, creating a negative entropy gradient in its wake within the first few milliseconds. This leads to the onset of prompt convection in the post-shock region, approximately 10 ms after the bounce. This phase of prompt convection is relatively short-lived, lasting for about 50 ms, and is followed by a quiescent period that extends for roughly 100 ms [75].

Subsequent to this lull, neutrino heating within a specific area known as the gain region takes over, instigating neutrino-driven convection behind the advancing shock wave. In certain models [8, 78, 80, 81], the shock wave can also exhibit Standing Accretion Shock Instabilities (SASI) [82], characterized by large-scale, non-radial oscillations. Concurrently, the neutrino emissions from the PNS induce a negative lepton number gradient in the gain region spanning 10 to 25 km, fueling robust PNS convection for several seconds post-formation. As shown schematically in Figure 5.1, these combined instabilities disturb the PNS and induce its oscillations, which in turn give rise to GWs. This revives the stalled shock wave with enough energy to eject the star’s outer envelope, ultimately leading to a supernova explosion. Figure 4.2 shows the GW amplitude and the characteristic wave strain from one of the neutrino-driven explosion simulations by Kuroda [9]. The component “A” originated from the PNS g-mode oscillation. The component “B” is considered to be associated with the SASI activities.

4.2.2. MHD-driven Explosions. MHD-driven explosions provide a possible alternative mechanism to neutrino-driven mechanisms [76, 83, 84]. These models emphasize the interplay between magnetic fields and the fluid dynamics of the collapsing stellar core.

For progenitor stars with rapid rotation, the angular momentum amplifies and organizes magnetic fields, allowing MHD forces to primarily govern the outflows [67]. The mass and metallicity of the progenitor can further complicate the dynamics and timescales involved in these explosions.

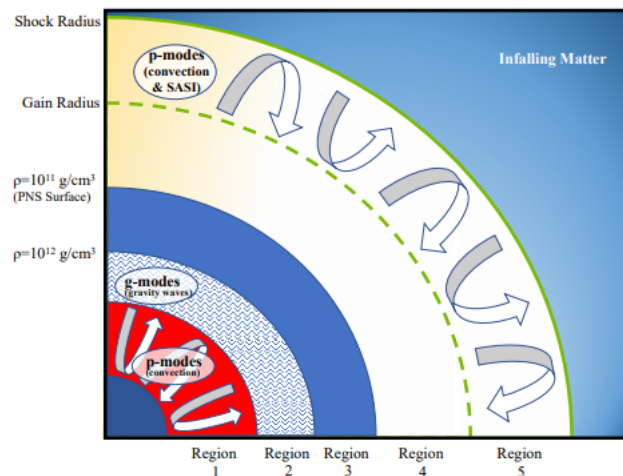


Figure 4.1. The schematic depiction of the CCSN central engine for the slowly rotating case. Figure is taken from Ref. [8].

The basic features of the MHD models can be described as follows. The conservation of angular momentum leads to increased rotational speed, generating intense magnetar-like magnetic fields. These fields counteract the inward gravitational forces and may channel some of the collapsing matter along the magnetic poles, creating jets. These jets can then impart sufficient energy to the star's outer layers, triggering a supernova explosion.

Therefore, the core collapse manifests differently along the equatorial plane and the rotational axis due to centrifugal support. This results in a PNS with an axisymmetric oblate deformation immediately after bounce. The subsequent PNS oscillations endure for approximately 10–20 ms and remain axisymmetric. The strength of GW signals grows with the rotation speed, classifying the models as slowly, rapidly, and extremely rapidly rotating [67].

In the slowest rotating model, the GW signal is minimal at bounce, but prompt convection emerges around 10 ms post-bounce, detectable in the GW signature. Conversely, rapidly rotating models inhibit prompt convection due to the presence of strong, positive

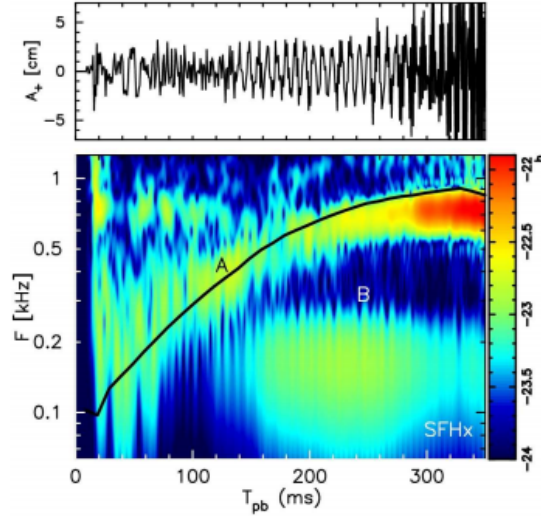


Figure 4.2. Top: GW amplitude of plus mode A_+ [cm], bottom; the characteristic wave strain in the frequency-time domain in a logarithmic scale which is overplotted by the expected peak frequency (black line denoted by “A”). Figure is taken from Ref. [9].

gradients of specific angular momentum in the post-shock region. Models with extreme rotation indicate a wider bounce spike, implying slower dynamics and lower frequencies in the GW signal [67].

The MHD-driven model may be mostly relevant when observations of the supernova remnant indicate high rotation or significant bipolar outflows. It also plays a role in explaining GRBs that originate from CCSNe.

4.3. GRAVITATIONAL-WAVES EMITTED FROM CORE-COLLAPSE SUPERNOVES

4.3.1. GW Amplitude. The strain of a GW wave emitted by a source at distance D can be estimated with the quadrupole formula 2.7. A back of the envelope calculation for the GW amplitude gives

$$\begin{aligned}
 |h| &= \frac{2G}{c^4 D} \ddot{I}_{ij} \\
 &\simeq 10^{-21} \left(\frac{\epsilon}{0.1} \right) \left(\frac{10 \text{ kpc}}{D} \right) \left(\frac{M}{M_\odot} \right) \left(\frac{R_c}{10 \text{ km}} \right)^2 \left(\frac{T_{\text{dyn}}}{1 \text{ ms}} \right)^{-2}.
 \end{aligned} \tag{4.1}$$

where the quadrupole contribution has been written as a product of the main factors that determine the strain: the typical mass M , the radius of the inner core R_c , and the dynamical timescale at the point of core bounce T_{dyn} , respectively. The distance D of the CCSN in Equation 4.1 is normalized to 10 kpc, i.e., the distance of the Sun from the Milky Way's center. The parameter ϵ denotes the degree of nonsphericity of the collapsing object. A value of 0 for ϵ corresponds to a spherical configuration [59].

The emission of GWs vanishes for a rotating star since $\ddot{I}_{ij} = 0$. However, GWs may be emitted if the rotating star undergoes dynamic contraction or expansion, causing the time derivatives of the quadrupole moments to be non-zero. We assume the GW propagates radially from the source at a distance D along the r direction. Owing to the TT nature of the GWs mentioned in 2.1, the components h_{rr} , $h_{r\theta}$ and $h_{r\phi}$ vanish. Consequently, the $+$ and \times polarization modes of the GWs can be expressed as

$$h_+ = \frac{h_{\theta\theta}}{D^2}, \quad h_\times = \frac{h_{\theta\phi}}{D^2 \sin \theta}. \quad (4.2)$$

4.3.2. GW Energy. Now we focused on the energy associated with GWs. The relationship between the total energy emitted in GWs, denoted as E_{GW} and the LVK standard metric for burst amplitude at the detector, h_{rss} can be expressed as:

$$\begin{aligned} h_{\text{rss}} &= \int_{-\infty}^{\infty} dt [h_+^2(t) + h_\times^2(t)] \\ &= 2 \int_0^{\infty} df \left[|\tilde{h}_+(f)|^2 + |\tilde{h}_\times(f)|^2 \right]. \end{aligned} \quad (4.3)$$

The GW flux, or energy per unit area per unit time, is given by:

$$F_{\text{GW}} = \frac{c^3}{16\pi G} \langle \dot{h}_+^2(t) + \dot{h}_\times^2(t) \rangle. \quad (4.4)$$

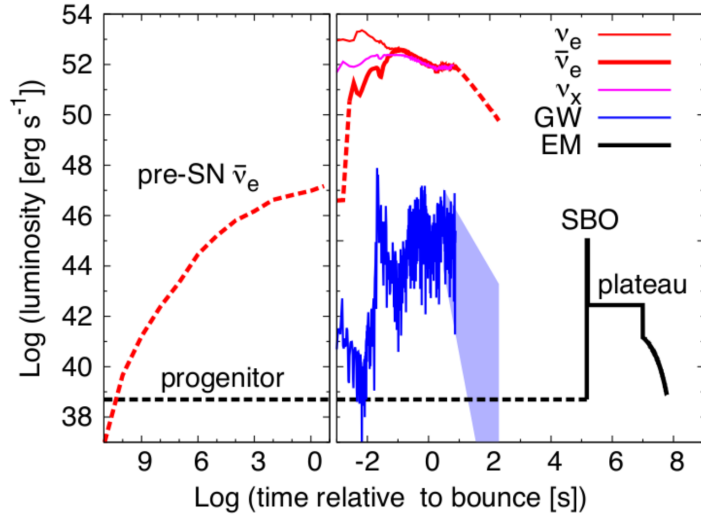


Figure 4.3. Time evolution of neutrino, GW (thin blue line), and EM (thick black line) signal luminosities for a non-rotating $17 M_{\odot}$ progenitor star. Figure is taken from Ref. [10].

For rotational motion, the total energy E_{GW} can be expressed as:

$$E_{\text{GW}} = \frac{2}{5} \frac{\pi^2 c^3}{G} r^2 f_0^2 h_{\text{rSS}}^2. \quad (4.5)$$

Here, we have utilized h_{rSS} for an optimally oriented source, where ($\iota = 0$). The derived expression for E_{GW} is $\frac{2}{5}$ times the result one would expect for isotropic emission, as referenced in the literature [85].

4.4. MULTIMESSAGENER ASTRONOMY OF CORE-COLLAPSE SUPERNOVAE

The exploration of CCSNe has reached an exciting juncture with the advancement of multi-messenger astronomy. This multidisciplinary approach involves various messengers such as EM waves[63], GWs[12], neutrinos[64], and even cosmic rays [65] to unlock a more understanding of the complexities of these astrophysical phenomena.

Figure 4.3 offers a comparative overview of the timings and energies associated with different messengers in CCSNe. In the preliminary phase, the star undergoes silicon burning, emitting neutrinos that could be detectable for exceedingly proximate CCSNe. As the star approaches the Chandrasekhar mass limit, core collapse ensues, accompanied by a robust neutrino outflow lasting approximately 100 seconds. Within the first second post-collapse, GW signals emerge. These in-band signals are expected to last less than a second. Following this, the shockwave propagates outward. The time that the shockwave takes to reach the star's surface can vary from a few hours to a few days, contingent upon the specific attributes of the progenitor star. The moment the shock breaks through the surface, known as Shock Breakout (SBO), marks the point when the supernova becomes optically visible. In the post-explosion, the remnant takes the place of the original star, and after several years, cosmic rays originating from this remnant become observable. This multi-messenger framework provides a comprehensive picture, capturing the complex chronology and energetics of a CCSN event [59].

The energy released by a stellar explosion is approximately 10^{53} erg, which is disseminated through multiple channels. A dominant 99% of this energy manifests as low-energy (MeV) neutrinos. The residual 1% is predominantly allocated to the kinetic energy of the shockwave. A minuscule fraction, about 0.01%, powers a multi-wavelength EM emission, and an even smaller portion, a few times 10^{46} erg, is disseminated through GWs [59].

From an observational standpoint, Supernova 1987A serves as a landmark event, as shown in Figure 4.4. It contains X-rays from NASA's Chandra X-ray Observatory (blue), visible light data from NASA's Hubble Space Telescope (green), and submillimeter wavelength data from the international Atacama Large Millimeter/submillimeter Array (ALMA) telescope in Chile (red). Although it is located in a neighboring galaxy rather than our own Milky Way, its relative proximity allowed for a variety of studies [86, 87, 88, 89, 90].

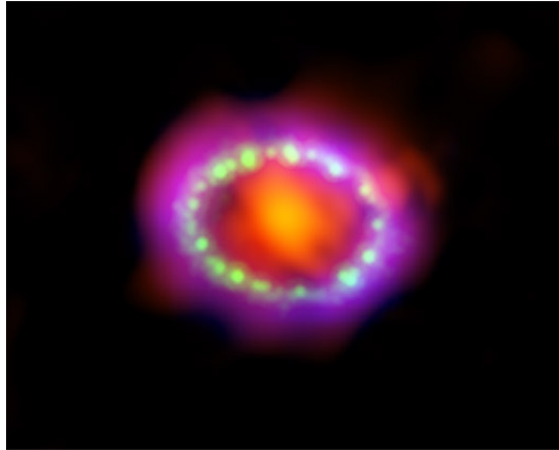


Figure 4.4. The composite image of supernova 1987A. Figure is taken from Chandra X-ray Observatory.

It led to an invigorated interest in neutrino astrophysics and enriched our understanding of the SN phenomenon. The detection of neutrinos from Supernova 1987A underscored the pivotal role these particles play in the dynamics of supernovae.

Since GWs are generated by the aspherical motion in the inner regions, they contain information about the dynamics of the central engine. In addition, neutrinos carry information about the thermodynamic conditions at the surface of the PNS. Therefore, observations of GWs and neutrinos will enable us to probe the central engine in a completely new way. In particular, this may allow us to extract information about the mechanism that produces the explosion. Moreover, such an observation may reveal the rotation and the structure of the innermost regions of the star.

For future detections, especially of one of the last of the primary sources of GWs that will be detectable by current-generation GW detectors: a galactic core-collapse supernova explosion. The GW detection of a galactic CCSN, along with the detection of the supernova neutrinos, will provide direct information about the supernova central engine. It will allow us to validate our models and derive a better understanding of the central engine's physics.

4.4.1. EM Emissions. The majority of SNe have been observed predominantly through their EM emissions. While these emissions have provided a wealth of information, they come with limitations, specifically in offering only a narrow window into the star's core where the central engine of a CCSN is located.

Before the actual core-collapse event, pre-CCSN signals present a unique observational opportunity. These signals offer insights into the state of massive stars just before they undergo core collapse. Despite challenges in positional localization with pre-CCSN neutrinos, the small number of such massive stars close to the Sun allows for continued monitoring. However, the rarity of these massive stars implies a low rate of CCSN events [63].

A critical point in the EM observations of CCSNe occurs hours to days following the core collapse when the supernova shock wave breaks out of the progenitor star's surface. This SBO results in a bright burst of ultraviolet (UV) and X-rays. Capturing this fleeting signal can offer vital data, such as the progenitor star's radius. However, the short-lived nature of SBO makes its detection a significant challenge, and knowing where to look for this signal in advance would greatly enhance detection prospects [59].

Following the SBO, the EM emission enters the so-called plateau phase, which can last around 100 days. During this time, the luminosity and duration of this plateau offer additional clues about the progenitor star, such as its radius and the mass of the ejecta. More conventional investigations of CCSNe characteristics like energy, composition, and velocity also play a crucial role in our understanding of these stellar explosions. For this reason, a well-observed early light curve is essential for an accurate reconstruction of the CCSN's evolutionary path.

In summary, EM observations continue to be a significant tool in our study of CCSNe, even if they provide limited information about the internal dynamics of these stellar events. Each stage of EM emissions offers unique opportunities for enhancing our understanding of CCSNe and their progenitors [59].

4.4.2. Neutrino Emissions. Neutrino emissions begin before the onset of core collapse, during the terminal stages of silicon burning. These emissions can be detected by Hyper-K up to a few kiloparsecs away, serving as an early warning system for an impending CCSN event [10, 64]. In the first approximately 10 seconds following the core collapse, a substantial burst of neutrinos was emitted. It is confirmed by observations of SN 1987A [86, 87]. SN 1987A was a landmark event in CCSN studies. It was not just the first CCSN to be detected by neutrino experiments but also the first supernova visible to the naked eye since Kepler’s observation in 1604. The progenitor of SN 1987A was a star with an approximate mass of $15 M_{\odot}$, located in the outskirts of the Tarantula Nebula in the Large Magellanic Cloud at a distance of about 50 Kpc[87]. This event serves as a cornerstone, demonstrating the vital role neutrinos play in our understanding of CCSNe and their progenitors.

A variety of neutrino detectors are presently operational, capable of capturing neutrinos emitted during CCSNe. Among these, Super Kamiokande (Super-K) [91, 92] stands out for its potential to amass a rich data set of neutrino events from future galactic CCSNe. IceCube [93, 94] possesses equal statistical neutrino detection potential. Other smaller, yet sensitive detectors include Baksan [95], Borexino [96], HALO [97] KamLAND [98], LVD [99] etc. In the coming years, advancements in detector technology will significantly boost our capability to capture and analyze CCSN neutrinos.

4.5. SEARCH FOR GWS FROM CCSNE

Searching for GWs emitted from CCSNe holds significant promise for enhancing our understanding of the explosion mechanisms, as well as for contributing to the burgeoning field of multi-messenger astronomy. Data from GW observatories like LIGO and Virgo, when combined with information from optical and EM telescopes, allow for optically triggered searches for GWs that are associated with CCSNe [12, 13].

The first step in this process involves estimating the sky location of the CCSN, which is facilitated by its observation of optical and EM spectra. Knowing its location helps to identify its host galaxy, from which we can then estimate the distance to the supernova. This estimated distance, along with the information of the progenitor star, which can also be derived from observational data, helps us to predict the time interval during which we would expect the GWs to be emitted. This expected time interval is known as the on-source window (OSW) [100].

Armed with this information, we proceed to perform a coherent search for potential GW signals using all available detectors. To accomplish this, we utilize a specialized search pipeline: cWB [52, 101, 102], which combines the data from multiple detectors to identify possible GW emissions. By aligning the data in this way, we increase the sensitivity of the search and improve the likelihood of successful GW detections. This multi-pronged approach integrates data from various observational platforms, serving as a powerful tool for understanding the complex processes at play during the collapse and subsequent explosion of massive stars.

4.5.1. On-source Window. The OSW refers to the time frame during which a GW event is most likely to be detected. It is defined by t_1, t_2 , which signify the beginning and end of this interval respectively. The objective is to establish an OSW that is long enough to capture the GW transient with a high degree of certainty, yet short enough to enhance the sensitivity for detecting weaker signals when compared to broader, all-sky searches.

To estimate the OSW, the light curve of the CCSN is essential. The light curve is a graphical representation of the luminosity or brightness of the supernova as a function of time [63]. It serves as a crucial diagnostic tool for astronomers, as it encapsulates key stages and physical processes that unfold during and after the explosion. Observations of CCSNe can be categorized into three distinct phases, following the discussion in Ref. [100]. In the early observation phase, CCSN is detected in the optical range before the shock breakout, while the shockwave is still progressing through the stellar material. Based on this, we can

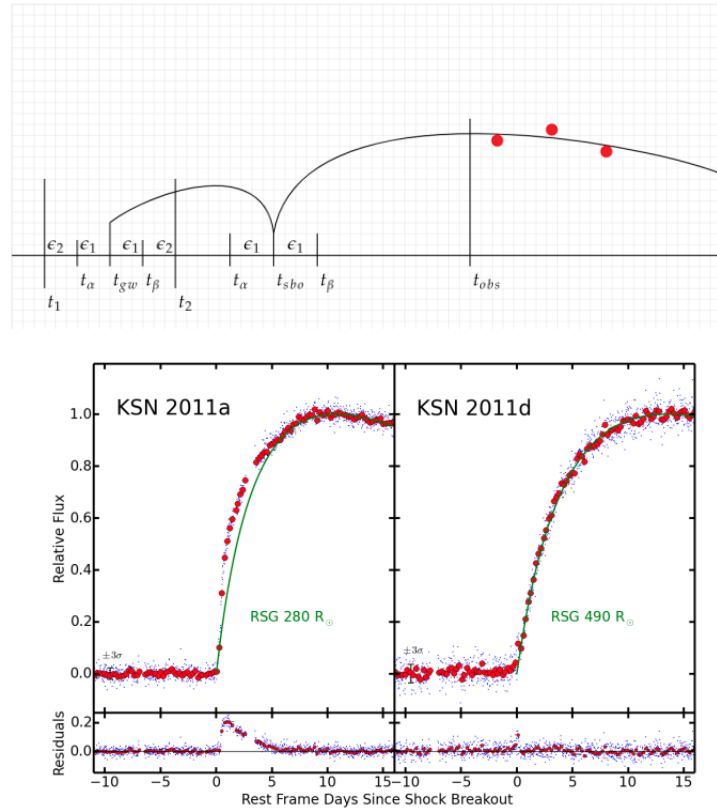


Figure 4.5. Top: the three different phases of observing the explosion in the EM regime. Bottom: The early light curves of the two Kepler type II-P supernovae: KSN2011a, KSN2011d. Blue dots are individual Kepler flux measurements with a 30 minute cadence and the red symbols are 6-hour medians. The x axis shows the redshift corrected time since the SBO was estimated from the model fit. Figure is taken from Ref. [11].

reasonably define the OSW that lasts from several hours to a few days, depending on the material of the progenitor star. This window is framed by the last time the CCSN was not observed and the moment it was discovered. During the peak light curve phase, the outer shell of the collapsed star begins to cool and ionized gas recombines. This thinner gas layer permits the escape of photons, creating a plateau in the light curve that indicates the time taken for recombination waves to reach the core post-collapse.

The recombination phase follows months after the peak light curve phase. Here, radioactive material is emitted from the supernova, generating light that, although less intense than at the time of the explosion, remains observable for several months. This dimming light corresponds to the decay of the radioactive material, marking a steady decline in the light curve. Figure 4.5 shows the phase and light curve from two Kelper supernovae as an example.

Several methods exist for estimating the time of the SBO to define the OSW. In the method of early observation, initial supernova observation t_{disc} , which is the discovery time, is used as the end of the OSW. The beginning of the OSW is calculated using the last null observation of a CCSN in the host galaxy t_{null} . This time can still be after the GW emission since the SBO is delayed with respect to the collapse t_{SBO} . We use $t_{null} - \Delta t_{SBO}$ as the beginning of OSW, while Δt_{SBO} can be estimated from the progenitor star.

For CCSNe with the light curves exhibiting a universal and smooth behavior up to their flux peak, the Quartic Interpolation method proves useful. The quartic polynomial fit is adopted to estimate the SBO timing, even when data from the first few days post-SBO were missing. This process yields a confidence belt for the SBO timing for each candidate CCSN.

For instances where the light curve data is of low quality, we utilize a hybrid approach that combines various physics-based interpolation methods. This results in an OSW that holds a high likelihood of encompassing the GW emission. Additionally, this method offers the potential to glean insights into the properties of the progenitor star.

4.5.2. Coherent WaveBurst. cWB is a data-analysis pipeline designed for the identification and characterization of GW transients [52, 101, 102]. As a principal algorithm in unmodeled GW searches, it is based upon the Maximum Likelihood mathematical framework. This method is particularly adept at capturing a broad range of transients that may not conform to any pre-existing templates or models. This method has the flexibility to detect a wide spectrum of GW signals, including those emanating from CCSNe.

The cWB searches for a coherent signal power in multiple detectors. The analysis is performed in a wavelet domain on GW strain data using the multi-resolution Wilson-Daubechies-Meyer wavelet transform [103]. The algorithm selects wavelets with amplitudes above the fluctuations of the detector noise and groups them into clusters, identifying coherent events.

cWB employs a constrained maximum likelihood approach. This statistical framework is designed to maximize the likelihood function of GW data and aims to find the most probable GW signal given the observed data from GW detectors. Each data stream from the detector is subjected to wavelet decomposition into distinct bases, each with varying time and frequency resolutions. Following this decomposition, the data undergo a whitening process, standardizing the statistical properties of the noise and rendering the data suitable for statistical inference. Within the whitened data, only the top 0.1% of wavelet magnitudes in each frequency bin and decomposition level are retained, termed as “black pixels”. Additionally, “halo pixels” surrounding these black pixels are also kept. Clusters of these pixels are identified once all wavelet decompositions are projected onto a unified time-frequency plane. These clusters are essentially sets of contiguous retained pixels, either black or halo, which are most likely related to a GW event [101].

To mitigate the risk of false positives, each cluster must be coherent across multiple interferometers. This coherence is determined based on the cluster’s compatibility with the expected direction of the GW arrival, thereby ensuring the reliability of the detected events. Upon satisfying these stringent conditions, a Gaussian likelihood function is computed for each cluster. The unknown GW signal is then reconstructed through a maximum likelihood estimator tailored to this function. The culmination of the cWB pipeline is the generation of triggers or candidate GW events, which can then be subject to further analysis and validation.

The versatility of the cWB pipeline makes it particularly suitable for detecting GW events from CCSNe. The cWB's multi-resolution wavelet decomposition and constrained maximum likelihood estimation are well-suited for capturing these complex signal morphologies. Moreover, its ability to generate triggers provides an invaluable tool for time-sensitive follow-up observations, which are crucial in the study of CCSN phenomena. The pipeline's robust statistical framework allows for the extraction of key parameters of the CCSN event, contributing to our understanding of CCSNe.

5. SEARCH FOR GWS EMITTED FROM CORE-COLLAPSE SUPERNOVAE DURING O3 RUN

Since the first observing run by LIGO and Virgo, three observing runs have been carried out, each incorporating optically triggered searches for GWs emitted from CCSNe. To date, no GWs originating from CCSNe have been detected. Because GWs predicted from the multidimensional CCSN simulations produce relatively weak GWs (compared to compact binaries) and they can be detectable only within Milky Way for Advanced GW detectors and their upgrades [104, 105]. However, these simulations and the many models of more energetic GW emission have not yet been observationally constrained. This motivates us to search for GW transients with CCSNe that occurred in the nearby Universe. While a Galactic CCSN will be the best opportunity for detecting GWs, LIGO [106], Virgo [107], and GEO600 [108] performed two targeted searches for GWs from CCSNe outside Milky Way. Both of them reported null results. The search with the initial GW detector data [109] established the search method; four CCSNe were analyzed within a distance of 15 Mpc. Later, Ref. [13] reports on a search on five CCSNe within 20 Mpc with data from the first and second observing runs. For the first time, the GW data enabled us to exclude parts of the parameter spaces of CCSN extreme emission models. LIGO, Virgo, and KAGRA [110] performed all-sky all-time generic searches [111, 112, 113, 114] that also had the potential to detect GWs from a CCSN. The previous CCSN searches are described more in detail in [104].

In this section, we present the results of the optically triggered search specifically from the third observing run. Furthermore, we include an extended analysis that discusses the projected detection sensitivity for the upcoming fourth and fifth observing runs. we present an optically targeted search with CCSNe observed up to a distance of approximately 30 Mpc that occurred during the third observing run (O3, 2019 Apr 1 – 2020 Mar 30) of LIGO, Virgo, and KAGRA. We selected eight CCSNe; seven of them are type-II (SNe

Table 5.1. CCSNe selected as optical targets for the GW search described in this section. Δt is the OSW duration. The last column shows coincident data durations T_{coinc} together with duty factors ($T_{\text{coinc}}/\Delta t$).

Supernova	Type	Host Galaxy	Distance [Mpc]	Δt [days]	T_{coinc} [days]
SN 2019ehk	I Ib	NGC 4321	16.1	1.40	0.41 (29%)
SN 2019ejj	II	ESO 430-G20	15.7	7.58	1.25 (16%)
SN 2019fcn	II	ESO 430-G20	15.7	4.54	32.51 (55%)
SN 2019hsw	II	NGC 2805	28.2	8.00	5.08 (64%)
SN 2020oi	Ic	NGC 4321	16.1	3.70	2.56 (69%)
SN 2020cxd	IIP	NGC 6395	20.9	6.00	4.58 (76%)
SN 2020dpw	IIP	NGC 6952	22.3	4.00	3.06 (77%)
SN 2020fqv	I Ib	NGC 4568	17.3	6.00	4.06 (68%)

2019ehk, 2019ejj, 2019fcn, 2019hsw, 2020cxd, 2020dpw, 2020fqv) and one is type-Ic (SN 2020oi). No GW associated with a CCSN has been identified, so we provide statements about the predicted GW emissions’ detectability and constrain the CCSN engine’s dynamics. For the first time, we report the upper limits on the GW luminosity and PNS ellipticity. The constraints of two GW extreme emission models are improved with respect to [13]. Furthermore, we include an extended analysis that discusses the projected detection sensitivity for the upcoming fourth and fifth observing runs (O4 and O5).

5.1. TARGETED CORE-COLLAPSE SUPERNOVAE

5.1.1. Source Selection. From all CCSNe observed during O3, we have selected those that meet the following criteria: (i) they contribute to the model exclusion statements (see Sec. 5.4.3), their distances are less than approximately 30 Mpc, (ii) the period where we expect to find a GW transient is sufficiently well identified (up to a few day, see Sec. 5.1.2); and (iii) there is sufficient GW detector data coverage to allow us to accumulate a few years of background data (see Sec. 5.2). During O3, astronomers found and followed-up numerous CCSNe in the nearby Universe. Based on the information from Astronomical

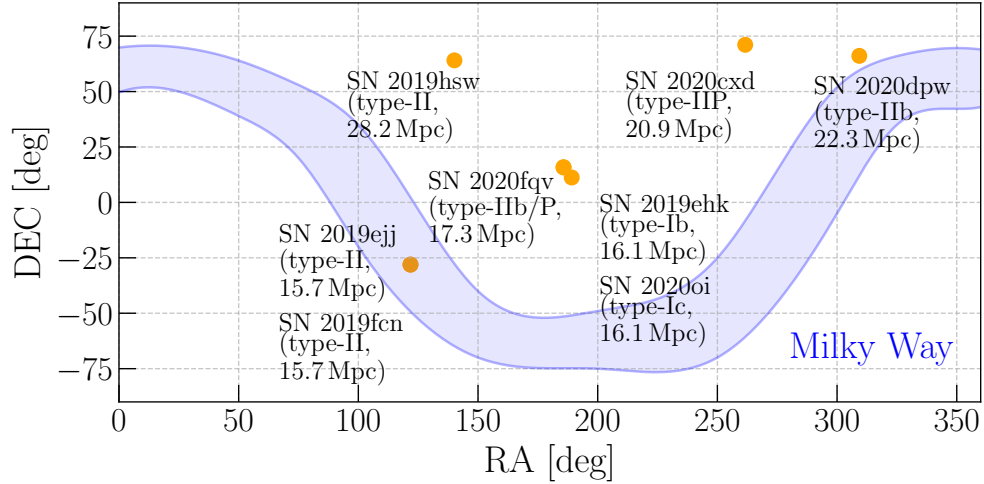


Figure 5.1. Sky locations of CCSNe are analyzed in this section. Figure is taken from Ref. [12].

Telegrams [115] and supernova catalogs (ASAS-SN [116, 117, 118, 119], DLT40 [120], Gaia [121, 122], ASRAS [123], TNS [124], OSC [125], CBAT [126]), we found eight supernovae of interest. They are reported in Table 5.1 and Figure 5.1 shows their sky locations. All were recorded within 30 Mpc during the third observing run of LIGO, Virgo, and KAGRA. Most of them are type-II supernovae originating from red supergiant progenitor stars, just one is type-I. The host galaxies are identified for all of them. The distance to each CCSNe is determined using the estimated distance to its host galaxy.

SN 2019ehk, a type-IIb supernova, was discovered on 2019 April 29 22:27:50 UTC [127]. The host galaxy is NGC 4321 (M100) at a distance of 16.1 Mpc [128, 129, 130] (distance inferred from Cepheid observations [131, 132, 133]). The progenitor star is either a zero-age main sequence (ZAMS) star with a mass of around $9 - 9.5 M_{\odot}$. The mass-loss rate smaller than $10^{-5} M_{\odot}/s$ for a wind velocity 500 km/s at distances $10^{16} - 10^{17}$ cm from the exploding core [133].

SN 2019ejj, a type-II supernova, was discovered on 2019 May 02 06:18:43 UTC [134]. The host galaxy is ESO 430-G20 at a distance of 15.7 Mpc [135] (distance inferred from Tully-Fisher method [136]).

SN 2019fcn, a type-II supernova, was discovered on 2019 May 08 23:02:24 UTC [137]. The host galaxy is ESO 430-G20 at a distance of 15.7 Mpc (distance inferred from Tully-Fisher method [136]).

SN 2019hsw, a type-II supernova, was discovered on 2019 June 18 03:07:12 UTC [138]. The host galaxy is NGC 2805 at a distance of 28.2 Mpc [139] (distance inferred from Tully-Fisher method [136]).

SN 2020oi, a type-Ic supernova, was discovered on 2020 January 07 13:00:54 UTC [140]. The host galaxy is NGC 4321 at a distance of 16.1 Mpc [129, 141, 142, 143] (distance inferred from Cepheid observations [131, 132, 133]) . The mass-loss rate is around $1.4 \times 10^{-4} M_{\odot} \text{ s}^{-1}$ for a wind velocity 100 km s^{-1} . *SN 2020oi* was also observed by *Swift* [144] with X-ray telescope in the energy range from 0.3 keV to 10 keV [145].

SN 2020cxd, a type-II supernova, was discovered on 2020 February 19 12:44:08 UTC [146]. The host galaxy is NGC 6395 at a distance of 20.9 Mpc [147, 148, 149] (distance inferred from Tully-Fisher method [150]). The progenitor star has a ZAMS mass of $\lesssim 15 M_{\odot}$.

SN 2020dpw, a type-IIP supernova, was discovered on 2020 February 26 10:01:22 UTC [151]. The host galaxy is NGC 6952 at a distance of 22.3 Mpc (distance inferred from Tully-Fisher and SN type-Ia methods, both agree) [135].

SN 2020fqv, a type-IIb supernova, was discovered on 2020 March 31 08:06:02 UTC [152]. The host galaxy is NGC 4568 at a distance of 17.3 Mpc (distance inferred from Tully-Fisher method [136]). The progenitor star has a ZAMS mass of $13.5 - 15 M_{\odot}$ [153].

5.1.2. On-source Window. We use three different methods to calculate OSWs. The choice depends on the availability of early observation (pre-peak luminosity) data and the availability of published tools to model the light curves. Table 5.1 shows the calculated OSWs and methods used.

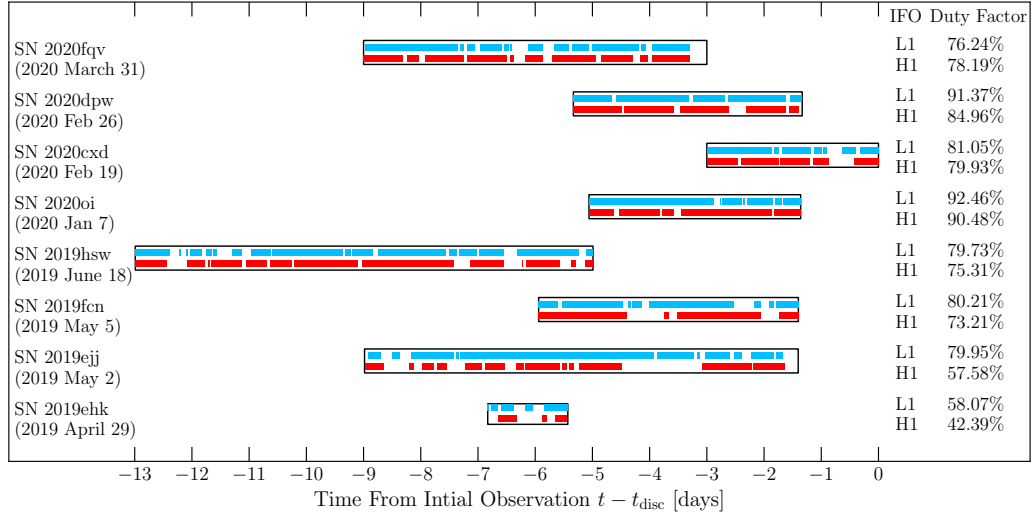


Figure 5.2. Visual representation of the on-source windows (see Sec. 5.1.2), the data coverage for each detector, and the detector duty factors (percentage of available data inside the on-source window). Figure is taken from Ref. [12].

5.1.2.1. Method 1 - the early observation. For SNe: 2019hsw, 2020cxd, 2020dpw, and 2020fqv, the available luminosity public data, at the time of this analysis, was of poor quality and did not appear to include the peak luminosity. For these candidates, we use an *Early* method described in [13] with an increased upper limit on the delay between the collapse of the shock breakout as described below. We note that a detailed photometry [153] for SN 2020fqv was publicly available in the late stages of our analysis.

5.1.2.2. Method 2 - the quartic interpolation. For SNe 2019ehk and 2020oi, the light curve indicated that the discovery happened in the homologous phase of the shock wave expansion. Since the part of the light curves of CCSNe up to the flux peak has a high degree of universality among observed CCSNe, we investigated what would be the simplest polynomial fit (where we estimated the coefficients of different polynomials with a chi-square minimization between the data and the polynomials). With the quartic interpolation and Monte-Carlo simulations, we estimated the t_{SBO} for each of the candidates and the uncertainties and, from that, the estimates of t_1 and t_2 .

5.1.2.3. Method 3 - the physics-Based. For SNe 2019fcn and 2019ejj, good quality public data were unavailable to perform the quartic interpolations. Instead, we used the OSWs published in Ref. [154] based on Las Cumbres Observatory data (named there an *Updated EOM*). These OSWs were produced using the overlap of different physics-based interpolation methods, with a large probability of containing the GW emission. This method has the potential also to provide progenitor star properties. While Methods 1 and 2 are frequentists, the results in this method involve Bayesian posteriors.

Figure 5.2 shows the OSW for eight SN candidates. These windows are plotted with respect to the discovery time t_{disc} , and the brackets show CCSN discovery dates in UTC. The plotted interferometers (IFO) are LIGO Hanford (H1) and LIGO Livingston (L1).

5.2. METHODOLOGY

We closely follow the methodology presented in Ref. [13], and this section briefly summarizes the method. The search is performed at the frequency range from 16 Hz to 2048 Hz.

5.2.1. Data. The LIGO and Virgo detectors use a photon recoil-based calibration [155, 156, 157] resulting in a complex-valued, frequency-dependent detector response. Previous studies have documented the systematic error and uncertainty bounds for O3 strain calibration in LIGO [158, 159] and Virgo [160, 161]. The product of this calibration is strain data sampled at 16384 Hz. Times affected by transient noise sources, referred to as *glitches*, and other data quality issues are identified so that searches for GWs can exclude (veto) these periods of poor data quality [162, 163, 164, 165, 166, 167, 168]. In addition, several known persistent noise sources are subtracted from the data using information from witness auxiliary sensors [169, 170]. In this search, we analyze a network of LIGO detectors (Hanford and Livingston). While adding the Virgo detector may provide benefits, e.g. sky localizations, it can affect the confidence of candidate detections. Hence, it is not an optimal choice for detection purposes [113] because of the higher rate of glitches.

5.2.2. Coherent WaveBurst. We use cWB for detecting and reconstructing GWs [101]. The coherent events identified by cWB are ranked with $\eta_c = \sqrt{E_c/\max(\chi^2, 1)}$, where E_c is coherent energy, and χ^2 quantifies the agreement of cWB reconstruction and the detector data. The correlation coefficient $c_c = E_c/(E_c + E_n)$, where E_n is a residual energy, further reduces noise events. The events are accepted when $\chi^2 < 2.5$ and $c_c > 0.8$. The remaining ones are divided into two mutually exclusive classes. Class *C1* contains transients of a few cycles with a prime example of short (order of 10 ms) and broadband (order of 100 Hz) *blip* glitches [171, 172]. All other events are in class *C2*.

As usual, we use time-shifting analysis to estimate the background for the burst searches. This method allows for estimating the FAR. For each analyzed OSW, we accumulated a few years of background data. An event with the smallest FAR from the non-time-shifted analysis across the two search classes is called the *loudest event* and is considered a potential GW candidate. Given two search classes, a trial factor of 2 is applied to the event's FAR [13]. The loudest event significance is assessed by calculating its false-alarm probability (FAP). This is the probability of obtaining one or more noise events that are less than or equally ranked:

$$\text{FAP} = 1 - \exp(-T_{\text{coinc}} \times \text{FAR}). \quad (5.1)$$

where T_{coinc} is the coincident data duration of the appropriate OSW.

Following Sec. 5.1.2, reducing time intervals to search for GW emission benefits optically targeted searches compared to all-sky searches in two ways or a combination. The first is to increase the statistical significance of the GW candidates by reducing the event's FAR. The second is to achieve the same statistical significance but with a larger FAR. This second option, in turn, allows reconstructing events with a smaller η_c or GWs emitted further away from the Earth. The usefulness of this second approach depends on

the slope of the FAR vs η_c histograms (a shallower slope, like in the case of glitchy data, would give larger gains in the detection range). Hybridization of the two would mean using some benefits in both directions. In this section, we only use the first type of benefit.

Note that the previous searches [13, 109] used an estimated 9.1% for the calibration error. In brief, the predicted GW signals from CCSNe (Sec. 5.2.3) were distorted in time and frequency according to the detector’s calibration errors at the times of the OSWs. We find that the impact on the η_c and c_c is negligible for a network of LIGO detectors.

5.2.3. Search Sensitivity. The search sensitivity is determined by adding waveforms to the detector strain data around every 33 s and reconstructing them with cWB. The procedure is repeated for sources placed at a range of distances, constructing a *detection efficiency*. The simulated sources are placed at the sky positions of the analyzed CC-SNe. We measure the search sensitivity with waveforms calculated from multidimensional CCSN simulations: neutrino- and magnetohydrodynamically-driven explosions, black hole formation, and quantum chromodynamics phase transition. We also consider two extreme emission models. For each three-dimensional model, the source orientation is randomized, and the waveforms from two-dimensional CCSN simulations are averaged over the source orientation using a factor of $\sqrt{5/18}$ [13]. The distance at 50% detection efficiency is called the *detection reach*.

As mentioned earlier, we employ *ad-hoc* signals to estimate the search sensitivity to monochromatic CCSN GW emission. These signals do not have physical meaning but are used to constrain the properties of a CCSN engine at a given frequency bin. The detection efficiencies are calculated as a function of the signal’s root-sum-squared strain:

$$hrss = \sqrt{\int (h_+^2(t) + h_\times^2(t)) dt}. \quad (5.2)$$

where h_+ and h_\times are GW polarizations.

5.2.3.1. Neutrino-driven explosions. In this section, we list and briefly describe the non-rotating, neutrino-driven explosion, or non-exploding CCSN models that are used to test the sensitivity of the search. All of the waveforms were simulated in three dimensions.

The first is model s11 from *Andresen et al. 2017* [173] (And+17). It is a solar metallicity $11.2 M_{\odot}$ progenitor star. The shock is not revived in this model. The simulation ends 352 ms after the core bounce. No standing accretion shock instability (SASI) is observed and most of the GW amplitudes are produced by convection. The low mass and lack of shock revival result in low GW amplitudes, with the majority of the GW energy at frequencies between 500 Hz and 700 Hz.

The s15 model is the solar metallicity, $15 M_{\odot}$ progenitor star simulated by *Kuroda et al. 2016* [80] (Kur+16) with the SFHx equation of state (EoS). The GW signal reaches frequencies of up to 1000 Hz, and has a strong low-frequency component due to the SASI. The simulation was stopped ~ 350 ms after the core bounce before the shock revival.

The C15 model is another $15 M_{\odot}$ progenitor star simulated by *Mezzacappa et al. 2020* [75] (Mez+20). The GW signals show a low-frequency component due to the SASI, and also a high-frequency component above 600 Hz due to convection. The simulation was stopped 450 ms after the core bounce before shock revival. The signal reaches very high GW amplitudes of above 1500 Hz.

The L15-3 model by *Müller et al. 2012* [174] (Mul+12) is an older simulation. However, we still include this model to compare to results in previous searches directly. The progenitor is a $15 M_{\odot}$ star. The GW emission only reaches frequencies of ~ 500 Hz, which is much lower than more modern simulations. The GW signal is 1.4 s long, and the model successfully undergoes shock revival.

We use two models from *O'Connor and Couch 2018* [81] (Oco+18). They are both simulations of a $20 M_{\odot}$ progenitor star from MESA [175, 176, 177, 178, 179, 180]. The first model, m20, does not include perturbations, and the second model, m20p, has perturbations.

Both of them are simulated for over 500 ms, and do not undergo shock revival before the end of the simulations. The GW signals in both models have a low-frequency component due to the SASI, and the high-frequency modes reach frequencies of over 1000 Hz.

The next two signals were simulated by *Powell and Müller 2019* [181] (Pow+19). The he3.5 model is an ultra-stripped $3.5 M_{\odot}$ helium progenitor star. The low mass results in low GW amplitudes. The s18 model is a solar metallicity $18 M_{\odot}$ progenitor star. Both models undergo successful neutrino-driven explosions and therefore have no low-frequency SASI modes. The he3.5 model is 0.7 s long, and s18 is 0.89 s. Both models have the majority of their GW energy between 600 Hz and 1000 Hz.

We use three models from *Radice et al. 2019* [78] (Rad+19). They are all solar metallicity progenitor stars with masses of $9 M_{\odot}$ model s9, $13 M_{\odot}$ model s13, $25 M_{\odot}$ model s25. The s9 simulation undergoes shock revival shortly after the bounce, and model s25 undergoes shock revival much later in the simulation, s13 does not explode. The s25 model has low-frequency GW emission due to the SASI, the GW signal is ~ 600 ms long and reaches frequencies of up to 1200 Hz. The s9 model has low GW amplitudes due to low mass, is simulated for ~ 350 ms and reaches frequencies of ~ 1000 Hz. The s13 model was simulated for over 0.7 s, and reached frequencies of up to ~ 2000 Hz.

5.2.3.2. Magnetorotational explosions. *Obergaulinger et al. 2020* [76] (Obe+20) performed a series of three-dimensional simulations of magnetorotational core collapse of potential progenitors of long gamma-ray bursts. While all of their cores are based on a star with a ZAMS mass of $35 M_{\odot}$ and sub-solar metallicity, the authors varied the pre-collapse magnetic field strength and geometry. We select their model signal_O, which develops a delayed, moderately energetic explosion dominated by magnetically driven jets reaching outflow speeds of around $c/3$ by the end of the simulation at about 0.8 s after the bounce. The explosion is launched by a combination of neutrino heating, rotation, the magnetic

field, and hydrodynamic instabilities, among which convection is more important than the SASI. Due to greater core asymmetries during the collapse, the GW emissions are larger than for neutrino-driven explosions.

5.2.3.3. Black hole formation. The black hole formation s40 model is a $40 M_{\odot}$ progenitor star, labeled model NR, from *Pan et al. 2021* [182] (Pan+21). The simulation did not undergo shock revival, and it was stopped ~ 0.7 s after the bounce when a black hole was formed. The GW frequency is rather high, above 2000 Hz at peak luminosity.

5.2.3.4. QCD phase transition. *Kuroda et al. 2022* [183] (Kur+22) investigate observable signatures of a first-order quantum chromodynamics phase transition in the context of CCSNe. The authors conduct axially symmetric numerical relativity simulations using a hadron–quark hybrid EoS with multi-energy neutrino transport. The progenitor model with $50 M_{\odot}$ of Umeda & Nomoto [184] is a blue supergiant star with solar metallicity. During the post-second-bounce phase, the GWs show a high-frequency emission at the range of $\gtrsim 1$ kHz. We analyzed the waveform from the s50 model.

5.2.3.5. Extreme supernova models. Given the large uncertainties in the numerical modeling of fast-rotating CCSNe, it is worth exploring extreme models at the limit of what is possible during the collapse of massive stars. In particular, we consider two scenarios used in previous targeted searches [109].

In the *Long-Lasting Bar Mode* scenario (or shortly bar model), a very rapidly rotating progenitor star induces bar mode instabilities in the proto-neutron star. These instabilities are either of dynamical [185, 186, 187, 188] or correlational (low $T/|W|$) type [182, 189, 190] the latter being preferred according to the most recent and sophisticated simulations. In this scenario, the instability leads to large amplitude GWs that depend on the properties of the deformed proto-neutron star. We use a simple phenomenological bar model [191, 192] in which the waveform can be modeled effectively by sine-Gaussian

waveforms with amplitude h_0 , frequency f_0 and width τ as parameters:

$$h_+(t) = h_0 \frac{1 + \cos^2 \iota}{2} e^{-t^2/\tau^2} \cos(2\pi f_0 t), \quad (5.3)$$

$$h_\times(t) = h_0 \cos \iota e^{-t^2/\tau^2} \sin(2\pi f_0 t), \quad (5.4)$$

where ι is a source viewing angle. The model used in the previous targeted searches [13, 109] assumed a cylindrical bar's particular shape, parametrized by its mass, radius, and length. Here, the model is generalized, and no assumption is made about the core shape. Its shape is characterized by frequency, ellipticity, and quadrupolar mass moment. The h_0 is related to the bar parameters, while the f_0 , and τ values are the same as in the previous model. See Section 5.4.2 for more details about the new parametrizations and comparison to the previous model. In this search, we use $f_0 = \{55, 82, 122, 182, 272, 405, 604, 900, 1342, 2000\}$ Hz and $\tau = \{0.001, 0.01, 0.1, 1.0\}$ s.

The *Torus Fragmentation Instability* scenario proposes that if a black hole and an accretion disk are formed during the collapse, the disk could fragment and large self-gravitating clumps of matter falling into the black hole would produce large amplitude GWs under the appropriate conditions. Fragmentation has been observed in some simplified numerical setups but is very short-lived. However, it is currently unclear if it will develop under more realistic conditions. To model this signal, we employ a simplified model that depends on the mass of the central black hole $M_{\text{BH}} = \{5, 10\} M_\odot$ and the properties of the disk, namely the thickness of the torus $\eta = \{0.3, 0.6\}$ and the alpha viscosity parameter $\alpha = 0.1$. The torus thickness is defined as $\eta = H/r$, where H is the disk scale height, and r is the local radius. For the disk model considered in the mass of the fragmented clump is $M_f = 0.53\eta^3 M_{\text{BH}}$. The GW amplitude is proportional to the reduced mass of the BH-clump system, $\mu = M_{\text{BH}} M_f / (M_{\text{BH}} + M_f)$, which for the parameter space considered

here ($M_f \ll M_{\text{BH}}$) is $\mu \approx M_f$. Following [13], the piro1 and piro2 stand for a source with $M_{\text{BH}} = 5 M_{\odot}$ and $\eta = \{0.3, 0.6\}$, respectively. The piro3 and piro4 are for CCSNe with $10 M_{\odot}$ black holes and $\eta = \{0.3, 0.6\}$, respectively.

5.2.3.6. Ad-hoc signals. To constrain the GW energy, luminosity, and PNS ellipticity emitted by a CCSN at a given frequency bin, we use *ad-hoc* sine-Gaussian signals. Currently, the best GW energy constraints are of an order of $10^{-4} M_{\odot}$ [13], and they correspond to the energies of extremely rapidly rotating explosion models. In this search, we use elliptically polarized sine-Gaussians that represent rotating sources. The waveforms are calculated according to the Eqns. (5.3) and (5.4), and they are parametrized with central frequency $f_0 = \{55, 82, 122, 182, 272, 405, 604, 900, 1342, 2000\}$ Hz, and $\tau = \{0.001, 0.01, 0.1, 1.0\}$ s. The amplitudes do not have physical meaning.

5.3. SEARCH RESULTS

5.3.1. SN 2020fqv Loudest Event. Table 5.2 presents the search results. The most significant GW candidate is the loudest event of SN 2020fqv with a FAP of 0.54% (2.8σ). This event is analyzed in Section 5.3.1 and likely has a noise origin. All other loudest events are consistent with the background.

Table 5.2. List of the loudest events for each CCSN.

Supernova	Class	η_c	FAR [Hz]	FAP
SN 2019ehk	C2	5.9	1.4e-5	0.39 (0.86 σ)
SN 2019ejj	C2	6.7	1.1e-5	0.71 (0.38 σ)
SN 2019fcn	C2	6.7	1.4e-5	0.95 (0.06 σ)
SN 2019hsw	C1	5.6	4.5e-6	0.86 (0.17 σ)
SN 2020oi	C1	5.8	2.0e-6	0.35 (0.93 σ)
SN 2020cxd	C1	6.7	3.3e-6	0.73 (0.34 σ)
SN 2020dpw	C2	6.2	6.3e-6	0.81 (0.23 σ)
SN 2020fqv	C1	7.6	1.5e-8	0.005 (2.78 σ)

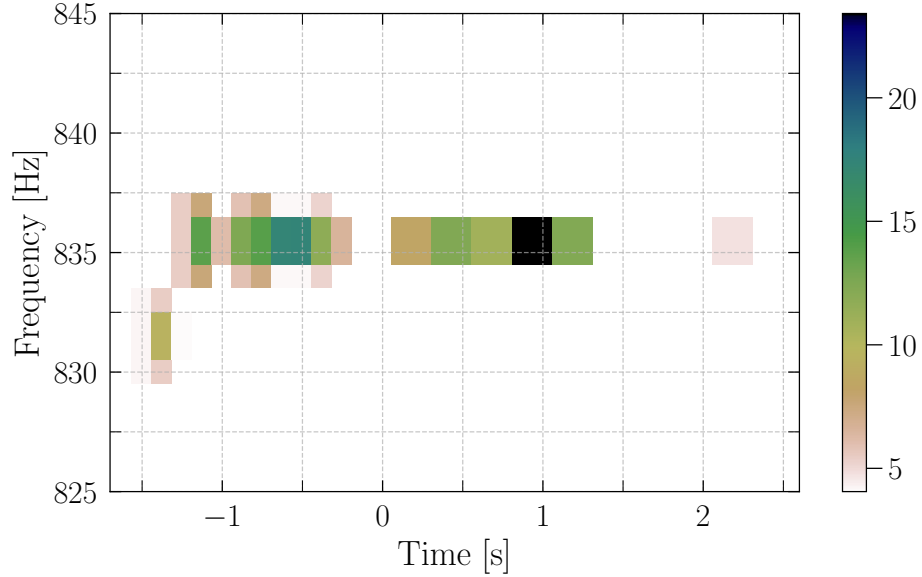


Figure 5.3. SN 2020fqv loudest event with a 2.8σ detection significance. Figure is taken from Ref. [12].

Figure 5.3 shows the time-frequency map of the SN 2020fqv loudest event. This is a long (around 4 s) and narrowband (around 4 Hz) signal with a peak frequency of 835 Hz detected with a FAR of 1 per 2.05 years. Given the OSW, the FAP is 0.54% which corresponds to 2.8σ confidence.

Investigating the data quality surrounding this event shows an 837 Hz noise feature at the LIGO Hanford observatory, ruling this event to be of instrumental origin. The same source of noise has been observed in the O3 search for long-duration transient GW to be instrumental

Apart from the data quality analysis, we consider the search sensitivity to the signals similar to this loudest event. Because it is a narrowband signal, the sine-Gaussians can be used to estimate detectability and the bar model waveforms can be used as probes. Among the analyzed waveforms, the closest is the one at a frequency of 900 Hz and $\tau = 1$ s. At the distance of SN 2020fqv (17.3 Mpc), the detection efficiency is about 23% (see the next section). Therefore, such an extreme emission can potentially explain the observed

SN 2020fqv loudest event. Alternatively, high-frequency modes are also visible in more realistic explosions. These signals are at a constant frequency if the mass accretion is low and the PNS isn't changing size.

5.3.2. Detection Efficiency vs Distance. To assess the search sensitivity, we produce detection efficiency vs distance for a wide range of CCSN models. Figure 5.4 shows the detection efficiencies of the models described in Sec. 5.2.3 for the sky location and OSW of SN 2017ejj. The numbers in the brackets are distances at 50% detection efficiencies. Horizontal dashed lines show 10%, 50%, and 90% detection efficiencies. *Left panel* shows the efficiencies for 12 CCSN models derived from multidimensional CCSN simulations. As references, the Galactic Center and Large Magellanic Cloud (LMC) distances are plotted. *Right panel* provides the detection efficiencies for the extreme emission long-lasting bar mode model. Some models are reaching the distance of SN 2019ejj. Given a null detection, it allows excluding parameter spaces of this extreme emission model as discussed in Sec. 5.4. The numbers in parentheses are detection reaches. As references, the left plot shows the distances to the Galactic Center (~ 8.5 kpc) and the Large Magellanic Cloud (49.6 kpc [193]) that hosted SN 1987A. Table 5.3 summarized the distance reached for all analyzed CCSNe. For each model, the values are consistent across the CCSNe. The largest distances are mostly achieved with SN 2020cxd.

The neutrino-driven explosions (models s11, s15, C15, L15-3, m20, m20p, s18, s3.5, s9, s13, and s25) are detectable up to a few kpc, with the s15 model being reached to the Galactic Center. When comparing the three models with solar metallicity progenitor stars (s9, s13, and s25), the distance reach increases with progenitor mass.

The magnetorotationally-driven explosion model signal_O has a larger distance reach compared to the neutrino-driven explosions. For most CCSNe, the distances exceed the Galactic Center; for a few of them, the detection probability is non-zero at the distance of the Large Magellanic Cloud. The quantum chromodynamics phase transition explosions (s50) can be reached up to around 2.1 kpc.

Table 5.3. Distance (in kpc) of the 50% detection efficiency reached for each CCSN with neutrino-driven explosions, magnetorotational explosions (signal_O), black hole formation (s40), and phase transitions (s50) models. Values in bold represent the farthest distance reached for each model. Mark ‘-’ means that the detection efficiency did not reach 50%.

(a)

Waveforms/SN	SN 2019ehk	SN 2019ejj	SN 2019fcn	SN 2019hsw
And+17 s11	-	0.72	0.58	0.70
Kur+16 s15	6.57	8.58	7.40	5.60
Kur+22 s50	-	1.57	0.80	1.82
Mez+20 C15	0.52	2.02	0.84	2.24
Mul+12 L15-3	2.47	3.23	2.46	2.33
Obe+20 signal_O	4.22	10.89	8.81	13.40
Oco+18 m20	0.18	0.62	0.50	0.60
Oco+18 m20p	0.77	0.94	0.64	0.76
Pan+21 s40	0.38	0.84	0.58	0.77
Pow+18 s18	3.05	2.61	0.83	3.85
Rad+19 s3.5	1.54	2.09	0.87	2.04
Rad+19 s9	0.16	0.31	0.22	0.17
Rad+19 s13	0.33	0.71	0.49	0.49
Rad+19 s25	3.11	2.44	1.86	2.82

(b)

Waveforms/SN	SN 2020oi	SN 2020cxd	SN 2020dpw	SN 2020fqv
And+17 s11	0.63	0.88	0.79	0.73
Kur+16 s15	6.53	8.90	8.66	6.86
Kur+22 s50	-	2.13	1.70	1.56
Mez+20 C15	1.15	2.74	2.46	2.38
Mul+12 L15-3	2.36	3.17	2.96	2.53
Obe+20 signal_O	9.52	14.65	13.43	13.42
Oco+18 m20	0.56	0.74	0.68	0.65
Oco+18 m20p	0.70	0.95	0.85	0.82
Pan+21 s40	0.61	0.94	0.90	0.81
Pow+18 s18	1.71	4.74	4.30	4.17
Rad+19 s3.5	0.94	2.38	2.24	2.17
Rad+19 s9	0.21	0.27	0.27	0.21
Rad+19 s13	0.52	0.67	0.61	0.55
Rad+19 s25	1.96	3.15	2.86	2.90

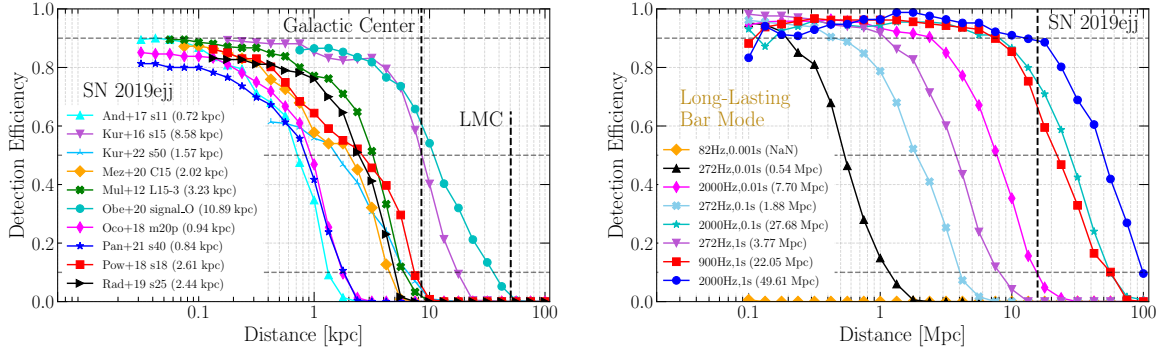


Figure 5.4. The detection efficiency as a function of distance for SN 2019ejj. Figure is taken from Ref. [12].

The right panel of Figure 5.4 shows SN 2017ejj detection efficiencies of a few GW signals from the extreme emission bar model. The detection reaches increase with signals' duration and peak frequency, up to tens of Mpc. For example, 82 Hz and 1 ms signals are not detectable at 0.1 Mpc. On the contrary, 900 Hz and 1 s signals can reach distances of the analyzed supernovae. In particular, the relatively high detection efficiency is achieved for the SN 2020fqv.

We use the L15-3 model to compare the search sensitivity between the previous searches [13, 109] and this search. In Ref. [13] a typical distance was around 1.5 kpc with a maximum of 2.4 kpc. Here, the distances are above 2 kpc with a maximum of 3.44 kpc. This corresponds to an improvement in the detectors' sensitivities of around 50%.

Detection distances were recently derived in the O3 all-sky generic LIGO-Virgo-KAGRA search [113]. They share a common model with this work: the m20 simulation. They estimate the distance at a 10% detection efficiency to be ~ 1 kpc. It is calculated at FAR of 1/100 years. In this search, the distance at a 10% detection efficiency is estimated at around 2 kpc but with a higher FAR associated with the loudest event and using a shorter time window. As explained in Sec. 5.2.2, better sensitivities are achieved with targeted searches.

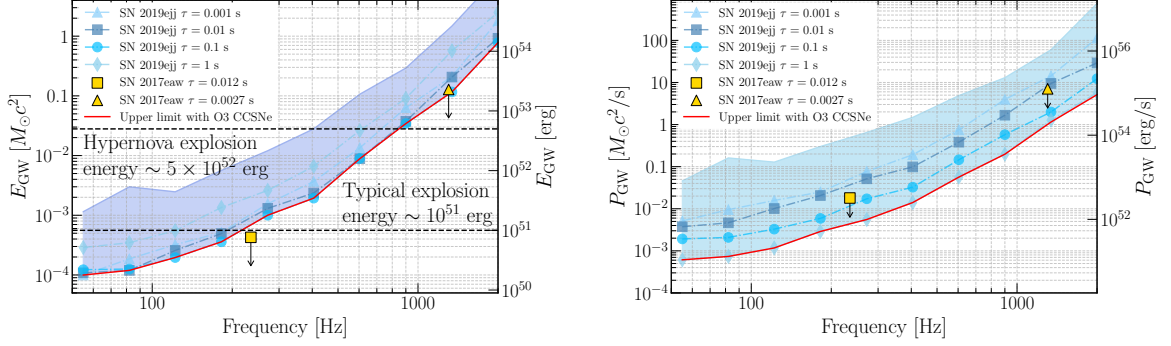


Figure 5.5. The upper limits on the GW energy (E_{GW}) and luminosity (or power, P_{GW}) emitted by a CCSN engine. Figure is taken from Ref. [12].

5.4. CCSN ENGINE CONSTRAINTS

Because no GW is found, we constrain the dynamics of the CCSN engine, similarly to Ref [13]. However, we significantly expand the statements. Rather than probing low- and high-frequency GW emission, a broad frequency spectrum is explored here. Also, the analyzed range of signal durations expanded. The constraints presented in this section can be divided into generic and modeled. The statements on the generic constraints include the upper limits on emitted GW energy, luminosity, and PNS ellipticity. Following [13], we further constrain the parameter spaces of the extreme emission models. However, the bar model is generalized compared to [13].

5.4.1. Upper Limits On GW Energy And Luminosity. Similarly to [13], we constrain the GW energy (E_{GW}) emitted by a CCSN engine. Additionally, we explore CCSN explosion's dynamics with GW luminosity (or power, P_{GW}). Assuming a rotating CCSN source, the total energy emitted in GWs is described in the previous section:

$$E_{\text{GW}} = \frac{2}{5} \frac{\pi^2 c^3}{G} D^2 f_0^2 h_{\text{rss}50}^2. \quad (5.5)$$

where f_0 is the peak frequency, D is the distance to the source and $h_{\text{rss}50}$ is an $hrss$ at 50% detection efficiency. The detection efficiencies versus $hrss$ are produced with elliptically polarized sine-Gaussians described in Sec. 5.2.3.6.

The GW luminosity is the ratio between emitted GW energy and the duration of this emission. The detector Gaussian noise and glitches affect the events' reconstructed parameters, such as duration. To minimize this bias, we use signal duration containing 90% of the signal's energy. In terms of the τ parametrization, the cWB reconstructed duration can be approximated by $1.65\tau_{\text{rec}}$. The GW power is then defined as:

$$P_{\text{GW}} = \frac{0.9E_{\text{GW}}}{1.65\tau_{\text{rec}}}. \quad (5.6)$$

The left panel of Figure 5.5 shows the E_{GW} constraints. The shaded region contains combined results from all analyzed CCSNe. From the optical observations, the typical CCSN explosion energy is around 10^{51} erg, while for hypernovae, it can be even 5×10^{52} erg. The tightest results are obtained primarily for SN 2019ejj. At 50 Hz the stringent energy constraints are $10^{-4} M_{\odot}c^2$ for signals 1 – 100 ms. The constraints obtained in the previous search [13] are also shown in the figure. At 235 Hz the GW emission was estimated with $\tau = 12$ ms, while at 1034 Hz it was $\tau = 2.7$ ms. The constraints with SN 2019ejj are around two times less stringent.

The right panel of Figure 5.5 reports on the emitted GW power. The tightest results are obtained for SN 2019ejj. The shaded region contains combined results from all analyzed CCSNe. The stringent power constraints are $5 \times 10^{-4} M_{\odot}c^2/\text{s}$ for signals at 50 Hz and 1 s long. We re-analyzed SN 2017eaw [13], and we find that the constraints with SN 2019ejj are around a factor of two less stringent.

5.4.2. Upper Limits On PNS Ellipticity. As mentioned in Sec. 5.2.3.5, the rotating core can be parametrized by its ellipticity and quadrupole mass moment. Here we provide an overview of a method.

We consider a rigid body with quadrupole mass moments I_{ij} rotating around the z-axis (no precession or nutation) with a rotational frequency f_{rot} . The resulting GW emission can be written, without loss of generality:

$$h_+ = \frac{1}{2} h_0 (1 + \cos^2 \iota) \cos(2\pi f_0 t), \quad (5.7)$$

$$h_\times = h_0 \cos \iota \sin(2\pi f_0 t), \quad (5.8)$$

where $f_0 = 2f_{rot}$ and the amplitude is:

$$h_0 = \frac{2}{D} \frac{G}{c^4} \frac{I_{xx} - I_{yy}}{2} (2\pi f_0)^2. \quad (5.9)$$

Taking an example of a triaxial ellipsoid rotating about a principal axis, the h_0 can be expressed as

$$h_0 = \frac{2}{D} \frac{G}{c^4} \frac{I_{zz} \epsilon}{2} (2\pi f_0)^2. \quad (5.10)$$

where the ellipticity is defined as [194]:

$$\epsilon \equiv \frac{I_{xx} - I_{yy}}{I_{zz}}. \quad (5.11)$$

The quantity ϵ is a measure of the core quadrupolar deformation with respect to sphericity. Because GWs considered in this search have a limited duration, we apply a Gaussian envelope to Eqns. (5.7) and (5.8) arriving then at Eqns. (5.3) and (5.4).

This model is a generalization of the one used in previously targeted searches [13, 109]. In that case, the PNS deformation was modeled by a cylinder of mass M , length L , and radius R rotating about the axis perpendicular to its length. In the current work, no assumption is made about the shape of the deformed star (only that it is rigidly rotating). If one wishes to relate the results for the new model to previous results, it is possible to relate the parameters of the new model (ϵ and I_{zz}) with the ones of the old one (M , L and R) particularizing the rigid body to a cylinder (note that f_0 and τ are common to both models)

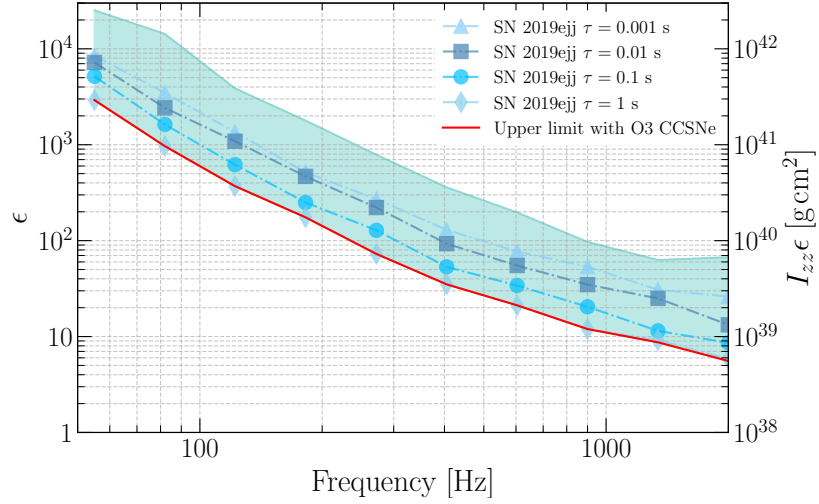


Figure 5.6. The upper limits on the PNS ellipticity. Figure is taken from Ref. [12].

such that

$$\epsilon = \frac{L^2 - 3R^2}{L^2 + 3R^2} \quad , \quad I_{zz} = \frac{1}{12}M(3R^2 + L^2). \quad (5.12)$$

This model can be used to provide upper limits on the allowed ellipticities of the core deformations. By noticing that [192] $h_{\text{rss}} = 0.708h_0\sqrt{\tau}$ one can arrive to an experimental expression of $I_{zz}\epsilon$:

$$I_{zz}\epsilon = \frac{Dc^4}{G(2\pi f_0)^2} \frac{h_{\text{rss}50}}{0.708\sqrt{\tau_{\text{rec}}}}, \quad (5.13)$$

where $h_{\text{rss}50}$ is an h_{rss} value at 50% detection efficiency, and τ_{rec} is signal duration, both are estimated from cWB. Figure 5.6 reports upper limits on the ellipticity for a range of GW signal frequencies and durations. The shaded region contains combined results from all analyzed CCSNe. Assuming a principal canonical moment of inertia for neutron stars, $I_{zz} = 10^{45} \text{g cm}^2$, the stringent upper limits on the ellipticities are down to around 5 at 2 kHz. The degree of deformation ϵ can also be presented assuming a principal canonical moment of inertia for neutron stars, $I_{zz} = 10^{45} \text{g cm}^2$. The stringent upper limits on ellipticity are obtained for the signals with $\tau = 1 \text{ s}$, ranging from 10^4 at the lowest search frequency to 10 at 2 kHz. The ϵ values increase with shorter signals.

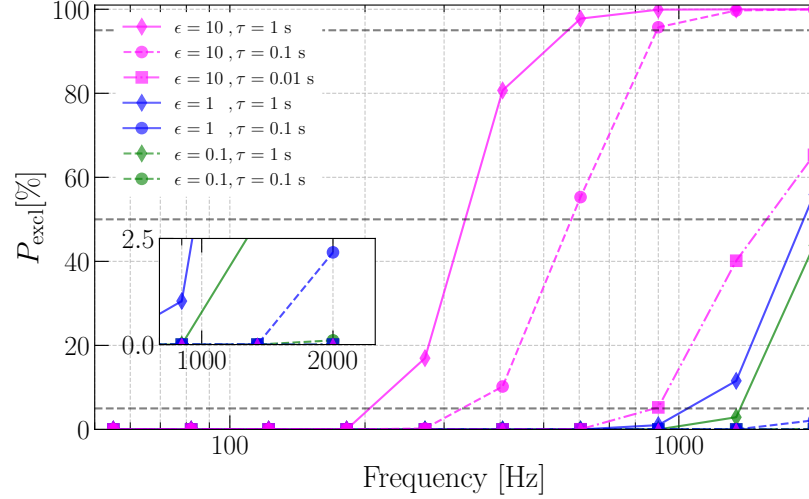


Figure 5.7. Model exclusion probability P_{excl} for long-lasting bar mode instability model. Figure is taken from Ref. [12].

5.4.3. Model Exclusion Statements. The previous search [13] excluded the parameter spaces of two extreme emission models. Here, we continue this effort. The model exclusion probability of combined N CCSNe is calculated as:

$$P_{\text{excl}} = 1 - \prod_{i=1}^N (1 - \varepsilon_i(D_i)). \quad (5.14)$$

The $\varepsilon(D) = a \times \mathcal{E}(D)$ is a detection efficiency $\mathcal{E}(D)$ reduced by the coverage duty factor $a = T_{\text{coinc}}/\Delta t$ (see Table 5.1).

The previous search [13] assumed a standard candle approach (the CCSN source is optimally oriented). Here, this approach is generalized to all possible source orientations. The CCSNe from O1 and O2 are then re-analyzed, and Figure 5.7 shows the model exclusion probabilities combining results from O1, O2, and O3 CCSNe. The numbers are calculated by accumulating results from CCSNe in O1, O2, and O3. The GW emissions from bars with $\epsilon = 10$ are excluded at almost 100% confidence above 900 Hz for $\tau = 1$ s and $\tau = 0.1$ s. The probabilities decrease with signal ellipticities and durations. The emissions with the ellipticity of 0.1 and $\tau = 1$ s are excluded up to around 50%. GW emission with

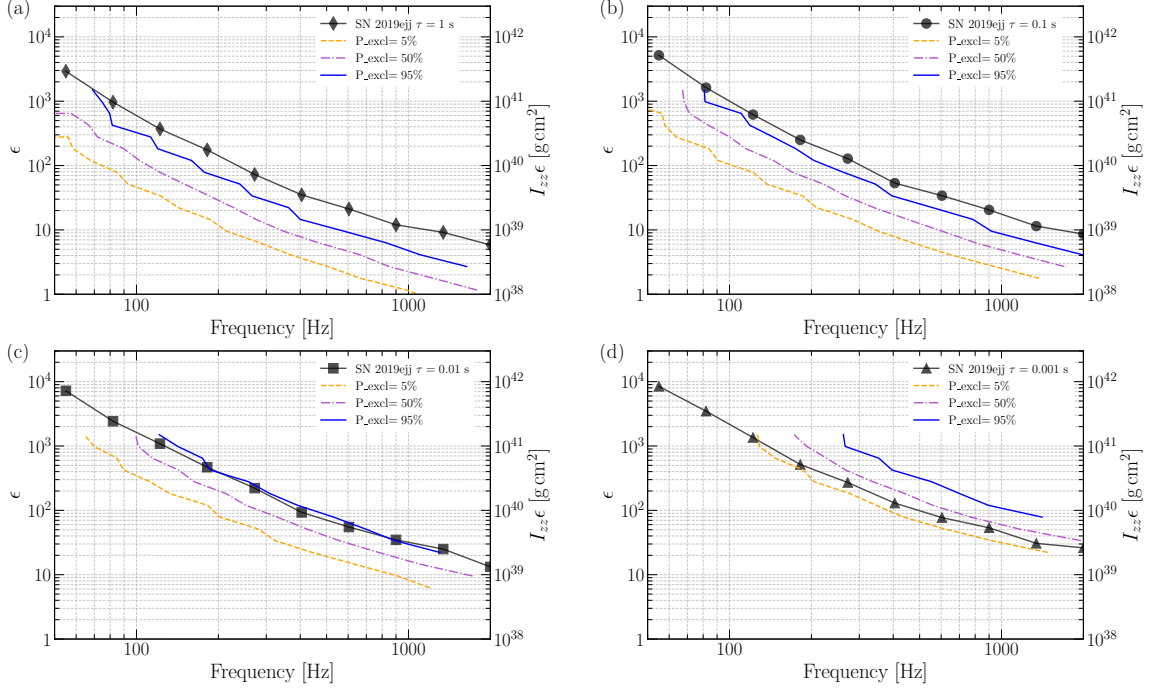


Figure 5.8. The constraint of the PNS ellipticity for the long-lasting bar model using a population of the CCSNe analyzed in this and the previous [13] search. Figure is taken from Ref. [12].

$\tau = 1$ ms cannot yet be excluded. The P_{excl} values are comparable between combined O1-O2 results [13] and this search. The model exclusion probabilities decrease with the PNS ellipticities. For $\epsilon = 10$, the emissions of $\tau = 1$ s and $\tau = 0.1$ s are excluded up to 100% for high-frequency emission (900 Hz and above). For emissions with $\tau = 0.1$ s at 2 kHz are excluded at around 50%. The emissions with $\tau = 0.1$ s and ellipticities of 1 and 0.1 cannot be yet reliably excluded, but they are non-zero. Finally, for $\tau = 0.001$ s, the emissions cannot be yet constrained. Interpreting these results, if bars are created in CCSNe, they are rather short-lived.

The analysis with O3 CCSNe allows further constraining of the fragmentation instability model (Sec. 5.2.3.5) analyzed in [13]. The model exclusion probabilities for piro2 and piro4 obtained with this search are 10.6% and 93.9%. The cumulative P_{excl} values with O1, O2, O3 CCSNe for piro1-piro4 are 0, 41.3%, 5.2% and 99%. These results

further assure us that if clumps of matter are formed in type-II and type-Ib/c supernovae, these clumps are small compared to the central black holes. Additionally, if the torii are created around black holes, they are either non-fragmented or rather thin.

5.4.4. Ellipticity Constraints For The Bar Model. Section 5.4.2 provides generic upper limits of the ellipticity based on single CCSN targets using ad-hoc sine-Gaussians. Here, a population of CCSNe used in this and the previous search [13] is used to find upper limits on the ellipticity for the long-lasting bar model. These constraints are derived from the model exclusion statements. Because the signal amplitudes are proportional to the ellipticity (Eqn. 5.10), we can probe the continuous values of the ellipticities. This method provides constraints at chosen confidence levels; here, we take 5%, 50%, and 95%.

Figure 5.8 shows the ellipticity constraints for the four signal durations. Compared with the generic ellipticity constraints, these upper limits are more stringent for τ of 1 s, 0.1 s, and 0.01 s, and are less stringent for shorter signals. At 2 kHz GW emission, we constrain the core deformation to $\epsilon = 1$. Note that for a bar model, the frequency of GW emission is twice the rotational frequency. These constraints do not span the full frequency band because some GW signals have very low detection efficiencies at smaller analyzed distances. See Figure 5.4 for 82 Hz and 1 ms example signal with a zero detection efficiency across the analyzed source distances. In such a case, it's not possible to achieve even $P_{\text{excl}} = 5\%$.

Recent CCSN simulations show bar mode instabilities appearing with an amplitude of 10^{-21} at around 300 Hz [189] or 10^{-20} at around 800 Hz [190]. Taking $I_{zz}\epsilon = 0.1 \times 10^{45} \text{g cm}^2$, or $\epsilon = 0.1$ for a canonical moment of inertia for neutron stars, one gets similar amplitudes at these two frequencies using the bar model. It is around an order of magnitude from the obtained upper limits.

5.5. SUMMARY AND DISCUSSION

We present the results of a search for GWs in coincidence with CCSNe observed optically during the third observing run of the LIGO and Virgo detectors. For eight CCSNe, all within a distance of around 30 Mpc, we calculated windows where a GW transient could be found: SNe 2019ehk, 2019ejj, 2019fcn, 2019hsw, 2020oi, 2020cxd, 2020dpw, 2020fqv. The loudest event of SN 2020fqv has a significance of 2.8σ , but the detailed analysis indicates that this event most likely has a noise origin. The loudest events from all other CCSNe are consistent with the background.

For the analyzed waveforms from multidimensional CCSN simulations, the distances at 50% detection efficiency do not reach beyond Milky Way. For neutrino-driven explosions, these distances are up to 8.9 kpc. Because the GW emissions are typically larger for magnetorotationally-driven explosions, the distance reaches are further, up to 14.7 kpc for the analyzed model. For the selected black hole formation and quantum chromodynamics phase transition models they are up to 0.9 kpc and 2.1 kpc, respectively. However, the distances for extreme emission models can be further than those of the analyzed CCSNe. This allows further constraining of the CCSN engine.

We provide generic CCSN engine constraints and those for the extreme emission models. The generic constraints include upper limits on the GW energy, and, for the first time, GW luminosity and PNS ellipticity. The analysis is performed across a wide frequency range from 50 Hz to 2 kHz. At frequencies less than 900 Hz the obtained energies are below 10^{51} erg (a typical CCSN explosion energy). The upper limits of around $10^{-4} M_{\odot} c^2$ are at frequencies below 100 Hz for signals with durations 1 – 100 ms. After re-analyzing SN 2017eaw [13], our constraints are less stringent by a factor of around two.

We report generic constraints of the PNS ellipticity, $I_{zz}\epsilon$. Assuming the principal canonical moment of inertia for a neutron star ($I_{zz} = 10^{45} \text{ g cm}^2$), the upper limits for $\tau = 1$ s are down to $\epsilon = 5$ for GW signals 2 kHz and they increase above 10^3 for the lowest frequencies. These upper limits are becoming less stringent for shorter signal durations.

By combining the results obtained with the data from O1 and O2 [13], we improve the constraints of the parameter spaces of the extreme emission models assuming a standard candle approach. Specifically, the long-lasting bar mode models are analyzed in more detail compared with [13]. The most stringent constraints are at high frequencies, down to $\epsilon = 1$ for 1 s long emission. These constraints are less stringent for shorter signals. We note that the obtained ellipticities are roughly an order of magnitude larger than those obtained from the recent CCSN simulations [189, 190].

The targeted search with O1-O2 data [13] allowed, for the first time, constraining the CCSN engine. While this search has not improved the upper limits on the GW energy emission, the upper limits on GW luminosity and PNS ellipticity are reported for the first time. By combining O1, O2, and O3 data, the extreme emission models are constrained further compared to [13]. The obtained ellipticities of the rotating cores are around an order of magnitude above the largest obtained in CCSN simulations. Future observing runs with improved sensitivities have the potential to accumulate enough statistics to constrain the CCSN simulations. Moreover, our results indicate that near-future data might be able to observationally constrain other CCSN models, such as core fragmentation or higher $T/|W|$ effects, and others.

5.6. ORIGINAL CONTRIBUTION

This section is built on the collaborative work with M. Szczepańczyk and others, titled “An Optically Targeted Search for Gravitational Waves Emitted by Core-Collapse Supernovae during the Third Observing Run of Advanced LIGO and Advanced Virgo,” available as an arXiv preprint, arXiv:2305.16146, 2023. It has been reviewed in the LVK group.

My contributions to this work include leading the closed-box analysis for two CCSNe candidates, reviewing and finalizing the analysis results for all studied CCSNe, managing the open-box phase of the search, authoring the code for estimating constraints on energy, power, and ellipticity, and calculate model exclusion probabilities.

6. DETECTING GWS FROM THE NEXT GALACTIC CORE-COLLAPSE SUPERNOVA IN THE ADVANCED DETECTOR ERA

Detecting GWs from CCSN presents a formidable challenge due to the inherently weak signals that most current detectors are tuned to capture. As of now, only GWs emitted from CCSNe within our galaxy stand a reasonable chance of being detected. Meanwhile, a plethora of simulated GW signals, each possessing unique characteristics, are being studied to understand the potential features of these elusive emissions.

The current O4 observing runs and the forthcoming O5 runs bring renewed hope and enthusiasm to the scientific community due to recent technological advancements. These upgrades to the detectors may significantly increase the likelihood of making a groundbreaking discovery, such as the first-ever detection of GW originating from a CCSN within the Milky Way. In light of these technological advancements and the expanding catalog of simulated GW signals, it becomes increasingly important to understand the feasibility of detecting GWs from the next Galactic or near extra-Galactic CCSN with the planned observations and revisit some of the previous results.

Heightening the significance of these discussions was a noteworthy event that occurred during LIGO's 15th engineering run before the O4 observing run. A CCSN explosion was observed in the host galaxy Messier 101, named SN 2023ixf, and located approximately 6.7 Mpc away from Earth. The color-composite image can be seen in Figure 6.1. Remarkably, this is one of the closest supernovae to be observed in the last decade, rivaled only by SN 2017eaw, which was discovered in 2017 at an equivalent distance of 6.7 Mpc. SN 2023ixf is classified as a Type II supernova and captured significant attention from the scientific community. Various studies have been conducted to date, examining diverse aspects of its characteristics and behavior. The event was observed on May 19th, coinciding with a period during which LIGO was actively collecting data within its on-source window.

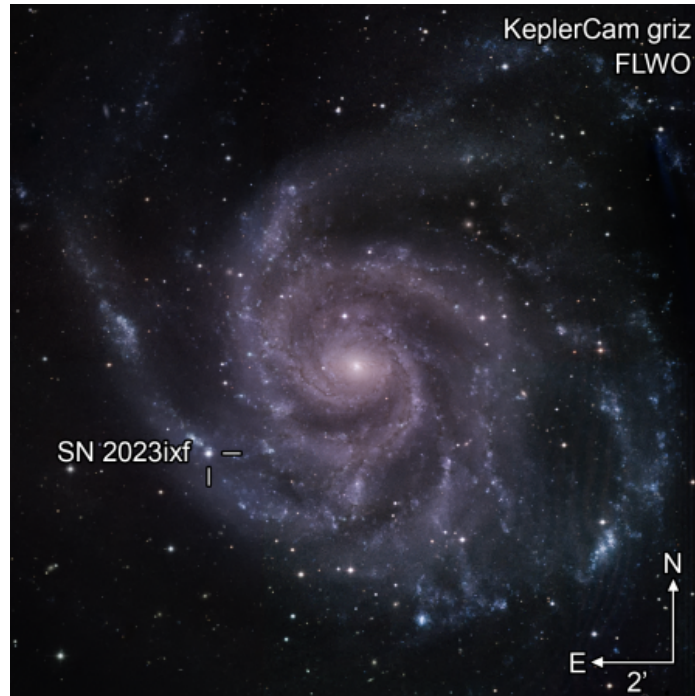


Figure 6.1. Color-composite image of SN 2023ixf and its host galaxy M101 taken by the Fred Lawrence Whipple Observatory.

Current efforts are underway to search for GWs emitted from this supernova. Even if no direct signals are detected, the analysis will enhance our understanding by placing improved constraints on parameters such as energy emission and luminosity compared to O3.

In this section, an extensive analysis of simulated state-of-the-art GW signals is performed. Using a large set of predicted GW signals, we provide basic properties, compare their energy evolution, spectra, and list the dominant emission processes. Meanwhile, the predictions of detection sensitivity for O4 and O5 observing runs are made. By rescaling O2 data to align with the sensitivities of the O4 and O5 runs while maintaining the characteristics of the noise, we calculate the distance and minimum SNR at which predicted GW signals could potentially be detected.

6.1. CCSN MODELS

Despite more than half a century of efforts to comprehend the evolutionary mechanisms of CCSN [195], the intricacies of their dynamics remain elusive due to the involvement of highly complex physics that leaves many questions unanswered. While initial calculations were restricted to one- and two-dimensional models, considerable strides have been made recently with the advent of full, self-consistent, three-dimensional simulations. However, the number of publicly accessible GW signals generated by these 3D simulations remains limited, largely owing to the computational resources required for their extraction.

We analyzed 82 waveforms from 18 waveform families. We study waveforms from 2D and 3D simulations that were available at the beginning of the analysis. We do not analyze GW signals from older simulations (e.g. [196, 197, 198, 199, 200]) and those that became available during our analysis (e.g. [201, 202, 203, 204, 205]). The set reflects the landscape of available GW signals for a variety of progenitor star parameterizations, physics approximations, and GW signal properties.

The approximations in the numerical setup of the simulations affect GW production. The axisymmetric 2D models produce by definition linearly polarized signals (h_+ and $h_\times = 0$), while two polarizations (h_+ and h_\times) are available for 3D simulations. The equation of state (EOS) of the dense matter is an important ingredient, they can range from softer to stiffer and they may alter GW signatures. The EOSs used in these waveforms are: LS, LS180, LS220 [206]; Shen [207]; DD2, TM1 [208]; SFHx, SFHo [209]; and others. Various efforts are conducted for approximating General Relativity, neutrino treatment and other physical processes. Some of the approaches used to calculate waveforms we analyze are: CoCoNuT [210], CoCoNuT-FMT [211], PROMETHEUS [212], CHIMERA [213], FLASH [214], Zelmani [215], JM (Janka & Müller [216]), Pen (Pen et al. [217]), and 3D-GR [218].

For all waveforms, we provide information about the progenitor star masses M_{star} that range from $3.5 M_{\odot}$ to $60 M_{\odot}$. The $3.5 M_{\odot}$ progenitor is an ultra-stripped helium star and all other progenitors have zero-age main-sequence (ZAMS) masses. The rotation of the stars is modeled to be differential and initial central angular velocity Ω_c is provided. The peak frequency f_{peak} is calculated from the energy spectra and the GW energy E_{GW} is the source angle averaged. The waveform duration is the time from the moment of the collapse until the end of the simulations. Due to a large computational cost, some of the simulations are stopped before the full GW signal develops. Here gives the brief overview of three waveform families:

Kuroda et al. 2016 [80] (Kur+16) study the impact of the EOSs on the GW signatures using a $15 M_{\odot}$ progenitor star. GW emission in the pre-explosion phase strongly depends on whether the post-shock flow is dominated by the SASI/convection and g-mode components in their signals. For the TM1 waveform, only one angle orientation was available to analyze.

Kuroda et al. 2017 [219] (Kur+17) is a continuation of Kur+16 work. Two additional explosions are analyzed, with $11.2 M_{\odot}$ and $40 M_{\odot}$ progenitor stars. Their study suggests a correlation between neutrino fluxes and GWs from the SASI. For both waveforms only one angle orientation was available.

Radice et al. 2019 [78] (Rad+19) explore the dependence of the GW properties on the progenitor star mass, which ranges from $9 M_{\odot}$ to $60 M_{\odot}$. The signals are dominated by f- and g-modes, but some of them also show strong SASI or prompt-convection signatures. We analyzed 10 waveforms: s9, s10, s11, s12, s13, s14, s15, s19, s25, s60.

6.2. GWS CALCULATION

As described in the first section, the GWs under TT gauge can be written as:

$$\mathbf{h}_{ij}^{TT} = h_+ \mathbf{e}_+ + h_{\times} \mathbf{e}_{\times} . \quad (6.1)$$

where \mathbf{e}_+ and \mathbf{e}_\times are unit plus and cross polarization tensors. Using a coordinate transformation between Cartesian and spherical coordinates, the GWs radiated in the (θ, ϕ) direction are expressed as [220]:

$$h_+ = \frac{1}{D} \frac{2G}{c^4} (\ddot{Q}_{\theta\theta} - \ddot{Q}_{\phi\phi}), \quad (6.2)$$

$$h_\times = \frac{1}{D} \frac{G}{c^4} \ddot{Q}_{\theta\phi}. \quad (6.3)$$

where:

$$\begin{aligned} \ddot{Q}_{\theta\phi} = & (\ddot{Q}_{22} - \ddot{Q}_{11}) \cos \theta \sin \phi \cos \phi \\ & + \ddot{Q}_{12} \cos \theta (\cos^2 \phi - \sin^2 \phi) \\ & + \ddot{Q}_{13} \sin \theta \sin \phi - \ddot{Q}_{23} \sin \theta \cos \phi. \end{aligned} \quad (6.4)$$

$$\ddot{Q}_{\phi\phi} = \ddot{Q}_{11} \sin^2 \phi + \ddot{Q}_{22} \cos^2 \phi - 2\ddot{Q}_{12} \sin \phi \cos \phi. \quad (6.5)$$

and

$$\begin{aligned} \ddot{Q}_{\theta\theta} = & (\ddot{Q}_{11} \cos^2 \phi + \ddot{Q}_{22} \sin^2 \phi + 2\ddot{Q}_{12} \sin \phi \cos \phi) \cos^2 \theta \\ & + \ddot{Q}_{33} \sin^2 \theta - 2(\ddot{Q}_{13} \cos \phi + \ddot{Q}_{23} \sin \phi) \sin \theta \cos \theta. \end{aligned} \quad (6.6)$$

In the case of axisymmetric 2D simulations, the cross polarization is zero. The Q_{ij} matrix has only diagonal components, $Q_{11} = Q_{22} = -\frac{1}{2}Q_{33}$, and the GW strain h_+ is related to \ddot{Q}_{ij} as [221]:

$$h_+ = \frac{1}{D} \frac{G}{c^4} \frac{3 \sin^2 \theta}{2} \ddot{Q}_{33}. \quad (6.7)$$

where θ is an inclination angle.

We use \ddot{Q}_{ij} to analyze the waveforms and provide basic properties, such as the total energy, energy evolution, energy spectrum, and the characteristic strain. The total energy is calculated as:

$$E_{GW} = \int_{-\infty}^{\infty} \frac{dE_{GW}}{dt} dt . \quad (6.8)$$

where [222, 223]:

$$\begin{aligned} \frac{dE_{GW}}{dt} = \frac{G}{5c^5} (\ddot{Q}_{11}^2 + \ddot{Q}_{22}^2 + \ddot{Q}_{33}^2 + \\ 2(\ddot{Q}_{12}^2 + \ddot{Q}_{13}^2 + \ddot{Q}_{23}^2)) . \end{aligned} \quad (6.9)$$

The energy spectrum is:

$$\begin{aligned} \frac{dE_{GW}}{df} = \frac{G}{5c^5} (2\pi f)^2 (|\ddot{Q}_{11}|^2 + |\ddot{Q}_{22}|^2 + |\ddot{Q}_{33}|^2 + \\ 2(|\ddot{Q}_{12}|^2 + |\ddot{Q}_{13}|^2 + |\ddot{Q}_{23}|^2)) . \end{aligned} \quad (6.10)$$

where \tilde{Q}_{ij} is a Fourier transform of Q_{ij} :

$$\tilde{Q}_{ij}(f) = \int Q_{ij}(t) e^{-i2\pi ft} . \quad (6.11)$$

The characteristic strain is defined as [224]:

$$h_{char} = \frac{1}{D} \sqrt{\frac{2G}{\pi^2 c^3} \frac{dE_{GW}}{df}} . \quad (6.12)$$

6.2.1. Energy And Spectra Of GW Signals. Figure 6.2 shows the source orientation averaged GW energy as a function of the peak frequency f_{peak} (frequency of the $dE_{GW}(f)/df$ maximum value) for all analyzed waveforms. In the plot, we show the typical explosion energy of a CCSN that is 10^{51} erg (approximately kinetic energy of the ejecta), and the current best GW energy constraint at low frequency is below this limit ($4.27 \times 10^{-4} M_{\odot} c^2$ at 235 Hz [225]). Energies of most of the waveforms are in the $10^{-10} - 10^{-7} M_{\odot} c^2$ range with

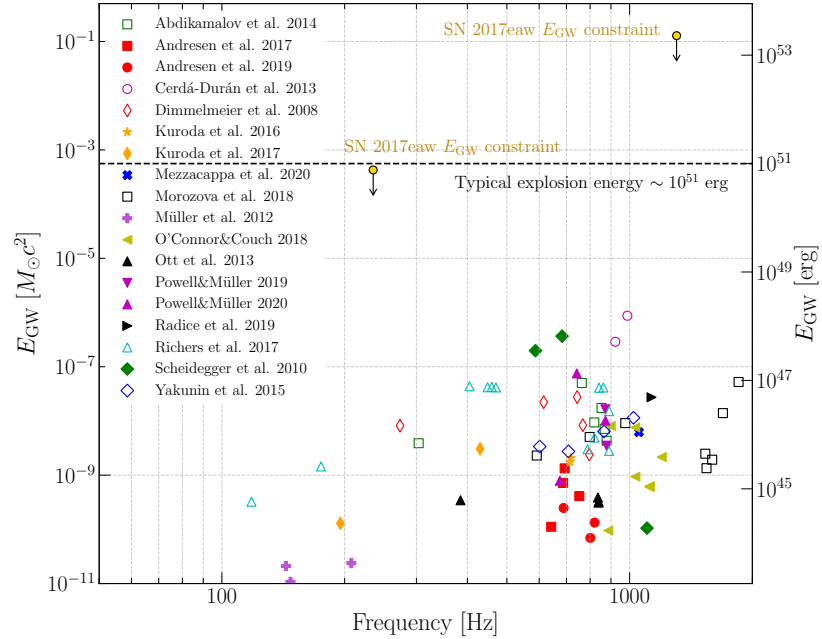


Figure 6.2. GW energy as a function of peak frequency (maximum of dE_{GW}/df) for 82 analyzed waveforms. Figure is taken from Ref. [14].

more energetic emissions involving rapid rotation (Cer+13, Sch+10 and Ric+17). Only less than 0.01% of the explosion energy appears to be converted into GWs. The peak frequencies range from 100 Hz to above 2 kHz with the majority of the energy emitted around 1 kHz.

Figure 6.3 shows example curves of the cumulative energy emitted in GWs as a function of time after core bounce. As described earlier, a CCSN explosion can be divided into a few phases that can be observed in the curves. A core bounce and quiescent phase are followed by a period of accretion and strong GW emission until an explosion phase occurs with typically little accretion and weak GWs. The timescales and the strengths differ between waveforms. Since many simulations are stopped abruptly due to the high computational cost, the GW evolution is stopped before the full signal is evolved. For example, the Abd+14 waveforms represent the bounce signal of a rapidly rotating core and the later evolution is not yet well understood.

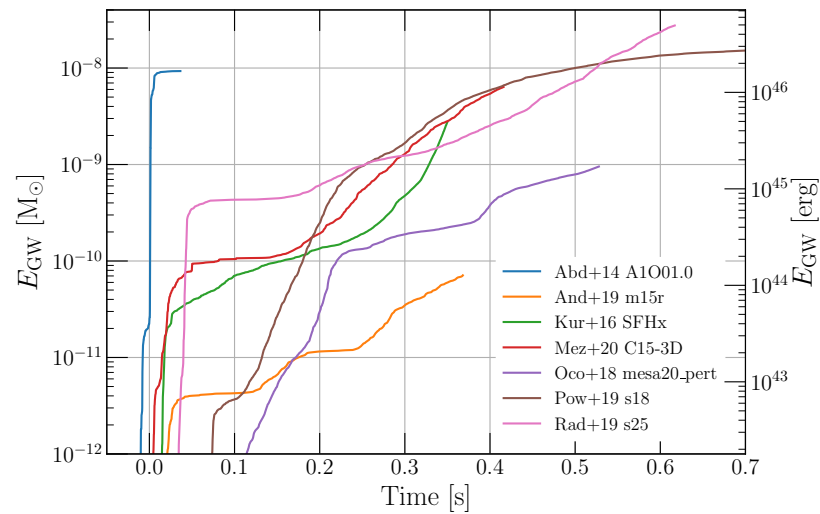


Figure 6.3. Examples of the GW energy evolution. Figure is taken from Ref. [14].

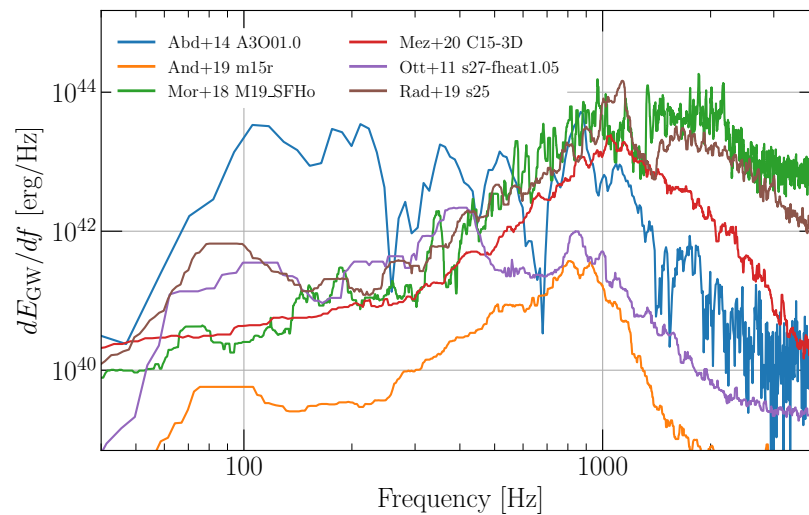


Figure 6.4. The GW signals from CCSNe are typically broadband with the majority of the energy at higher frequencies. Figure is taken from Ref. [14].

Figure 6.4 shows the GW energy spectra dE_{GW}/df for a few example waveforms. The GW signals are usually broadband with the majority of the energy at higher frequencies. The dominant GW emission comes typically from the PNS oscillations. In the case of the Ott+03 model, the explosion is initially very aspherical and the prompt-convection signal around 400 Hz dominates. In some cases, the peak frequencies cannot be determined unambiguously, for example, the Abd+14 waveforms have multiple peaks in their spectrum.

6.2.2. Characteristic Strains. Figure 6.5 presents the characteristic strains for example waveforms together with the noise amplitudes of LIGO, Virgo, and KAGRA detectors projected for O4 and O5 [226]. The GW150914 signal is also shown for comparison. The GW detector sensitivities are frequency-dependent and it impacts the detectability of GW features. The stronger GW emission from PNS oscillations peaks in a less sensitive area of the detector spectrum. The GWs from lower frequency SASI/convection have the majority of their energy in the frequency range where the detectors are most sensitive.

6.3. NOISE RESCALING

The GW detectors are impacted by many sources of noise. The data is non-stationary, the amplitudes may fluctuate vastly, and it is corrupted by non-Gaussian noise. Every upgrade of the GW interferometers alters the noise properties. The astrophysical predictions with the projected detector sensitivities should take into account the features of the real detector noise. Therefore, we rescale publicly available O2 data from LIGO Livingston (L1), LIGO Hanford (H1), and Virgo (V1) detectors to the projected sensitivities in O4 and O5 [226]. The data from the KAGRA (K1) detector is not yet available so a Gaussian noise is scaled to projected O4 and O5 sensitivity.

We developed a procedure that allows us to preserve all features of the noise, including the distributions of glitches, fluctuations of the detector spectra, and other noise sources present in the real data. The rescaling procedure uses an average detector noise spectrum from O2, $S_{\text{O2,avg}}(f)$ [227, 228] and the projected detector sensitivity O5 $S_{\text{O5,proj}}(f)$. The

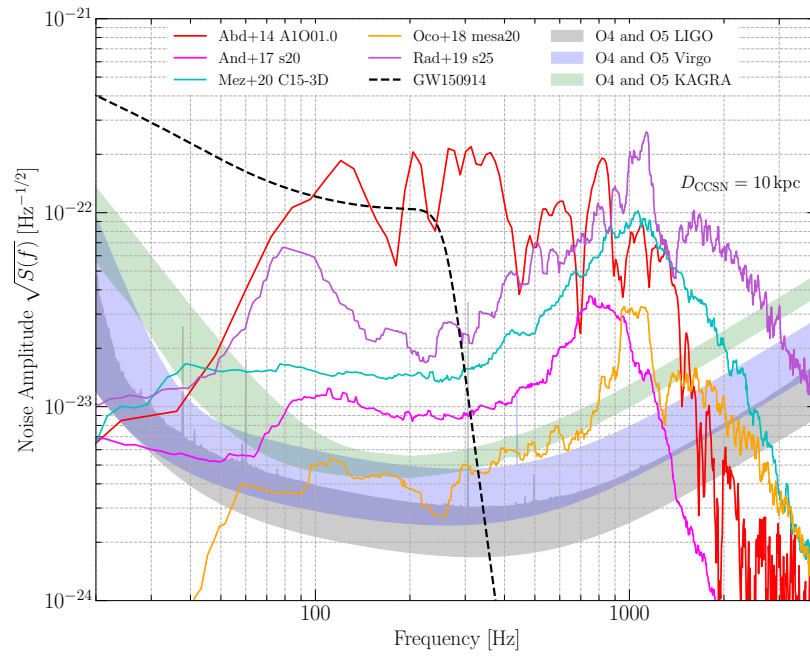


Figure 6.5. The projected noise amplitudes of the LIGO, Virgo, and KAGRA detectors for O4 and O5. Figure is taken from Ref. [14].

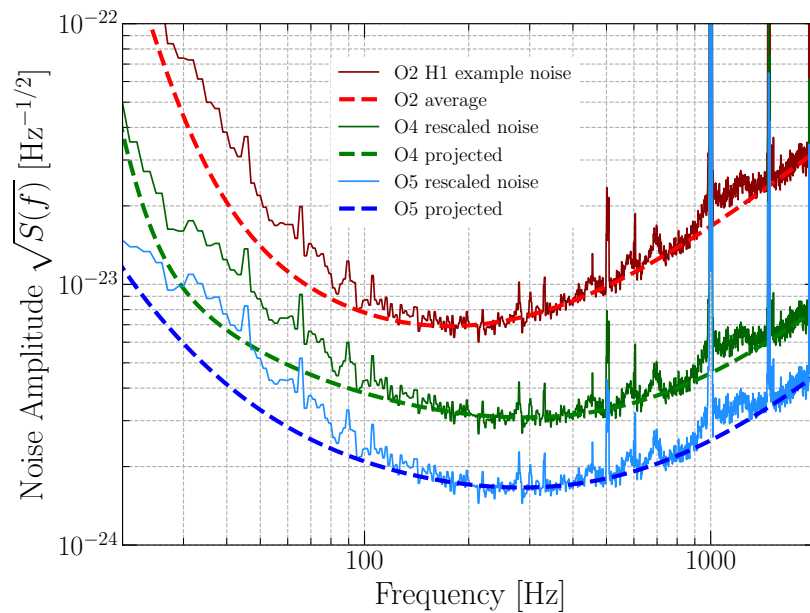


Figure 6.6. Example O2 LIGO Hanford detector sensitivity rescaled to O4 and O5 designs. Figure is taken from Ref. [14].

algorithm takes time series from O2, calculates the spectrum $S_{O2}(f)$ and rescales it in the frequency domain as:

$$S_{O5}(f) = S_{O2}(f) \frac{S_{O5,proj}(f)}{S_{O2,avg}(f)}. \quad (6.13)$$

The phase is preserved and the rescaled spectra are transformed back to the time domain. The same procedure is performed with O4 data. Figure 6.6 shows an example of the spectra of the original H1 O2 data that is rescaled to O4 and O5, an average noise in O2, and the projected O4 and O5 sensitivities. In this example, the algorithm preserves the lower H1 sensitivity below 100 Hz and a noise excess around 1 kHz.

6.4. RESULTS FROM SENSITIVITY STUDIES

We determine how sensitive the cWB search is to detect and reconstruct CCSN waveforms. The waveforms from different source angle orientations are placed randomly in the sky, added (injected) to the detector noise every 150 s and reconstructed with cWB. This procedure is performed for a range of source distances creating detection efficiency curves. For each waveform, the distance at 50% detection efficiency is referred to as a *detection range*. A similar procedure is performed with detection efficiency curves as a function of network SNR. The waveforms are placed randomly in the sky and their amplitudes are rescaled to match certain injected SNR (SNR_{inj}). This allows us to determine how strong the GW signal needs to be to be detected by cWB. The *minimum detectable SNR* is referred to as the SNR at 50% detection efficiency.

In this search sensitivity study, we use 10 days of coincident data from O2 rescaled to projected O4 and O5 sensitivities. This extended period of data allows us to average the impact of the detector network angular sensitivity and the effects of the noise. We discard events with FAR larger than 1 per year. For a GW signal from a nearby CCSN, the Supernova Early Warning System (SNEWS) [229] should provide a conservative period of 10 s to identify the GW burst. Assuming that the GW is detected with FAR smaller

than 1 per year, it results in a 5σ detection confidence (see Eqn. (1) in [225]). In case when a neutrino counterpart is not available, the time of the GW burst would have to be estimated from optical observations [225] that will likely be more uncertain than the time from SNEWS therefore decreasing the detection significance.

6.4.1. Detection Ranges. The detection ranges for the projected sensitivities of the LIGO detectors in O4 and O5 are presented in Figure 6.7. Top panels of Figure 6.7 provide example detection efficiency curves for projected O5 LIGO sensitivities. Bottom panel of Figure 6.7 summarize distances at 10%, 50% and 90% detection efficiencies for all analyzed waveforms.

In Figure 6.7, a detection efficiency curve for a certain waveform can be interpreted as the probability of detecting that waveform as a function of the source distance. The numbers in the brackets are the detection ranges (distances at 50% detection efficiency). The values vary significantly, from around 1 kpc to over 100 kpc. The maximum values of the detection efficiency curves for waveforms calculated in 3D simulations are above 90% while it is around 70% for linearly polarized GW signals. The HL network used for this analysis is sensitive effectively to only one polarization (the arms of H1 and L1 detectors are approximately parallel). Depending on the polarization angle a waveform may not be registered at the output of the detectors, even if the amplitude is large compared to the noise level. Notably, the best-studied bounce signal has only one polarization component and with 30% probability, the signal will not be detectable even for a very nearby CCSN.

The bottom panel of Figure 6.7 provides a broad overview of how well the GW signals from CCSNe can be detected in O5. Typically, the detection ranges for the waveforms generated in neutrino-driven explosions are up to around 10 kpc and only a few GW signals can be detected up to the edge of the Milky Way. When a star explodes according to the MHD-driven mechanism, the detection ranges may exceed the distance of the Large Magellanic Cloud (49.6 kpc [230]). The largest detection ranges are obtained for Sch+10 (around 100 kpc for R3E1AC_L and R4E1CA_L) and Pow+20 (60 kpc for y20). These results are in

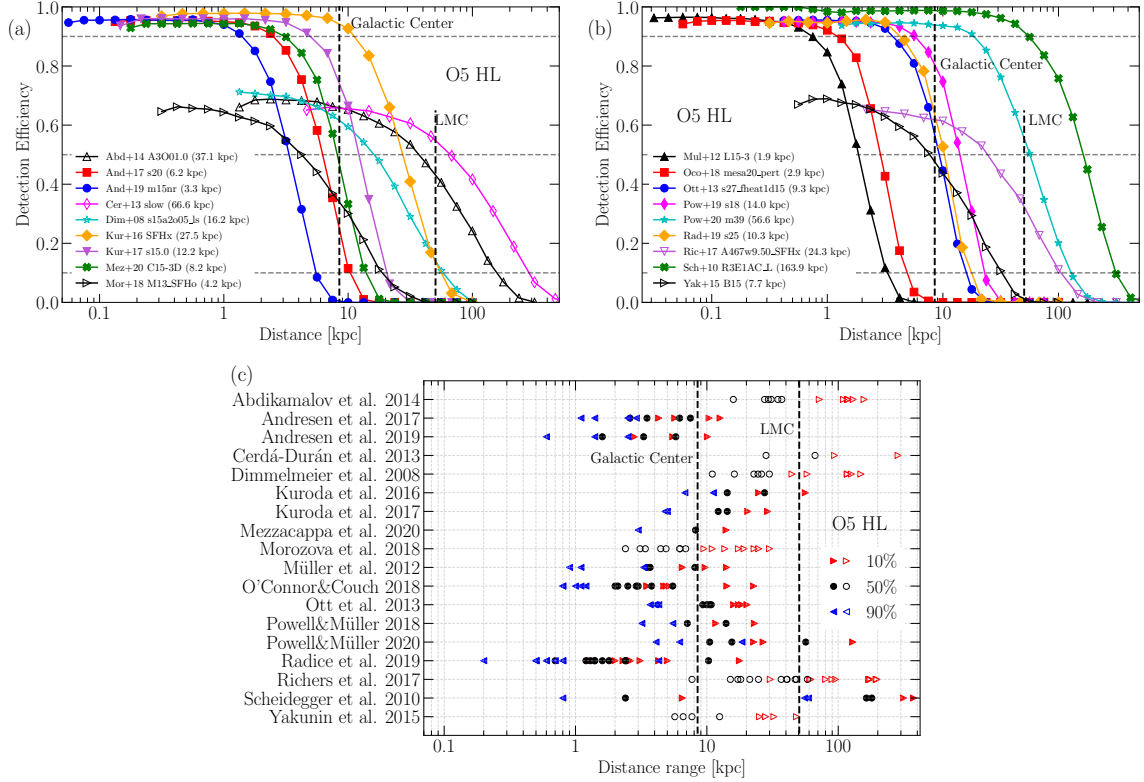


Figure 6.7. Detection efficiency curves for example waveforms are presented in panels (a) and (b). Panel (c) shows the distances at 10%, 50% and 90% detection efficiencies for all waveforms analyzed. Figure is taken from Ref. [14].

a qualitative agreement with previous studies and conclusions from the optically targeted search performed with O1-O2 data [225, 231] where the detection ranges for MHD-driven explosions are much larger than for neutrino-driven explosions. It is worth mentioning that the detection ranges for the MHD-driven explosions could increase significantly if the amplitudes of the turbulent phase (not available for Abd+14, Dim+08, and Ric+17) are comparable with the core bounce one.

6.4.2. Minimum Detectable SNR. The cWB algorithm is sensitive to a wide range of GW signals but it is not equally sensitive to all morphologies. In general, waveforms that are short and narrowband are easier to detect than waveforms that are long, broadband, or fragmented in the time-frequency domain. As an illustration, binary BH signals usually have a continuous evolution in the time-frequency domain, in the LIGO band they are typically

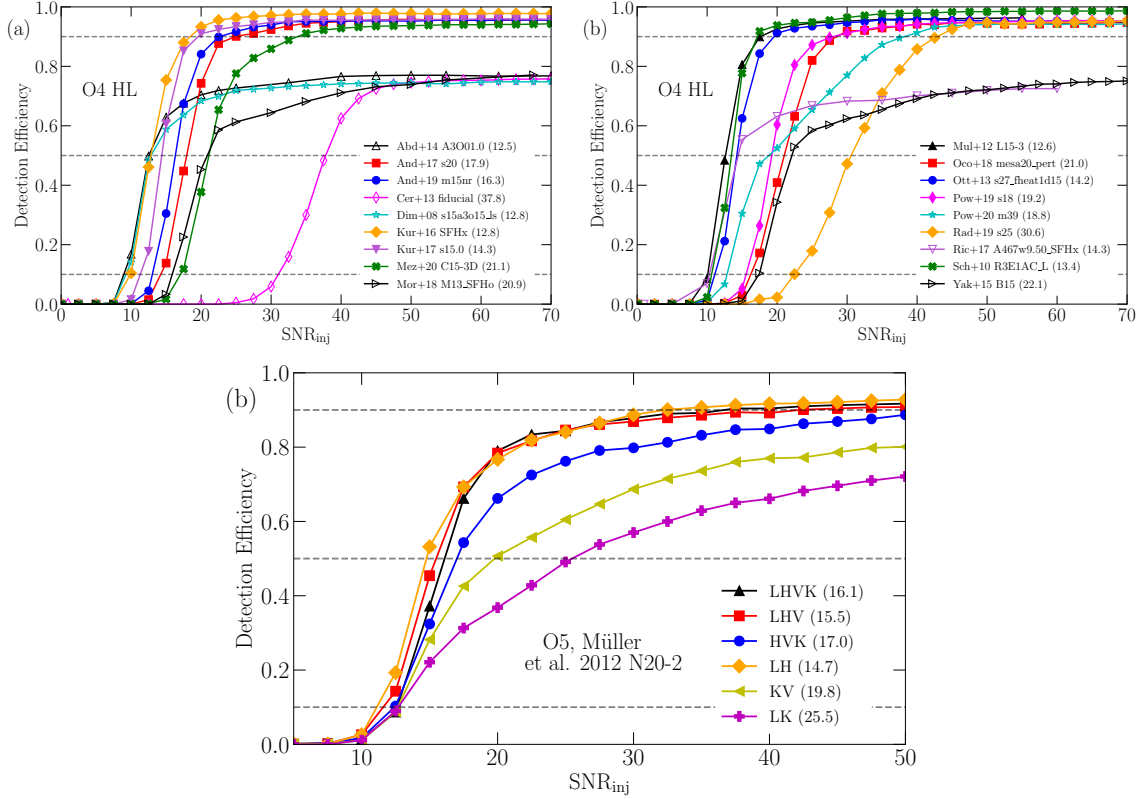


Figure 6.8. Detection efficiency curves as a function of injected SNR (SNR_{inj}) for example waveforms are presented in panels (a) and (b). Panel (c) shows the SNRs at 10%, 50% and 90% detection efficiencies. Figure is taken from Ref. [14].

relatively short and narrowband. On the contrary, the waveforms from CCSNe often have very complex signatures in time and frequency. For example, the peak frequencies of GWs from PNS oscillations evolve from around 100 Hz up to a few kHz during the first second after the collapse. The time-frequency evolution of these oscillations often is not continuous and depends on the amount of accreting matter. Moreover, rapid plumes of infalling matter can cause the generation of a broadband GW signal. Additionally, the GWs from SASI/convection and the PNS oscillations can be disconnected in the time-frequency domain.

The top panels of Figure 6.8 present detection efficiency curves as a function of injected SNR for projected O5 sensitivity and an HL network. The numbers in the brackets are the minimum detectable SNR (SNR at 50% detection efficiency). The bottom panel

of Figure 6.8 summarizes the SNR values at 10%, 50%, and 90% detection efficiency for all analyzed waveforms. The minimum detectable SNR is typically in the range of 10-25. The smallest values are reported for short waveforms (<200 ms) such as Abd+14, Dim+08, Kur+17, Ott+13, Sch+10, and Ric+17, or when they are narrowband, e.g. Mul+12. The minimum detectable SNR is increasing with the complexity of the waveform morphology and the GW signals from neutrino-driven explosions have higher minimum detectable SNR values, such as for And+16, Mor+18, Oco+18, and Rad+19. The highest minimum detectable SNR is given for the Cer+13 fiducial waveform. This signal represents a BH formation after almost 2 s with a broadband spectrum making it challenging to detect. If the star collapses to a BH faster (e.g. Cer+13 slow or [79, 205, 232, 233, 234]) then the corresponding SNR to capture the full signal is smaller. Similar to the results obtained in Section 6.4.1, the detection efficiency for linearly polarized waveforms do not exceed around 70% detection efficiency.

6.5. SUMMARY

Core-collapse supernovae are one of the most spectacular phenomena known in the Universe. CCSN explosions are multi-messenger sources and their emitted GWs are yet to be detected. Although these sources have been modeled for decades, the explosion mechanism and the details of physical processes inside an exploding star are still not fully understood. The detection of these GWs might shed light on rich stochastic dynamics. We analyzed 18 waveform families that represent an extensive set of possible signal morphologies. This wide range of models represents several emission processes, such as prompt-convection, PNS oscillations, SASI/convection, core bounce, and BH formation. The typical GW energy range is from around $10^{-10} M_{\odot}$ to $10^{-7} M_{\odot}$ and the peak frequencies range from approximately 100 Hz to 1 kHz.

It is not possible to predict robustly a GW signal emitted by a CCSN, so the search algorithm needs to use weak or minimal assumptions on the signal morphology. Then, using minimal assumptions, we used the coherent WaveBurst algorithm to make predictions on the detectability of the next nearby CCSN event. We predict that in O5, the typical detection range for neutrino-driven explosions will be around 10 kpc. For models involving rapid rotation of the progenitor stars, the detection range can get up to above 100 kpc (and possibly more if a strong turbulent GW production continues after the end of the current simulations). Our analysis of the minimum detectable SNR indicates that the GWs from CCSNe are detectable in the SNR range of roughly 10-25. The shorter waveforms are detectable with smaller SNR, while the longer and broadband signals require larger SNR to be detected. The latter are more challenging to detect, and their reconstructed SNR is usually underestimated.

As we move into an era marked by unprecedented technological advancements in GW detectors, the prospects for detecting GWs emanating from CCSN have never been more promising. Upcoming observing runs, such as LIGO's O5 and subsequent iterations, herald a new age of heightened sensitivity and observational capability. Enhanced detectors like the Einstein Telescope and Cosmic Explorer are projected to supersede current facilities like LIGO and Virgo in terms of sensitivity. These advancements are anticipated to drastically widen the scope of detectable events, potentially including CCSN occurrences in extragalactic domains. Noteworthy too are the anticipated innovations in search algorithms. Sophisticated data analysis methods, optimized through machine learning techniques or Bayesian inference models, will likely bolster our capacity to discern weaker GW signals amidst instrumental noise. These algorithmic improvements stand to enhance not only the detection rates but also the fidelity in parameter estimation for CCSN events. The acceleration of observational capabilities implies a concomitant increase in the number of detectable CCSN events. Each new observation contributes invaluable data, refining our theoretical models and enhancing our comprehension of the multifaceted mechanisms at

play during CCSN explosions. The burgeoning field of multi-messenger astronomy affords an integrated observational strategy, leveraging electromagnetic, neutrino, and gravitational wave data. This method promises comprehensive insight into CCSN phenomena, permitting cross-validation of theoretical models across disparate yet complementary data streams.

In summation, the future for detecting and understanding GWs from CCSNe is exceptionally bright. It is shaped by the confluence of advancing detector technology, the refinement of search algorithms, an increasing reservoir of observational opportunities, and the integrative capabilities afforded by multi-messenger astronomy. These factors collectively contribute to the optimistic outlook for groundbreaking discoveries in this domain.

6.6. ORIGINAL CONTRIBUTIONS

This section is based on the research carried out by myself and my colleagues and reported in the paper: “Detecting and Reconstructing Gravitational Waves from the Next Galactic Core-Collapse Supernova in the Advanced Detector Era,” published in *Physical Review D*, 104(10), 102002, 2021. My contributions included analyzing three waveform models and conducting analyses to forecast search sensitivity for the O4 and O5 observing runs.

7. THE ANGULAR POWER SPECTRUM OF GRAVITATIONAL-WAVE TRANSIENT SOURCES AS A PROBE OF THE LARGE-SCALE STRUCTURE

After the detection of the first GW signal from a BBH coalescence in 2015 [235], LIGO and Virgo captured ten BBH coalescence events and one binary neutron star coalescence in their first two observing runs. The third observation run significantly accelerated the pace of discoveries, yielding candidate events on a nearly weekly basis [236]. Most of the detections so far are from the BBH mergers, as shown in Figure 7.1. These developments have expanded the frontier of astrophysical and theoretical research, opening up a plethora of new questions and possibilities. Looking to the future, the next decade is set to bring exponential growth to GW astronomy. The O4 run is underway and it is expected to dramatically increase the number of CBC detections. Japan’s KAGRA detector [237] has recently joined the international network of ground-based GW observatories, strengthening global detection capabilities. Moreover, India has finalized its plans for the construction of the LIGO-India detector [238]. Planned advanced projects like the Cosmic Explorer [239] and Einstein’s Telescope [240] are anticipated to further increase our abilities to detect and localize GW events, promising more frequent and precise observations. Space missions like the European LISA project [241] are poised to bring GW astronomy into the realm of space. These upcoming initiatives will further consolidate the role of multi-messenger approaches—incorporating optical, particle, and GW astronomy—in providing a comprehensive understanding of the Universe. These developments also hold the potential to shed new light on the cosmic background, offering a unique window into the early universe and its large-scale structures.

In this context, an area of growing interest is the measurement of the spatial distribution of GW transient sources and its relation to the LLS of the universe [242, 243, 244]. The SDGW provides a means to test the LSS that is complementary to electromagnetic mea-

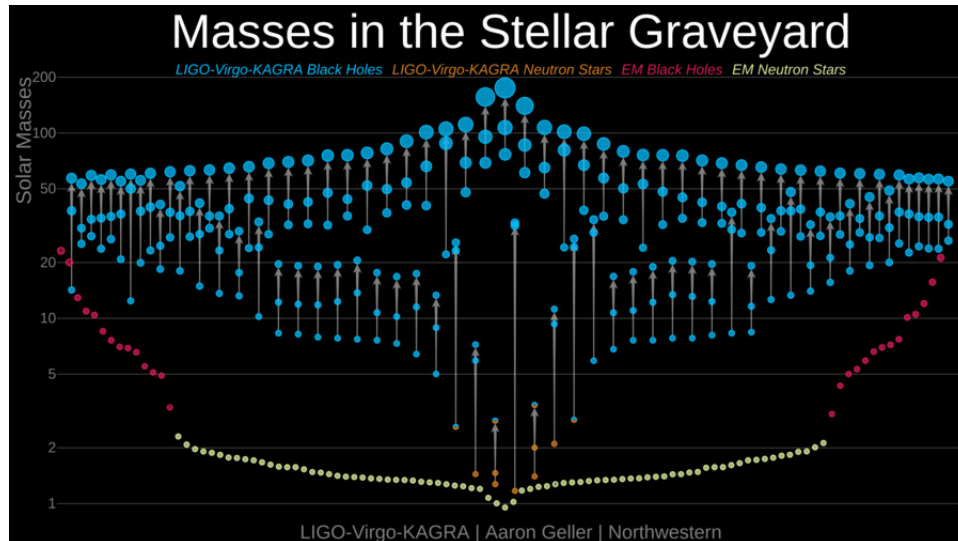


Figure 7.1. This image is a graphic of masses of announced GW detections and black holes and neutron stars previously constrained through electromagnetic observations. This version contains all events through the end of O3 with $p_{astro} > 0.5$. Figure is taken from Ref. LIGO-Virgo / Aaron Geller / Northwestern University.

measurements as well as dark siren analyses [245, 246], which rely on cross-referencing GW detections with galaxy catalogs. Developing a scheme to accurately measure the SDGW constitutes one of the critical milestones towards precision cosmology with GWs [247].

In this section, a novel, simulation-based inference method is presented to test the SDGW. This method borrows from techniques used in electromagnetic precision cosmology, in particular the study of the cosmic microwave background radiation (CMB). Specifically, in this section, we show how to calculate the observed angular power spectrum of *foreground* GW events and use it to probe the SDGW. This technique provides complementary information to analogous studies based on the astrophysical GW *background*, where the angular power spectrum is derived from the clustering statistics of the BBH host galaxies [248, 249, 250, 251, 252].

In this dissertation, only the first application of the method is presented to test the isotropic source distribution hypothesis for the confident BBH mergers observed during the O3 LVK observing run. However, it should be stressed that this approach is not limited

to this specific instance. The technique that is presented here can be easily generalized to various GW sources, future GW searches with additional detections, and different test hypotheses on the SDGW and its correlation with the LSS.

7.1. SKY LOCALIZATION OF GW EVENTS

To test the distribution of BBH mergers, it's crucial to determine the GW event sky localization. The sky localization of a GW event is defined as the most likely region in the sky from which the detected GW event emanates. The sky localization is mathematically described as a two-dimensional probability map on the celestial sphere, commonly known as a sky map. The information encoded in a sky map plays a crucial role in directing follow-up observations and enhancing our overall comprehension of the spatial distribution of cosmic sources. Once a GW event is detected, the next step is to find out where it came from. Accurate sky localization enables :

- **Multi-Messenger Astronomy:** Quick and precise localization allows for follow-up observations using electromagnetic telescopes, which can observe the event in different wavelengths, providing a fuller understanding of the physical properties of the GW source.
- **Astrophysical Understanding:** Knowing the location can help in understanding the environment in which such events occur, thus enriching astrophysical models.
- **Cosmological Insights:** Accurate localization can also be vital for cosmological measurements, like determining the Hubble constant through the use of 'standard sirens.'

Skymaps are generally formulated as probability density functions mapped onto the celestial sphere. The higher the density in a particular region, the more likely the GW source is in that direction in the sky. Often, these probability maps are presented with contour lines that indicate regions enclosing a certain percentage of the total probability. For example, a 90% confidence region would include the area where the source is 90% likely to be located.

The geometry and orientation of detectors significantly influence the resolution of sky localization. For instance, detectors like LIGO and Virgo are not equally sensitive in all directions. This anisotropic sensitivity, captured by the detectors' antenna patterns as shown in Equ. 2.14, plays a significant role in shaping the sky map. Other than that, the time delays between the arrival of a GW at different sites are crucial for localization in a network of detectors. These time delays can be used to triangulate the source's position. However, it's worth noting that GW usually provides only two-time delays (from three detectors), which localizes the source in the sky. SNR, phase, or polarization angle of the signal are needed to further narrow down the location.

Several computational techniques are employed to construct sky maps from raw detector data. Algorithms sift through the noisy signals to extract valuable information that eventually can be used to construct a sky localization map. There are usually two ways widely used to get the skymaps: BAYESTAR [16] is a rapid, Bayesian, non-Markov chain Monte Carlo sky localization algorithm. It takes the information from matched-filter pipelines as input and produces probability sky maps in a few seconds. Another way is using Bayesian inference techniques [253]. This technique is very computationally costly so it is typically used for more detailed parameter estimation. It calculates the posterior distributions of the parameters of interest, given the data and a statistical model. In the following, we are going to briefly describe the main features of the two methods.

7.1.1. BAYESTAR. BAYESTAR [16] presents a transformative approach to the rapid and accurate sky localization of GW events using Bayesian methodologies. Remarkably, BAYESTAR requires only a few seconds to yield sky localization estimates that are

comparable in accuracy to those achieved through extensive Markov Chain Monte Carlo (MCMC) analyses. In GW searches, matched-filter pipelines produce signal information that can be used for sky localization. The values of arrival times, amplitudes, and phases produced from the pipelines are given in the form of measurements with known and quantifiable uncertainties. These uncertainties are translated into a likelihood function, suitable for Bayesian inference. BAYESTAR employs the Fisher Information Matrix as an important tool for validating the form of the likelihood function, providing key insights. On the computational side, BAYESTAR avoids the computational complexities and parallelization issues inherent with a full MCMC by utilizing a straightforward likelihood function and a well-defined parameter space. It opts for deterministic, very low-order Gaussian quadrature for Bayesian marginalization. Lastly, BAYESTAR can be extended to work not only with the results generated by the matched-filter detection pipeline but also directly on the full GW time series. This makes it a fast and coherent localization method that is mathematically equivalent to a full MCMC parameter estimation, albeit focused on extrinsic parameters such as sky location, binary orientation, and distance.

7.1.2. Bilby. Bilby [253, 254] is another software package used extensively in the GW data analysis community. It is a flexible toolkit for Bayesian model selection and parameter estimation, and it is often used for interpreting the signals detected by LIGO, Virgo, and other GW observatories. The primary objective of the GW inference for compact binary merger signals is to recover posterior probability densities for the source parameters θ , like the masses and spins of the binary components, given the data and a model hypothesis. The posterior can be computed using Bayes' theorem:

$$p(\theta | d, \mathcal{H}) = \frac{\mathcal{L}(d | \theta, \mathcal{H})\pi(\theta | \mathcal{H})}{\mathcal{Z}(d | \mathcal{H})}. \quad (7.1)$$

where $\mathcal{L}(d | \theta, \mathcal{H})$ is the likelihood, $\pi(\theta | \mathcal{H})$ is the prior, $\mathcal{Z}(d | \mathcal{H})$ is the evidence, and \mathcal{H} is the model. The prior is chosen to incorporate any a priori knowledge about the parameters. The likelihood represents the probability of the detectors measuring data d , assuming a signal (described by the model hypothesis \mathcal{H}) with source properties θ . Stochastically sampling the posterior probability distribution with MCMC and nested sampling [253].

Default BBH priors contain 15 parameters. The intrinsic variables are the two black hole masses $m_{1,2}$, their dimensionless spin magnitudes $a_{1,2}$, the tilt angle between their spins and the orbital angular momentum $\theta_{1,2}$, and the two spin vectors describing the azimuthal angle separating the spin vectors δ_ϕ and the cone of precession about the system's angular momentum ϕ_{JL} . The extrinsic parameters are the luminosity distance d_L , the right ascension RA and declination DEC , the inclination angle between the observer's line of sight and the orbital angular momentum ι , the polarization angle ϕ , and the phase at coalescence ϕ_c . The phase spins, and inclination angles are all defined at some reference frequency. No default prior for the coalescence time t_c [255] is set. With the posterior distribution of sky location, more accurate skymaps can be generated.

7.2. ANGULAR POWER SPECTRUM

The angular power spectrum is a tool used in astrophysics and cosmology to quantify the distribution of power or variance of a physical quantity over different angular scales in the sky [256]. Essentially, it describes how the fluctuations in a field (such as the temperature of the cosmic microwave background radiation, or the density of galaxies) vary as a function of angular size. The concept is commonly applied to the analysis of CMB radiation, where it provides insights into the initial conditions and composition of the universe. In the case of the CMB, the angular power spectrum reveals the intensity of temperature fluctuations at various angular scales, providing observational evidence for the theories about the Big Bang, cosmic inflation, and the large-scale structure of the universe [248, 249, 250, 251, 252].

The angular power spectrum is often represented by the quantities of C_l where l (often called the ‘‘multipole moment’’) is related to the angular scale. In cosmology, the angular power spectrum is not limited to CMB studies; it is also used in the analysis of galaxy surveys [257], gravitational lensing [258].

To compute the C_l of the BBH population, we treat the sky localization error regions of the BBH detections as probability density heat maps, following Ref. [259]. Given the (normalized) sky localization error region map of the i^{th} BBH detection in the sample, $M_i(\chi, \phi)$, where χ and ϕ are the polar and azimuthal angles on the celestial sphere, respectively, we define the sky localization probability:

$$M(\chi, \phi) = \frac{1}{A(N)} \sum_{i=1}^N F_i(\chi, \phi) M_i(\chi, \phi). \quad (7.2)$$

where N is the number of BBH detections, F_i are probability weights that depend on the GW detector network sensitivity, and $A(N)$ is a normalization factor. By expanding the sky localization map in spherical harmonics:

$$M(\chi, \phi) = \sum_{lm} \alpha_{lm} Y_{lm}(\chi, \phi). \quad (7.3)$$

The multipole components of the angular power spectrum are obtained by summing the absolute square of the α_{lm} coefficients of the expansion over m :

$$C_l = \frac{1}{2l+1} \sum_m |\alpha_{lm}|^2. \quad (7.4)$$

7.3. TWO-DIMENSIONAL CORRELATION FUNCTION

The physical information contained in the power spectrum can also be expressed in terms of the two-dimensional (angular) correlation function (CF). The CF describes the excess probability of finding two objects in the directions \hat{n}_1 and \hat{n}_2 and angular separation θ

with respect to a uniform distribution. Given the cumulative sky localization map $M(\chi, \phi)$, the CF is defined as

$$C(\theta) = \langle M(\hat{n}_1) \cdot M(\hat{n}_2) \rangle_{21} . \quad (7.5)$$

where the average is taken over the observed sky with angular separation held fixed [259]. The CF can be written in terms of the power spectrum as

$$C(\theta) = \frac{1}{4\pi} \sum_l (1 + 2l) C_l P_l(\cos \theta) . \quad (7.6)$$

where $P_l(\cos \theta)$ denotes the Legendre polynomial of order l and argument $\cos \theta$. Typically, the finite beam resolution of the detectors leads to a high- l cutoff l_{\max} in Eq.(7.6). This effect can be modeled by introducing a window function $W_l \propto \exp[-l(l+1)\sigma_{\text{res}}^2]$, where σ_{res} is the detector resolution [260].

7.4. METHOD

The method probes the spatial distribution of BBH merger events by computing their observed angular power spectrum [259] and comparing it to a fiducial distribution. In this work, the isotropic distribution is selected, which corresponds to testing whether BBHs are isotropically distributed in the local universe. First, the power spectrum of observed BBH events from the LVK GW catalogs is computed. Then a suitable subset of these events is chosen by imposing the selection cuts detailed in the next section. Then, the power spectra of a number of mock sets obtained by injecting synthetic signals into real detector data are computed. Their parameters are sampled from the latest LVK population analysis posterior distributions [15] and inject the signals isotropically into the sky. Then a subset of events is selected by imposing the same selection cuts used for the observed BBH mergers. The synthetic power spectra are combined to produce a fiducial distribution of an isotropically distributed angular power spectrum as would be measured by the LVK detectors. Finally, there are statistical consistency tests of the observed BBH angular distribution with the

Table 7.1. List of selected GW events

GW190408_181802	GW190412_053044	GW190413_052954
GW190413_134308	GW190503_185404	GW190512_180714
GW190512_180714	GW190513_205428	GW190517_055101
GW190519_153544	GW190521_030229	GW190602_175927
GW190701_203306	GW190706_222641	GW190720_000836
GW190727_060333	GW190728_064510	GW190803_022701
GW190828_063405	GW190828_065509	GW190915_235702
GW190924_021846	GW190929_012149	GW191105_143521
GW191127_050227	GW191215_223052	GW191230_180458
GW200129_065458	GW200202_154313	GW200208_130117
GW200209_085452	GW200219_094415	GW200224_222234
GW200311_115853		

fiducial isotropic distribution are performed. For each multipole component of the power spectrum, the p-value that the observed multipole belongs to the fiducial distribution is computed.

7.4.1. GW Events Selection. In this work, only the subset of BBH events detected during the LVK O3 observing run with a false alarm rate (FAR) smaller than 1 yr^{-1} is considered, as reported in Ref. [15]. The sample is further restricted to three-detector events. This allows to generation of a consistent fiducial angular distribution, as the accuracy of sky localizations depends on the number of detectors [16]. These conditions restrict the sample of O3 events to 34. These events constitute our catalog of observed signals. A list of these events is reported in Table 7.1.

7.4.2. Synthetic Events Generation. To generate the synthetic signals, their source parameters are drawn from their inferred median population distributions [15], assuming the Power Law + Peak model (PP) for the primary mass [261] with a power law on mass ratio, the Default spin model [262, 263], and a power law model for redshift evolution [264]. Figure 7.2 shows the distribution of these source parameters.

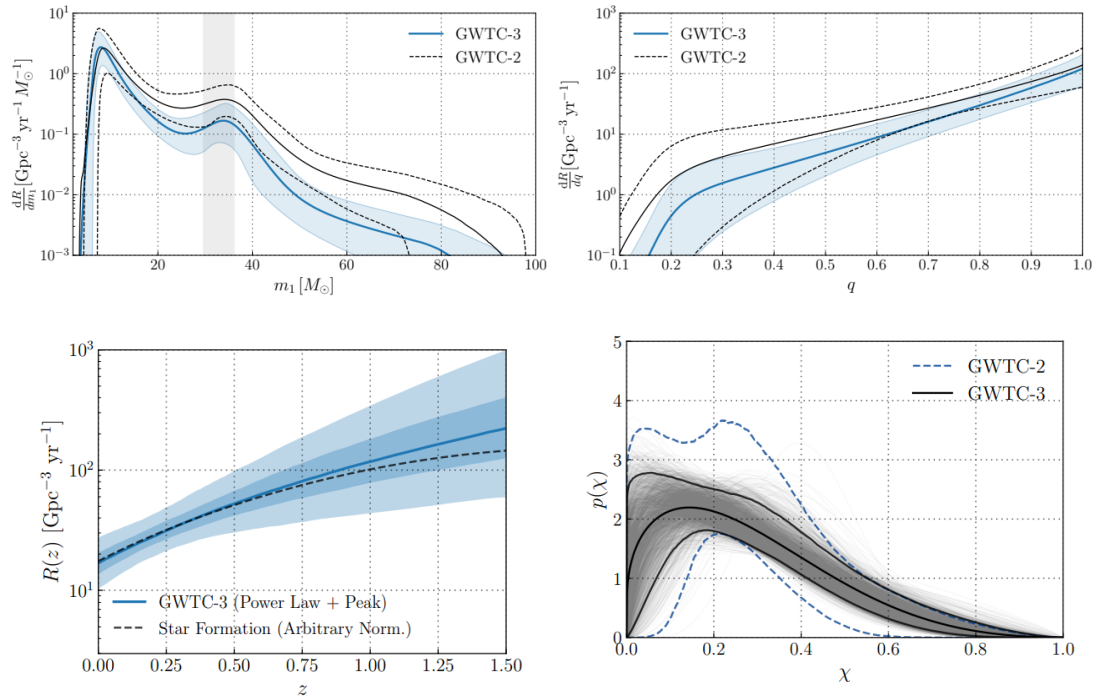


Figure 7.2. The astrophysical BBH primary mass (top left panel) and mass ratio (top right panel) distributions for the fiducial texttPP model, showing the differential merger rate as a function of primary mass or mass ratio. The bottom left panel shows the distributions of component spin magnitudes. The bottom right panel shows the constraints on the evolution of the BBH merger rate. Figure is taken from Ref. [15]

The phase and orientation parameters are sampled from distributions with isotropic orientations. The signals are injected into real detector data with an isotropic distribution in the sky. The times of the injections are uniformly sampled during O3. These times are downselected to periods that do not overlap with known non-astrophysical transient noise [265] and GWTC-3 confident detections [236]. The signals are simulated with the IMRPhenomPv2 [266, 267] waveform model. Selecting the synthetic events based on their FAR is computationally expensive, as it requires doing PE for the full set of events. To avoid this computational cost, the FAR selection cut is substituted with a threshold on the optimal network SNR ρ_N . Here choose $\rho_N > 10$, following the approximate threshold used for the semianalytic sensitivity estimates in Ref. [15].

Here a catalog of 3,400 synthetic events is generated. This allows us to produce meaningful statistical results while limiting the computational cost required to perform PE and generate the sky localization maps. We use the synthetic signals to create 100 random mock sets of 34 events each. These sets provide independent realizations of what the detectors would observe under the hypothesis that the events are isotropically distributed in the sky. These sets are used to generate the fiducial distribution.

Then PE of all observed and synthetic events is performed with `bilby pipe` [253]. The `IMRPhenomPv2` waveform is used for the signal model and the samples are drawn from the posterior distribution with the nested sampler `dynesty` [268].

The standard LVK uniform priors on the mass ratio and chirp mass from Ref. [236] are adopted. The chirp mass is restricted to a $\pm 12M_{\odot}$ range around the injected values of the synthetic events and the median values of the O3 observed events. Additionally, the priors are constrained on the primary and secondary masses to be within the interval $[1, 120] M_{\odot}$. The prior on all other parameters is chosen according to the uninformative priors adopted in standard LVK analyses [236]. Then the posterior samples are used for the declination and the right ascension to produce sky maps.

7.4.3. Angular Resolution. The diffraction-limited angular resolution of the LIGO-Virgo network determines the high- l cutoff as $l_{\max} \sim \pi/\theta_{\text{res}}$, where θ_{res} is the angular resolution. In this work, l_{\max} is estimated directly from the distributions of the skymaps. The distribution of the observed skymap 90% contour regions is fit as a proxy for the square angular resolution $\Delta\Omega_{\text{res}} = 2\pi[1 - \cos(\theta_{\text{res}}/2)]$ with a gamma distribution [269]. We then perform a one-tailed test and choose $\Delta\Omega_{\text{res}}$ such that 90% of the observed events have a larger localization area than that value. This provides an estimate for the angular resolution of $\theta_{\text{res,o}} \sim 7^{\circ}$, corresponding to $l_{\max,\text{o}} \sim 26$. We then repeat the procedure for the whole set of synthetic events. This yields $\theta_{\text{res,s}} \sim 5^{\circ}$, corresponding to $l_{\max,\text{s}} \sim 37$. Figure 7.4

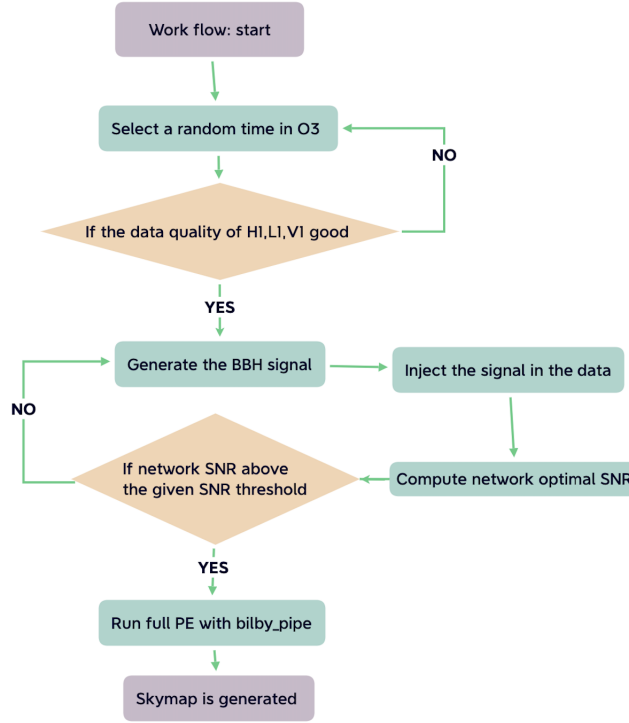


Figure 7.3. Flowchart of the pipeline used for the generation of the synthetic data sets that are used for the comparison with the observed power spectrum.

shows the distribution of skymap 90% contour regions. The resolution of the simulated set is smaller than the resolution of the observed set. This is expected because of the larger number of events in the simulated set compared to the observations.

As a consistency check, we also estimate $\Delta\Omega_{\text{res}}$ using the theoretical estimate of Ref. [270]. For a monochromatic GW at frequency f , the square angular resolution of a three-detector network is

$$\Delta\Omega_{\text{res}} \approx 8 \left(\frac{150\text{Hz}}{f} \frac{10}{\rho_{\text{N}}} \right)^2 \frac{10^{17}\text{cm}^2}{A_{\text{N}}} \frac{1/27}{\rho_1^2 \rho_2^2 \rho_3^2 / \rho_{\text{N}}^6} \frac{\sqrt{2}/2}{|\sin i_{\text{N}}|}. \quad (7.7)$$

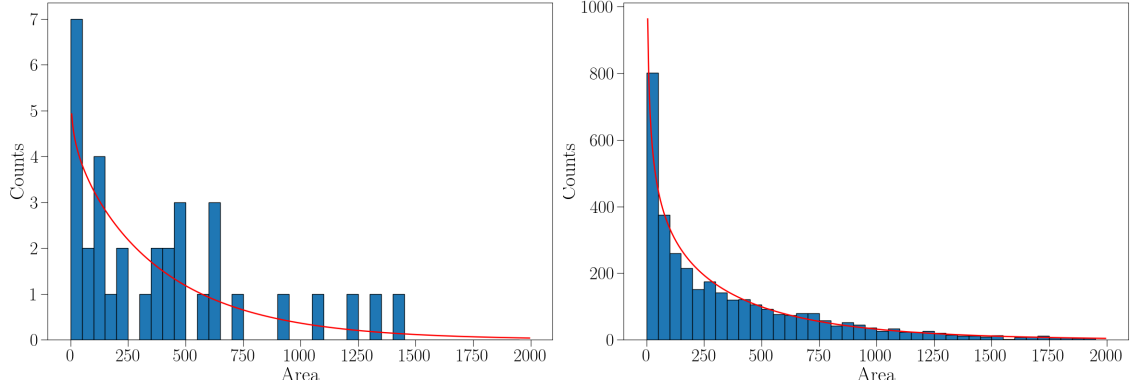


Figure 7.4. The distribution of sky localization area at 90% contour lever from the observed events (left) and synthetic events (right). The red curve shows the gamma distribution by fitting the sky localization area.

where A_N is the triangular area formed by the three detector sites, i_N is the angle between the wave direction and the three-detector plane, ρ_N is the network optimal SNR of the GW signal, and ρ_i ($i = 1, 2, 3$) are the single-detector SNRs. We consider a triangular area $A_N = 10^{17} \text{cm}^2$ for the LIGO-Virgo network and a mean incidence angle of 45° with the detector plane. We use the posterior sample median values to estimate the SNRs and approximate f with the ISCO frequency obtained from the posterior median chirp mass and mass ratio. Using the means of the SNRs and f in Eq. (7.7), we obtain the angular resolution $\theta_{\text{res,o}} \sim 4.04^\circ$ for the observed events and $\theta_{\text{res,s}} \sim 4.44^\circ$ for the synthetic events, corresponding to $l_{\text{max,o}} \sim 45$ and $l_{\text{max,s}} \sim 41$, respectively. The theoretical estimate gives higher bounds than the data sets. This is expected, as Eq. (7.7) is derived under optimal assumptions and a Fisher approximation. In the following, we will use $l_{\text{max}} = 26$ as a conservative upper bound.

7.5. RESULT

We generate the combined sky localization map of the observed GW events, $M(\chi, \phi)$, by stacking the sky localization density maps of all events in the observed catalog. Figure 7.5 shows the Mollweide representation of $M(\chi, \phi)$.

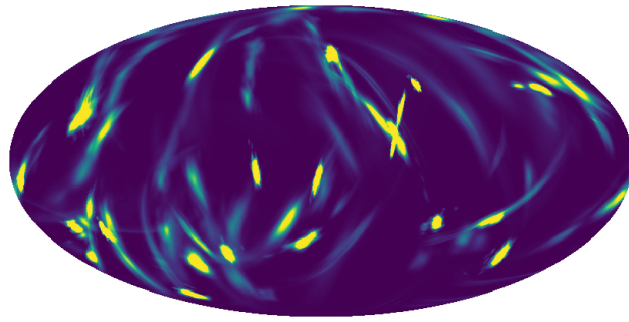


Figure 7.5. Combined sky localization map of the O3 BBH events considered in the analysis. The sky localization of each event is generated with BAYESTAR [16] from the PE posterior samples for the declination and the right ascension. The map is created with the HEALPY package [17, 18]. Figure is taken from Ref. [19].

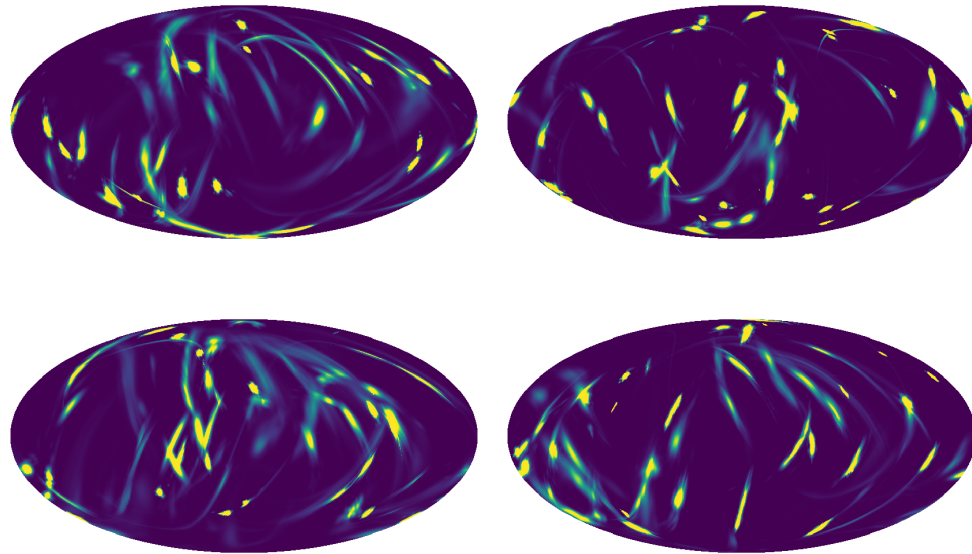


Figure 7.6. Combined sky localization maps from four synthetic sets. Each set contains 34 synthetic events.

We repeat this procedure to obtain a cumulative sky localization map for each set of synthetic events. Figure 7.6 shows combined skymaps from 4 sets of synthetic events, each made from 34 events. For the 100 sets of synthetic events, Figure 7.7 shows the combined

sky localization map obtained by stacking the 100 synthetic maps. The map shows that the synthetic events are isotropically distributed in the sky. It also depicts what the GW sky would look like with 3400 foreground BBH events, a not-too-unrealistic scenario in a few years.

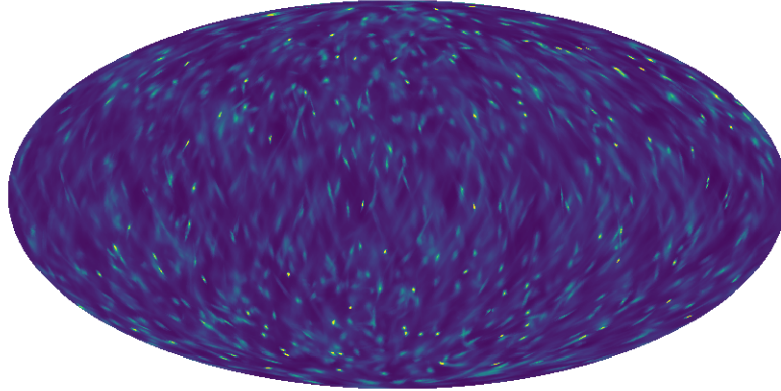


Figure 7.7. Combined sky localization map of all 3400 synthetic events that are used to build the fiducial power spectrum. Their isotropic distribution in the sky is shown by the map. Figure is taken from Ref. [19].

7.5.1. Angular Power Spectrum. We then compute the angular power spectra of the combined sky localization maps. The left panel in Figure 7.8 shows the angular power spectra computed from the combined skymaps from observed events and synthetic events. The blue curve indicates the C_l from the observed events, while the other colored curves indicate the 100 sets of synthetic events.

Figure 7.9 shows the power spectrum of the observed events (red curve) and the mean spectrum of the 100 synthetic sets (black curve) up to $l_{\max} = 26$. For each l , we fit the C_l distribution from the synthetic sets with a gamma distribution. The three gray-filled areas in Figure 7.8 (darker to lighter gray) denote the 1σ to 3σ confidence level regions from

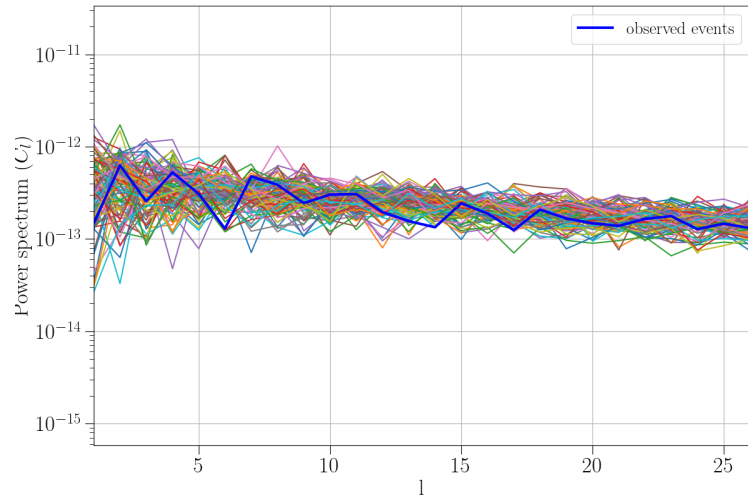


Figure 7.8. The plot shows the observed power spectrum of O3 BBH events (blue curve) considered in the analysis and 100 sets of synthetic events (other colors) under the isotropic hypothesis.

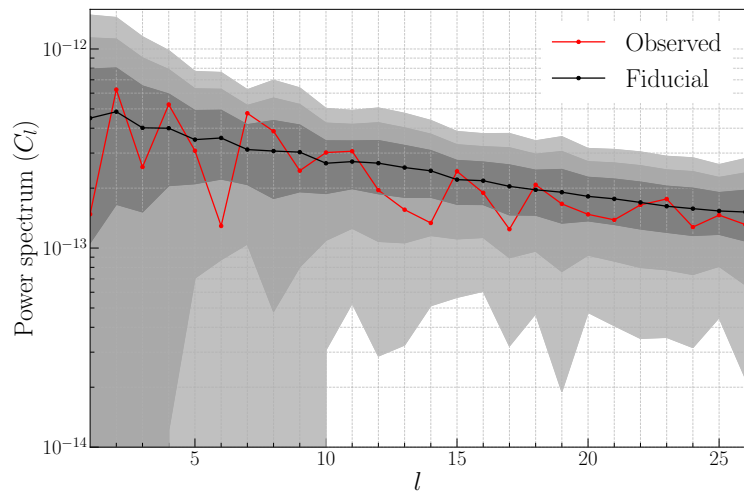


Figure 7.9. The plot shows the observed power spectrum of the O3 BBH events (red curve) and the fiducial power spectrum obtained from the 100 synthetic sets under the isotropic hypothesis (black curve). The gray-filled regions denote $1 - 3\sigma$ deviations from the mean. Figure is taken from Ref. [19].

the mean. All observed C_l values lie within the 2σ band. Therefore, we conclude that the observed angular distribution of observed BBH events shows no significant inconsistencies relative to an isotropic distribution.

To quantify this statement, we performed two statistical tests: the χ^2 test and the cumulative distribution of p-values. χ^2 test is a statistical test used to determine if there is a significant association between two categories of variables in a sample [271]. Here we assess the goodness of fit of the observed power spectrum with the fiducial spectrum by performing a reduced χ^2 test:

$$\chi^2 = \sum_l \frac{(C_l(\text{observed}) - C_l(\text{synthetic}))^2}{\sigma_l^2}. \quad (7.8)$$

Here σ_l is the variance of the gamma distribution for each l . With the χ^2 test, we can compute the p-value. The p-value, or probability value, is a concept in statistics that measures the strength of the evidence against a null hypothesis [269]. It quantifies the probability of observing a statistic as extreme as, or more extreme than, the observed statistic under the assumption that the null hypothesis is true. In our case, the χ^2 test yields a p-value of 0.82, in agreement with the null isotropic hypothesis.

In the second test, the cumulative distributions of p-values for the observed C_l under the hypothesis that the BBH is distributed isotropically in the sky are computed. For each l we have 100 independent values of C_l computing from 100 synthetic sets. We fit these C_l sets at fixed l with a gamma distribution. Then we compute the p-value of the observed C_l . Figure 7.10 shows as an example the distribution of one of the C_l for the 100 synthetic sets ($l = 14$). The black dashed line indicates the C_l from the 34 events in our observed set. The red curve is the gamma distribution fit. For this specific value of $l = 14$, the p-value is 0.011.

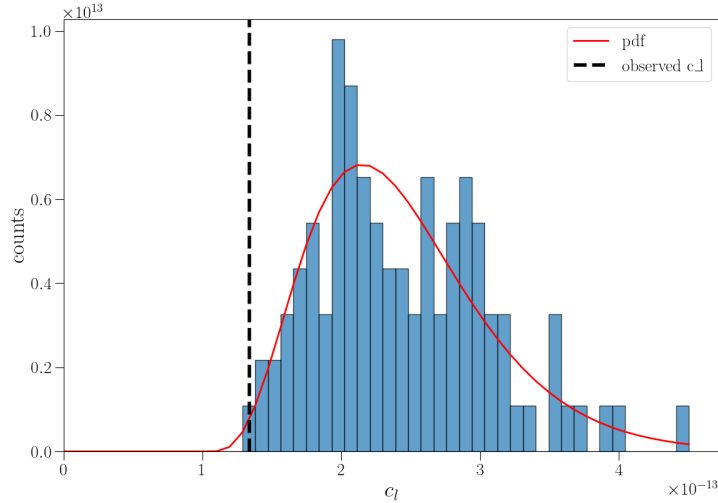


Figure 7.10. An example distribution from one of the C_l for the 100 synthetic sets ($l = 14$).

Then we compute the p-value for all $l = 1, 2, \dots, 26$ and plot the cumulative distributions of these 26 p-values (pp-plot). Figure 7.11 shows the cumulative distributions of p-values (red dots). The expected distribution is represented by the black dashed line, with the gray-filled regions denoting the $1 - 3\sigma$ confidence levels. All p-values lie within the 2σ region, in agreement with the results of Figure 7.8.

7.5.2. Two-dimension Correlation Function. Finally, we test the isotropy hypothesis with the CF. Figure 7.12 and Figure 7.13 show the CF for the observed set and the fiducial correlation function obtained from the 100 synthetic sets under the isotropic hypothesis. We have set the window function

$$W_l \propto \exp[-l(l+1)\sigma^2] . \quad (7.9)$$

where the detector resolution is $\sigma_{\text{res}} = l_{\text{max}}$.

Similarly to C_l , we compute the cumulative distribution of the p-value of CF for the separation angle of θ . All p-values lie within the 2σ region, in agreement with the results of the angular power spectrum.

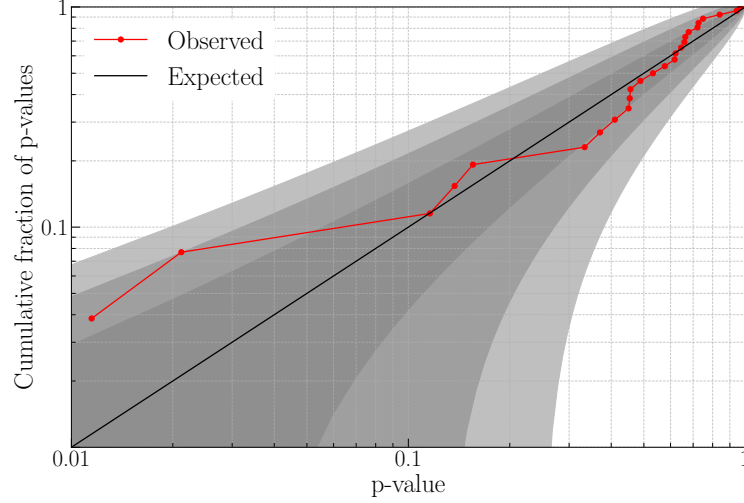


Figure 7.11. The cumulative distribution of observed p-values for the C_l . The black solid line indicates the expected distribution under the isotropic hypothesis. The gray-filled regions correspond to $1 - 3\sigma$ deviations from the expected distribution. Figure is taken from Ref. [19].

Figure 7.15 shows the CF computed from the observed and 100 synthetic sets. Consistent with the power spectrum result, the observed CF agrees with the fiducial isotropic distribution within 2σ .

The CF in Equation 7.6 can be interpreted as a weighted projection of the spatial two-point CF $\xi(r)$ [272]. At small scales, the power-law behavior of the CF is expected to be

$$C(\theta) = (\theta/\theta_0)^{1-\gamma}. \quad (7.10)$$

where θ_0 is an angular correlation scale [273] and γ is the power-law slope of the spatial two-point CF:

$$\xi(r) = \left(\frac{r}{r_0}\right)^{-\gamma}. \quad (7.11)$$

where r_0 is the spatial correlation length. The power law slope of CF provides a test of isotropy [259]. We first compute the power-law slope γ of each synthetic CF at the minimum angular resolution $\theta_{\text{res},s}$ with a log-log fit. The slope distribution from 100 synthetic sets can be seen in Figure 7.15. Averaging the values, we obtain a fiducial value of $\gamma_s = 2.05 \pm 0.35$,

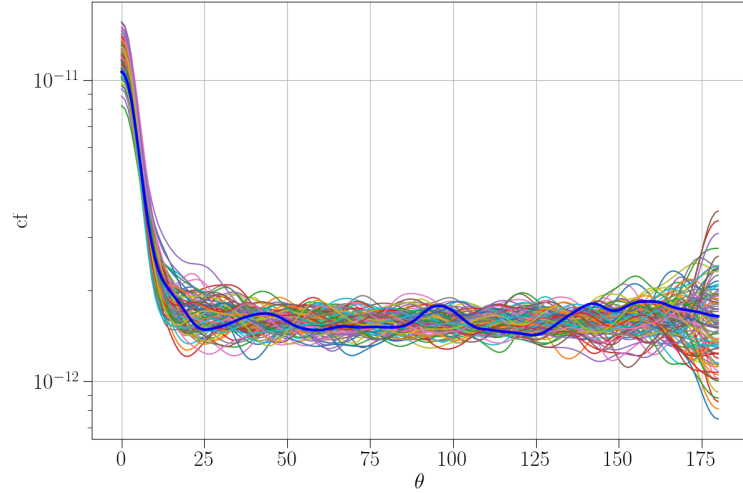


Figure 7.12. The observed correlation function of the O3 BBH events (blue curve) and the 100 set of synthetic events (other colors).

which is consistent with an isotropic distribution ($\gamma = 2$). We then compute the power-law slope for the observed set at the same angular scale. The observed power-slope is $\gamma_o = 1.96$. This is in agreement with the null isotropic hypothesis with a p-value of 0.45.

7.6. CONCLUSIONS

In this section, we have developed a new, simulation-based inference framework to probe the spatial distribution of observed, foreground GW events. Our approach compares the power spectrum of observed GW signals to a fiducial power spectrum from a theoretical distribution. As an application of this method, we tested the isotropy hypothesis of the 3 detector BBH events with $FAR < 1/year$ observed during the O3 LVK observing run. No evidence of anisotropy at the 2σ confidence level is found.

Our method provides a powerful framework for testing the universe's LSS that complements current GW background searches [274, 275]. Due to the phase-coherence of matched-filter searches employed in GWTC-3 [236], we are able to access higher multipole moments than background searches [276]. Relying on resolved sources allows us to achieve

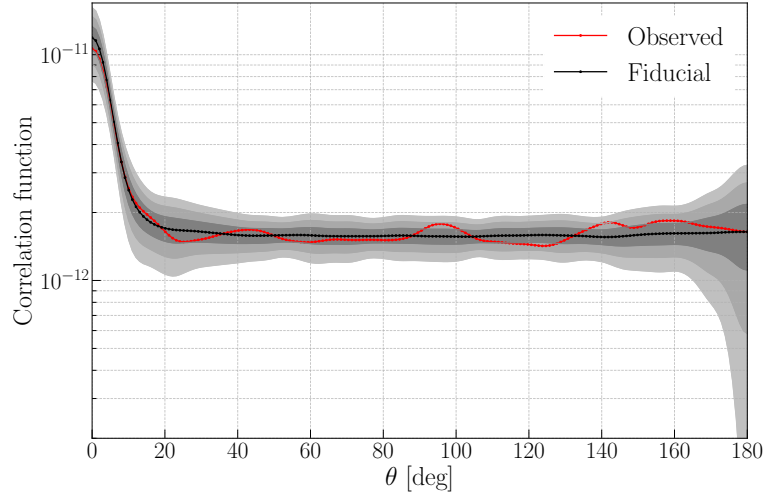


Figure 7.13. The observed correlation function of the O3 BBH events (red curve) and the fiducial correlation function under the isotropic hypothesis (black curve). The gray-filled regions denote $1 - 3\sigma$ deviations from the mean. Figure is taken from Ref.[19].

astrometric resolution at the square degree level [247]. Although the two approaches essentially target the same signal in the limit of many detections, our method has a higher resolution and is more sensitive than background analyses.

A first, straightforward extension of this work would be to refine the test of BBH isotropy as more GW events are discovered. Particularly, third-generation GW detectors are expected to detect GW with a sensitivity surpassing that of LIGO and Virgo. Given the existing local rate estimates for BBH mergers, the overall BBH merger rate is expected to be approximately 10,000 per month [277]. This offers a bright prospect for examining the isotropic distribution of BBH events.

Tests of specific theoretical models of anisotropic distributions and cross-correlations with astrophysical populations in the EM domain are two additional applications. The approach in this section can also be directly extended to include information about the source distances. Statistical associations between the observed GW populations and other extragalactic populations may be within reach of current and next-generation GW detectors. This method will provide a means to rapidly detect and quantify any such associations.

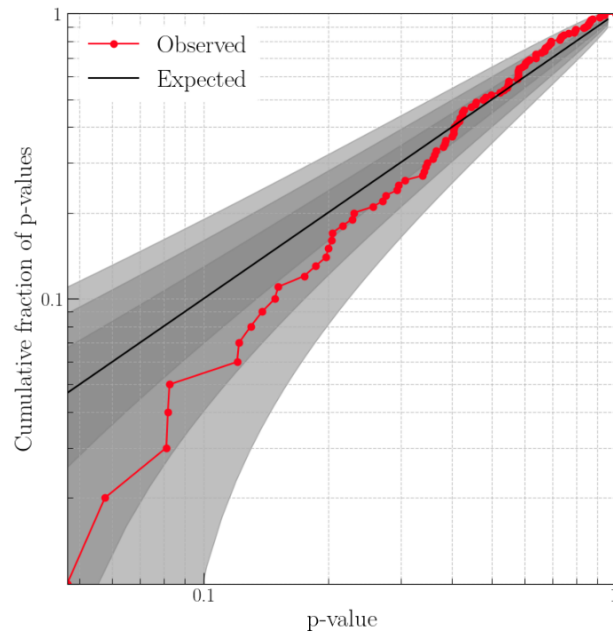


Figure 7.14. The cumulative distribution of observed p-values for the CF. The black solid line indicates the expected distribution under the isotropic hypothesis. The gray-filled regions correspond to $1 - 3\sigma$ deviations from the expected distribution.

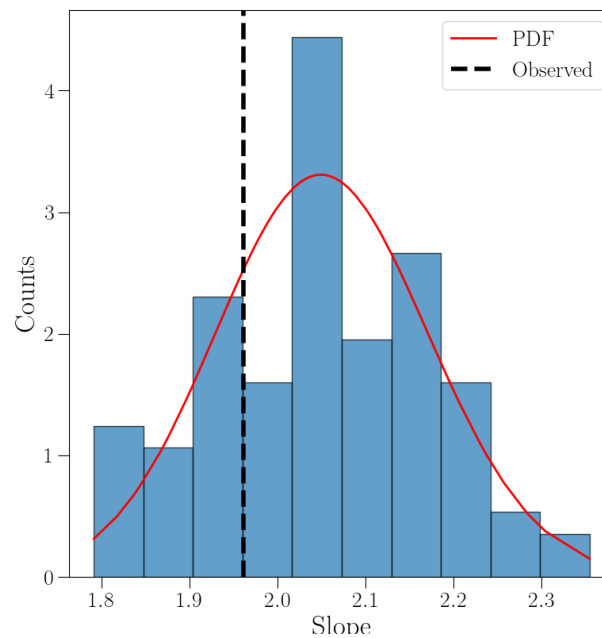


Figure 7.15. The distribution of the CF slope at minimum angular resolution $\theta_{\text{res},s}$ for 100 synthetic sets. The red curve is a gamma distribution to fit. The black dashed line indicates the slope computed from the observed events.

7.7. ORIGINAL CONTRIBUTION

This section is based on the paper co-authored by Y. Zheng *et al*, titled “The Angular Power Spectrum of Gravitational-Wave Transient Sources as a Probe of the Large-Scale Structure,” that was published in *Physical Review Letters*, 131, 171403 (2023).

My contribution involves developing the pipeline for synthetic events, generating skymaps, and the analysis for testing isotropic distributions of BBH mergers.

8. CONCLUSIONS

This dissertation addresses the realm of GW sources beyond the well-studied CBC. Starting with CCSNe, an extensive search was conducted using the O3 data from the LIGO and Virgo detectors. While no GW signals were identified, the study succeeded in placing important upper limits on key parameters related to CCSN phenomena, such as GW energy, luminosity, and PNS ellipticity. These new constraints enhance our understanding of the complex physical processes that drive these stellar explosions and have clear implications for future studies aimed at elucidating the mechanisms of GW emission from CCSNe. In terms of technological advancements, the study also explored the prospective sensitivity of current and future observing runs. It gives the detection range and minimum detectable SNR for different SN waveforms in O4 and O5.

Additionally, a novel, simulation-based inference framework was introduced, aimed at understanding the spatial distribution of gravitational wave events. Applying this method to BBH mergers yielded no evidence for anisotropy at a 2σ confidence level, thereby adding a new layer to our understanding of the universe's large-scale structure. This approach promises to be versatile, offering higher resolution and sensitivity compared to existing methods and having potential applicability to other extragalactic phenomena.

As more data accumulate from ongoing and subsequent observational runs, the methodologies and insights offered in this dissertation will become increasingly valuable. Not only do they stand to improve our understanding of new GW sources like CCSNe but they also promise to enrich our broader understanding of LSS in the universe. In summary, the methods and results presented in this dissertation serve as foundational elements for future work in this quickly evolving field, aligning closely with its central theme of advancing our understanding of GW sources that extend beyond the scope of CBC.

REFERENCES

- [1] Nigel T. Bishop and Luciano Rezzolla. Extraction of Gravitational Waves in Numerical Relativity. *Living Rev. Rel.*, 19:2, 2016. doi: 10.1007/s41114-016-0001-9.
- [2] R. Abbott, B. Abbott, Thomas Abbott, Matthew Abernathy, Fausto Acernese, K. Ackley, C. Adams, Teneisha Adams, Paolo Addesso, R.X Adhikari, Vaishali Adya, C. Affeldt, M. Agathos, Kazuhiro Agatsuma, Nishu Aggarwal, Odylio Aguiar, L. Aiello, Anirban Ain, P. Ajith, and John Zweizig. Observation of gravitational waves from a binary black hole merger. *Physical Review Letters*, 116, 02 2016. doi: 10.1103/PhysRevLett.116.061102.
- [3] Bernard F. Schutz. Networks of gravitational wave detectors and three figures of merit. *Class. Quant. Grav.*, 28:125023, 2011. doi: 10.1088/0264-9381/28/12/125023.
- [4] R. Abbott et al. GWTC-3: Compact Binary Coalescences Observed by LIGO and Virgo During the Second Part of the Third Observing Run. 11 2021.
- [5] Benjamin P. Abbott et al. Sensitivity of the Advanced LIGO detectors at the beginning of gravitational wave astronomy. *Phys. Rev. D*, 93(11):112004, 2016. doi: 10.1103/PhysRevD.93.112004. [Addendum: Phys.Rev.D 97, 059901 (2018)].
- [6] J Glanzer, S Banagiri, S Coughlin, M Zevin, C Berry, O Patane, Sara Bahaadini, Neda Rohani, K Crowston, V Kalogera, C Østerlund, L Trouille, and A Katsaggelos. Data quality up to the third observing run of advanced ligo: Gravity spy glitch classifications. *Classical and Quantum Gravity*, 40, 02 2023. doi: 10.1088/1361-6382/acb633.
- [7] B. P. Abbott et al. Observation of Gravitational Waves from a Binary Black Hole Merger. *Phys. Rev. Lett.*, 116(6):061102, 2016. doi: 10.1103/PhysRevLett.116.061102.
- [8] Anthony Mezzacappa et al. Gravitational-wave signal of a core-collapse supernova explosion of a $15 M_{\odot}$ star. *Phys. Rev. D*, 102(2):023027, 2020. doi: 10.1103/PhysRevD.102.023027.
- [9] Takami Kuroda, Kei Kotake, and Tomoya Takiwaki. A new Gravitational-wave Signature From Standing Accretion Shock Instability in Supernovae. *Astrophys. J. Lett.*, 829(1):L14, 2016. doi: 10.3847/2041-8205/829/1/L14.
- [10] Ko Nakamura, Shunsaku Horiuchi, Masaomi Tanaka, Kazuhiro Hayama, Tomoya Takiwaki, and Kei Kotake. Multimessenger signals of long-term core-collapse supernova simulations: synergetic observation strategies. *Monthly Notices of the Royal Astronomical Society*, 461(3):3296–3313, 06 2016. ISSN 0035-8711. doi: 10.1093/mnras/stw1453. URL <https://doi.org/10.1093/mnras/stw1453>.

- [11] P. M. Garnavich, B. E. Tucker, A. Rest, E. J. Shaya, R. P. Olling, D. Kasen, and A. Villar. Shock Breakout and Early Light Curves of Type II-P Supernovae Observed with Kepler. *Astrophys. J.*, 820:23, 2016. doi: 10.3847/0004-637X/820/1/23.
- [12] Marek J. Szczepańczyk et al. An Optically Targeted Search for Gravitational Waves emitted by Core-Collapse Supernovae during the Third Observing Run of Advanced LIGO and Advanced Virgo. 5 2023.
- [13] B.P. Abbott et al. Optically targeted search for gravitational waves emitted by core-collapse supernovae during the first and second observing runs of advanced LIGO and advanced Virgo. *Phys. Rev. D*, 101(8):084002, 2020. doi: 10.1103/PhysRevD.101.084002.
- [14] Marek J. Szczepańczyk, Javier M. Antelis, Michael Benjamin, Marco Cavaglia, and ete Gondek-Rosińska. Detecting and reconstructing gravitational waves from the next galactic core-collapse supernova in the advanced detector era. *Phys. Rev. D*, 104:102002, Nov 2021. doi: 10.1103/PhysRevD.104.102002. URL <https://link.aps.org/doi/10.1103/PhysRevD.104.102002>.
- [15] R. Abbott et al. The population of merging compact binaries inferred using gravitational waves through GWTC-3. 11 2021.
- [16] Leo P. Singer and Larry R. Price. Rapid Bayesian position reconstruction for gravitational-wave transients. *Phys. Rev. D*, 93(2):024013, 2016. doi: 10.1103/PhysRevD.93.024013.
- [17] Andrea Zonca, Leo Singer, Daniel Lenz, Martin Reinecke, Cyrille Rosset, Eric Hivon, and Krzysztof Gorski. healpy: equal area pixelization and spherical harmonics transforms for data on the sphere in python. *Journal of Open Source Software*, 4(35):1298, March 2019. doi: 10.21105/joss.01298. URL <https://doi.org/10.21105/joss.01298>.
- [18] K. M. Górski, E. Hivon, A. J. Banday, B. D. Wandelt, F. K. Hansen, M. Reinecke, and M. Bartelmann. HEALPix: A Framework for High-Resolution Discretization and Fast Analysis of Data Distributed on the Sphere. *apj*, 622:759–771, April 2005. doi: 10.1086/427976.
- [19] Yanyan Zheng, Nikolaos Kouvatsos, Jacob Golomb, Marco Cavaglia, Arianna I. Renzini, and Mairi Sakellariadou. Angular power spectrum of gravitational-wave transient sources as a probe of the large-scale structure. *Phys. Rev. Lett.*, 131:171403, Oct 2023. doi: 10.1103/PhysRevLett.131.171403. URL <https://link.aps.org/doi/10.1103/PhysRevLett.131.171403>.
- [20] Albert Einstein. Grundlage der allgemeinen relativit’ats theorie. *Annalen der Physik (ser. 4)*, 49:769–822, 1915.
- [21] J. Abadie et al. Implications for the Origin of GRB 051103 from LIGO Observations. *apj*, 755:2, August 2012. doi: 10.1088/0004-637X/755/1/2.

- [22] B. P. Abbott et al. *Living Rev Relativ*, 21, 2018. doi: <https://doi.org/10.1007/s41114-018-0012-9>.
- [23] B. P. Abbott et al. *Phys. Rev. D*, 93:122003, Jun 2016. doi: 10.1103/PhysRevD.93.122003. URL <https://link.aps.org/doi/10.1103/PhysRevD.93.122003>.
- [24] B.P. Abbott et al. GW170817: Observation of Gravitational Waves from a Binary Neutron Star Inspiral. *Phys. Rev. Lett.*, 119(16):161101, 2017. doi: 10.1103/PhysRevLett.119.161101.
- [25] B.P. Abbott et al. GWTC-1: A Gravitational-Wave Transient Catalog of Compact Binary Mergers Observed by LIGO and Virgo during the First and Second Observing Runs. *Phys. Rev. X*, 9(3):031040, 2019. doi: 10.1103/PhysRevX.9.031040.
- [26] R. Abbott et al. GWTC-2: Compact Binary Coalescences Observed by LIGO and Virgo During the First Half of the Third Observing Run. *Phys. Rev. X*, 11:021053, 2021. doi: 10.1103/PhysRevX.11.021053.
- [27] C. W. Helstrom. Statistical theory of signal detection. 1968.
- [28] Ehud Nakar. Short-hard gamma-ray bursts. *Physics Reports*, 442(1):166–236, 2007. ISSN 0370-1573. doi: <https://doi.org/10.1016/j.physrep.2007.02.005>. URL <https://www.sciencedirect.com/science/article/pii/S0370157307000476>. The Hans Bethe Centennial Volume 1906-2006.
- [29] R. Abbott, T. D. Abbott, S. Abraham, F. Acernese, K. Ackley, The LIGO Scientific Collaboration, and the Virgo Collaboration. Search for gravitational waves associated with gamma-ray bursts detected by fermi and swift during the ligo–virgo run o3a. *The Astrophysical Journal*, 915(2):86, jul 2021. doi: 10.3847/1538-4357/abee15. URL <https://dx.doi.org/10.3847/1538-4357/abee15>.
- [30] R. Abbott et al. Search for gravitational-wave transients associated with magnetar bursts in Advanced LIGO and Advanced Virgo data from the third observing run. 10 2022.
- [31] Florent Robinet, Nicolas Arnaud, Nicolas Leroy, Andrew Lundgren, Duncan Macleod, and Jessica McIver. Omicron: a tool to characterize transient noise in gravitational-wave detectors. *SoftwareX*, 12, December 2020. ISSN 2352-7110. doi: 10.1016/j.softx.2020.100620.
- [32] S. Chatterji, L. Blackburn, G. Martin, and E. Katsavounidis. Multiresolution techniques for the detection of gravitational-wave bursts. *Class. Quant. Grav.*, 21:S1809–S1818, 2004. doi: 10.1088/0264-9381/21/20/024.
- [33] Shourov Keith. Chatterji. The search for gravitational wave bursts in data from the second LIGO science run.

- [34] Rollins J. Multimessenger Astronomy with Low-Latency Searches for Transient Gravitational Waves.
- [35] Elena Cuoco et al. Enhancing Gravitational-Wave Science with Machine Learning. *Mach. Learn. Sci. Tech.*, 2(1):011002, 2021. doi: 10.1088/2632-2153/abb93a.
- [36] Duncan Macleod, Alex L. Urban, Joshua Smith, and Thomas Massinger. gwdechar/hveto: 1.0.1. November 2019. doi: 10.5281/zenodo.3532131. URL <https://doi.org/10.5281/zenodo.3532131>.
- [37] Joshua R. Smith, Thomas Abbott, Eiichi Hirose, Nicolas Leroy, Duncan Macleod, Jessica McIver, Peter Saulson, and Peter Shawhan. A Hierarchical method for vetoing noise transients in gravitational-wave detectors. *Class. Quant. Grav.*, 28: 235005, 2011. doi: 10.1088/0264-9381/28/23/235005.
- [38] Tomoki Isogai, (for the Ligo Scientific Collaboration, and the Virgo Collaboration). Used percentage veto for ligo and virgo binary inspiral searches. *Journal of Physics: Conference Series*, 243(1): 012005, aug 2010. doi: 10.1088/1742-6596/243/1/012005. URL <https://dx.doi.org/10.1088/1742-6596/243/1/012005>.
- [39] summary page. URL <https://summary.ligo.org/>.
- [40] The ligo scientific collaboration and the virgo collaboration 2018 data quality report user documentation. doi: <https://docs.ligo.org/detchar/data-quality-report/>.
- [41] Barthelmy S D. The gcn web site. 2009. doi: <http://gcn.gsfc.nasa.gov/gcn/>.
- [42] Duncan Brown Alex Nitz, Ian Harry et al. *gwastro/pycbc: PyCBC Release v1.15.0*. URL <https://zenodo.org/record/3561157>.
- [43] Cody Messick, Kent Blackburn, Patrick Brady, Patrick Brockill, et al. Analysis framework for the prompt discovery of compact binary mergers in gravitational-wave data. *Phys. Rev. D*, 95:042001, Feb 2017. URL <https://link.aps.org/doi/10.1103/PhysRevD.95.042001>.
- [44] Bruce Allen. *ensuremathchi^2* time-frequency discriminator for gravitational wave detection. *Phys. Rev. D*, 71:062001, Mar 2005. doi: 10.1103/PhysRevD.71.062001. URL <https://link.aps.org/doi/10.1103/PhysRevD.71.062001>.
- [45] B. Abbott, R. Abbott, R. Adhikari, A. Ageev, et al. Search for gravitational waves from galactic and extra-galactic binary neutron stars. *Phys. Rev. D*, 72:082001, Oct 2005. doi: 10.1103/PhysRevD.72.082001. URL <https://link.aps.org/doi/10.1103/PhysRevD.72.082001>.
- [46] B. Abbott, R. Abbott, R. Adhikari, A. Ageev, B. Allen, et al. Search for gravitational waves from primordial black hole binary coalescences in the galactic halo. *Phys. Rev. D*, 72:082002, Oct 2005. doi: 10.1103/PhysRevD.72.082002. URL <https://link.aps.org/doi/10.1103/PhysRevD.72.082002>.

- [47] Samantha A Usman, Alexander H Nitz, Ian W Harry, et al. The PyCBC search for gravitational waves from compact binary coalescence. *Classical and Quantum Gravity*, 33(21):215004, oct 2016. doi: 10.1088/0264-9381/33/21/215004.
- [48] C. Capano, T. Dent, C. Hanna, M. Hendry, C. Messenger, Y.-M. Hu, and J. Veitch. Systematic errors in estimation of gravitational-wave candidate significance. *Phys. Rev. D*, 96:082002, Oct 2017. doi: 10.1103/PhysRevD.96.082002. URL <https://link.aps.org/doi/10.1103/PhysRevD.96.082002>.
- [49] B. P. Abbott et al. *Phys. Rev. D*, 94:102001, Nov 2016. doi: 10.1103/PhysRevD.94.102001. URL <https://link.aps.org/doi/10.1103/PhysRevD.94.102001>.
- [50] S. Klimentenko, G. Vedovato, M. Drago, F. Salemi, V. Tiwari, G. A. Prodi, C. Lazzaro, K. Ackley, S. Tiwari, C. F. Da Silva, and G. Mitselmakher. Method for detection and reconstruction of gravitational wave transients with networks of advanced detectors. *Phys. Rev. D*, 93:042004, Feb 2016. doi: 10.1103/PhysRevD.93.042004. URL <https://link.aps.org/doi/10.1103/PhysRevD.93.042004>.
- [51] S Klimentenko, I Yakushin, A Mercer, and G Mitselmakher. A coherent method for detection of gravitational wave bursts. *Classical and Quantum Gravity*, 25(11): 114029, may 2008. doi: 10.1088/0264-9381/25/11/114029.
- [52] B. P. Abbott et al. All-sky search for gravitational-wave bursts in the second joint ligo-virgo run. *Phys. Rev. D*, 85:122007, 2012. doi: 10.1103/PhysRevD.85.122007. URL <https://journals.aps.org/prd/abstract/10.1103/PhysRevD.85.122007>.
- [53] B. P. Abbott et al. An optically targeted search for gravitational waves emitted by core-collapse supernovae during the first and second observing runs of advanced ligo and advanced virgo. *arXiv:1908.03584*, 2019. URL <https://arxiv.org/abs/1908.03584>.
- [54] B. P. Abbott et al. A guide to LIGOtextendashvirgo detector noise and extraction of transient gravitational-wave signals. *Classical and Quantum Gravity*, 37(5):055002, feb 2020. doi: 10.1088/1361-6382/ab685e.
- [55] 'Eanna 'E. Flanagan and Scott A. Hughes. Measuring gravitational waves from binary black hole coalescences. ii. the waves' information and its extraction, with and without templates. *Phys. Rev. D*, 57:4566–4587, Apr 1998. doi: 10.1103/PhysRevD.57.4566. URL <https://link.aps.org/doi/10.1103/PhysRevD.57.4566>.
- [56] B. P. Abbott et al. *Phys. Rev. Lett.*, 112:131101, Apr 2014. doi: 10.1103/PhysRevLett.112.131101. URL <https://link.aps.org/doi/10.1103/PhysRevLett.112.131101>.
- [57] B. P. Abbott, R. Abbott, T. D. Abbott, et al. Gravitational waves and gamma-rays from a binary neutron star merger: GW170817 and GRB 170817a. *The Astrophysical Journal*, 848(2):L13, oct 2017. doi: 10.3847/2041-8213/aa920c.

- [58] Reinhard Prix. Search for continuous gravitational waves: Metric of the multidetector \mathcal{F} -statistic. *Phys. Rev. D*, 75:023004, Jan 2007. doi: 10.1103/PhysRevD.75.023004. URL <https://link.aps.org/doi/10.1103/PhysRevD.75.023004>.
- [59] Paul Murdin (eds.) Athem W. Alsabti. *Handbook of Supernovae*. Springer, 2016. ISBN 9783319207940; 3319207946. URL libgen.li/file.php?md5=a5362864293ce17c76d4856790adbffb.
- [60] Lesley Murdin, Paul; Murdin. *Supernovae*. Cambridge University Press. p, 1985.
- [61] A. Heger, C. L. Fryer, S. E. Woosley, N. Langer, and D. H. Hartmann. How massive single stars end their life. *The Astrophysical Journal*, 591(1):288, jul 2003. doi: 10.1086/375341. URL <https://dx.doi.org/10.1086/375341>.
- [62] Kiranjyot Gill, Marica Branchesi, Marek Szczepanczyk, Michele Zanolin, and Edo Berger. Gravitational Wave Astronomy Prospectives for Core-Collapse Supernovae Populations. *Bulletin of the AAS*, jul 1 2023. <https://baas.aas.org/pub/2023n4i115p29>.
- [63] Alexei V. Filippenko. Optical Spectra of Supernovae. *araa*, 35:309–355, January 1997. doi: 10.1146/annurev.astro.35.1.309.
- [64] S. E. Woosley, A. Heger, and T. A. Weaver. The evolution and explosion of massive stars. *Rev. Mod. Phys.*, 74:1015–1071, Nov 2002. doi: 10.1103/RevModPhys.74.1015. URL <https://link.aps.org/doi/10.1103/RevModPhys.74.1015>.
- [65] Alexandre Marcowith, Vikram Dwarkadas, Matthieu Renaud, Vincent Tatischeff, and Gwenael Giacinti. Core collapse supernovae as Cosmic Ray sources. *Mon. Not. Roy. Astron. Soc.*, 479(4):4470–4485, 2018. doi: 10.1093/mnras/sty1743.
- [66] Stan Woosley and Thomas Janka. The physics of core-collapse supernovae. *Nature Phys.*, 1:147, 2005. doi: 10.1038/nphys172.
- [67] Ernazar Abdikamalov, Giulia Pagliaroli, and David Radice. Gravitational Waves from Core-Collapse Supernovae. 10 2020.
- [68] Hans-Thomas Janka. Explosion Mechanisms of Core-Collapse Supernovae. *Ann. Rev. Nucl. Part. Sci.*, 62:407–451, 2012. doi: 10.1146/annurev-nucl-102711-094901.
- [69] M. Obergaulinger, M. A. Aloy, and E. Müller. Axisymmetric simulations of magneto-rotational core collapse: dynamics and gravitational wave signal. *aap*, 450:1107, May 2006.
- [70] M. Obergaulinger, M. A. Aloy, H. Dimmelmeier, and E. Müller. Axisymmetric simulations of magnetorotational core collapse: approximate inclusion of general relativistic effects. *aap*, 457:209, October 2006.

- [71] E. Müller, H. Th Janka, and A. Wongwathanarat. Parametrized 3D models of neutrino-driven supernova explosions: Neutrino emission asymmetries and gravitational-wave signals. *Astron. Astrophys.*, 537:1–20, 2012. ISSN 00046361. doi: 10.1051/0004-6361/201117611.
- [72] T. Kuroda and H. Umeda. Three-dimensional Magnetohydrodynamical Simulations of Gravitational Collapse of a $15 M_{sun}$ Star. *apjs*, 191:439, December 2010.
- [73] A. Mezzacappa, M. Liebend” orfer, O. E. Messer, W. R. Hix, F. Thielemann, and S. W. Bruenn. Simulation of the Spherically Symmetric Stellar Core Collapse, Bounce, and Postbounce Evolution of a Star of 13 Solar Masses with Boltzmann Neutrino Transport, and Its Implications for the Supernova Mechanism. *Phys. Rev. Lett.*, 86:1935, March 2001.
- [74] W. G. Anderson, P. R. Brady, J. D. Creighton, and ’E. ’E. Flanagan. Excess power statistic for detection of burst sources of gravitational radiation. *prd*, 63(4):042003, February 2001. doi: 10.1103/PhysRevD.63.042003.
- [75] Anthony Mezzacappa, Pedro Marronetti, Ryan E. Landfield, Eric J. Lentz, Konstantin N. Yakunin, Stephen W. Bruenn, W. Raphael Hix, O. E. Bronson Messer, Eirik Endeve, John M. Blondin, and J. Austin Harris. Gravitational-wave signal of a core-collapse supernova explosion of a $15 M_{ensuremathdot}$ star. *prd*, 102(2):023027, July 2020. doi: 10.1103/PhysRevD.102.023027.
- [76] M. Obergaulinger and M. ’A. Aloy. Magnetorotational core collapse of possible GRB progenitors - III. Three-dimensional models. *mnras*, 503(4):4942–4963, May 2021. doi: 10.1093/mnras/stab295.
- [77] Anthony Mezzacappa, Eirik Endeve, O. E. Bronson Messer, and Stephen W. Bruenn. Physical, numerical, and computational challenges of modeling neutrino transport in core-collapse supernovae. 10 2020.
- [78] David Radice, Viktoriya Morozova, Adam Burrows, David Vartanyan, and Hiroki Nagakura. Characterizing the Gravitational Wave Signal from Core-collapse Supernovae. *apjl*, 876(1):L9, May 2019. doi: 10.3847/2041-8213/ab191a.
- [79] Takami Kuroda, Kei Kotake, Tomoya Takiwaki, and Friedrich-Karl Thielemann. A full general relativistic neutrino radiation-hydrodynamics simulation of a collapsing very massive star and the formation of a black hole. *Mon. Not. R. Astron. Soc. Lett.*, 84:80–84, 2018. ISSN 1745-3925. doi: 10.1093/mnrasl/sly059.
- [80] Takami Kuroda, Kei Kotake, and Tomoya Takiwaki. A New Gravitational-wave Signature from Standing Accretion Shock Instability in Supernovae. *apjl*, 829(1): L14, September 2016. doi: 10.3847/2041-8205/829/1/L14.
- [81] Evan P. O’Connor and Sean M. Couch. Exploring Fundamentally Three-dimensional Phenomena in High-fidelity Simulations of Core-collapse Supernovae. *apj*, 865(2): 81, October 2018. doi: 10.3847/1538-4357/aadcf7.

- [82] Laurie Walk, Thierry Foglizzo, and Irene Tamborra. Standing accretion shock instability in the collapse of a rotating stellar core. *Phys. Rev. D*, 107(6):063014, 2023. doi: 10.1103/PhysRevD.107.063014.
- [83] S. Scheidegger, R. Kappeli, S. C. Whitehouse, T. Fischer, and M. Liebendörfer. The influence of model parameters on the prediction of gravitational wave signals from stellar core collapse. *aap*, 514:A51, May 2010. doi: 10.1051/0004-6361/200913220.
- [84] H. Andresen, E. Müller, H. T. Janka, A. Summa, K. Gill, and M. Zanolin. Gravitational waves from 3D core-collapse supernova models: The impact of moderate progenitor rotation. *Mon. Not. R. Astron. Soc.*, 486(2):2238–2253, 2019. ISSN 13652966. doi: 10.1093/mnras/stz990.
- [85] Patrick J. Sutton. A Rule of Thumb for the Detectability of Gravitational-Wave Bursts. 3 2013.
- [86] K. Hirata, T. Kajita, M. Koshiba, M. Nakahata, and Y. Oyama. Observation of a neutrino burst from the supernova SN1987A. *Phys. Rev. Lett.*, 58:1490, April 1987. doi: 10.1103/PhysRevLett.58.1490.
- [87] R. Svoboda, C. B. Bratton, D. Casper, A. Ciocio, and R. Claus. Neutrinos from SN1987A in the IMB detector. In I. J. Danziger, editor, *European Southern Observatory Conference and Workshop Proceedings*, volume 26 of *European Southern Observatory Conference and Workshop Proceedings*, page 229, 1987.
- [88] S. W. Bruenn. Neutrinos from SN1987A and current models of stellar-core collapse. *prl*, 59:938, August 1987. doi: 10.1103/PhysRevLett.59.938.
- [89] G. Pagliaroli, F. Vissani, M. L. Costantini, and A. Ianni. Improved analysis of SN1987A antineutrino events. *Astropart. Phys.*, 31:163, April 2009. doi: 10.1016/j.astropartphys.2008.12.010.
- [90] F. Vissani. Comparative analysis of SN1987A antineutrino fluence. *J. Phys. G, Nuc. Phys.*, 42(1):013001, January 2015. doi: 10.1088/0954-3899/42/1/013001.
- [91] Super-Kamiokande. URL <http://neutrino.phys.washington.edu/superk>.
- [92] M. Ikeda et al. Search for Supernova Neutrino Bursts at Super-Kamiokande. *apj*, 669:519, 2007. doi: 10.1086/521547.
- [93] F. Halzen and G. G. Raffelt. Reconstructing the supernova bounce time with neutrinos in IceCube. *prd*, 80(8):087301, October 2009. doi: 10.1103/PhysRevD.80.087301.
- [94] R. Abbasi, Y. Abdou, and T. Abu-Zayyad et al. Icecube sensitivity for low-energy neutrinos from nearby supernovae. *aap*, 535:A109, November 2011. doi: 10.1051/0004-6361/201117810.
- [95] E. N. Alekseev, L. N. Alekseeva, I. V. Krivosheina, and V. I. Volchenko. Detection of the neutrino signal from SN 1987A using the INR Baksan underground scintillation telescope. 26:237–247, 1987.

- [96] Borexino. URL <http://borex.lngs.infn.it>.
- [97] HALO. URL <http://www.snolab.ca/halo/index.html>. Helium and Lead Observatory.
- [98] KamLAND. URL <http://www.awa.tohoku.ac.jp/KamLAND/>.
- [99] URL <http://www.bo.infn.it/lvd>. Large Volume Detector.
- [100] etc Michele Zanolin, Michael BenjaminMichele. On source window,ligo-t2000543.
- [101] S. Klimenko et al. Method for detection and reconstruction of gravitational wave transients with networks of advanced detectors. *Phys. Rev. D*, 93:042004, Feb 2016. doi: 10.1103/PhysRevD.93.042004.
- [102] G. Vedovato S. Klimenko and M. Drago. Method for detection and reconstruction of gravitational wave transients with networks of advanced detectors. *Phys. Rev. D*, 93:042004, Feb 2016. URL <https://journals.aps.org/prd/abstract/10.1103/PhysRevD.93.042004>.
- [103] V. Necula, S. Klimenko, and G. Mitselmakher. Transient analysis with fast Wilson-Daubechies time-frequency transform. *J. Phys. Conf. Ser.*, 363:012032, 2012. doi: 10.1088/1742-6596/363/1/012032.
- [104] Marek Szczepanczyk et al. Detecting and reconstructing gravitational waves from the next galactic core-collapse supernova in the advanced detector era. *Phys. Rev. D*, 104(10):102002, 2021. doi: 10.1103/PhysRevD.104.102002.
- [105] S. E. Gossan, P. Sutton, A. Stuver, M. Zanolin, K. Gill, and C. D. Ott. Observing gravitational waves from core-collapse supernovae in the advanced detector era. *Phys. Rev. D*, 93:042002, Feb 2016. doi: 10.1103/PhysRevD.93.042002. URL <http://link.aps.org/doi/10.1103/PhysRevD.93.042002>.
- [106] J. Aasi et al. Advanced LIGO. *Class. Quant. Grav.*, 32:074001, 2015. doi: 10.1088/0264-9381/32/7/074001.
- [107] F. Acernese et al. Advanced Virgo: a second-generation interferometric gravitational wave detector. *Class. Quant. Grav.*, 32(2):024001, 2015. doi: 10.1088/0264-9381/32/2/024001.
- [108] K. L. Dooley et al. GEO 600 and the GEO-HF upgrade program: successes and challenges. *Class. Quant. Grav.*, 33:075009, 2016. doi: 10.1088/0264-9381/33/7/075009.
- [109] B. P. Abbott et al. First targeted search for gravitational-wave bursts from core-collapse supernovae in data of first-generation laser interferometer detectors. *Phys. Rev. D*, 94:102001, Nov 2016. doi: 10.1103/PhysRevD.94.102001. URL <https://link.aps.org/doi/10.1103/PhysRevD.94.102001>.

- [110] Yoichi Aso, Yuta Michimura, Kentaro Somiya, Masaki Ando, Osamu Miyakawa, Takanori Sekiguchi, Daisuke Tatsumi, and Hiroaki Yamamoto. Interferometer design of the KAGRA gravitational wave detector. *Phys. Rev. D*, 88(4):043007, 2013. doi: 10.1103/PhysRevD.88.043007.
- [111] B. P. Abbott et al. All-sky search for short gravitational-wave bursts in the first advanced LIGO run. *Physical Review D*, 95(4):042003, feb 2017. doi: 10.1103/physrevd.95.042003. URL <https://doi.org/10.1103/physrevd.95.042003>.
- [112] B. P. Abbott et al. All-sky search for short gravitational-wave bursts in the second Advanced LIGO and Advanced Virgo run. *Phys. Rev. D*, 100:024017, Jul 2019. doi: 10.1103/PhysRevD.100.024017. URL <https://link.aps.org/doi/10.1103/PhysRevD.100.024017>.
- [113] R. Abbott et al. All-sky search for short gravitational-wave bursts in the third Advanced LIGO and Advanced Virgo run. *Phys. Rev. D*, 104(12):122004, 2021. doi: 10.1103/PhysRevD.104.122004.
- [114] R. Abbott et al. First joint observation by the underground gravitational-wave detector KAGRA with GEO 600. *Prog. Theor. Exp. Phys.*, 2022(6), 04 2022. ISSN 2050-3911. doi: 10.1093/ptep/ptac073. URL <https://doi.org/10.1093/ptep/ptac073.063F01>.
- [115] Robert E. Rutledge. The astronomer’s telegram: A web-based short-notice publication system for the professional astronomical community. *Publications of the Astronomical Society of the Pacific*, 110(748):754–756, jun 1998. doi: 10.1086/316184. URL <https://doi.org/10.1086/316184>.
- [116] B. J. Shappee et al. THE MAN BEHIND THE CURTAIN: X-RAYS DRIVE THE UV THROUGH NIR VARIABILITY IN THE 2013 ACTIVE GALACTIC NUCLEUS OUTBURST IN NGC 2617. *The Astrophysical Journal*, 788(1):48, may 2014. doi: 10.1088/0004-637x/788/1/48. URL <https://doi.org/10.1088/0004-637x/788/1/48>.
- [117] T W-S Holoiien et al. The ASAS-SN bright supernova catalogue – IV. 2017. *Monthly Notices of the Royal Astronomical Society*, 484(2):1899–1911, 01 2019. ISSN 0035-8711. doi: 10.1093/mnras/stz073. URL <https://doi.org/10.1093/mnras/stz073>.
- [118] D. Godoy-Rivera et al. The ASAS-SN bright supernova catalogue – III. 2016. *Monthly Notices of the Royal Astronomical Society*, 471(4):4966–4981, 08 2017. ISSN 0035-8711. doi: 10.1093/mnras/stx1544. URL <https://doi.org/10.1093/mnras/stx1544>.
- [119] D. Godoy-Rivera et al. The ASAS-SN bright supernova catalogue – II. 2015. *Monthly Notices of the Royal Astronomical Society*, 467(1):1098–1111, 01 2017. ISSN 0035-8711. doi: 10.1093/mnras/stx057. URL <https://doi.org/10.1093/mnras/stx057>.

- [120] L. Tartaglia et al. The discovery of DLT17ch/AT 2017gax with PROMPT. *The Astronomer's Telegram*, 10638, August 2017. URL <http://adsabs.harvard.edu/abs/2017ATel10638...1T>.
- [121] T. Prusti et al. The Gaia mission. *aap*, 595:A1, Nov 2016. doi: 10.1051/0004-6361/201629272.
- [122] A. G. A. Brown et al. Gaia Data Release 1. Summary of the astrometric, photometric, and survey properties. *aap*, 595:A2, Nov 2016. doi: 10.1051/0004-6361/201629512.
- [123] ASRAS. [urlwww.rochesterastronomy.org](http://www.rochesterastronomy.org), 2018. Accessed: 2022-06-05.
- [124] L. Tartaglia et al. The Early Detection and Follow-up of the Highly Obscured Type II Supernova 2016ija/HLT16am. *apj*, 853:62, January 2018. doi: 10.3847/1538-4357/aaa014.
- [125] James Guillochon, Jerod Parrent, Luke Zoltan Kelley, and Raffaella Margutti. An Open Catalog for Supernova Data. *apj*, 835(1):64, Jan 2017. doi: 10.3847/1538-4357/835/1/64.
- [126] CBAT. [urlhttp://www.cbat.eps.harvard.edu/cbat.html](http://www.cbat.eps.harvard.edu/cbat.html), 2018. Accessed: 2022-06-05.
- [127] J. Grzegorzek. PSH Transient Discovery Report for 2019-04-29. *Transient Name Server Discovery Report*, 2019-666:1, April 2019.
- [128] Tatsuya Nakaoka et al. Calcium-rich Transient SN 2019ehk in a Star-forming Environment: Yet Another Candidate for a Precursor of a Double Neutron-star Binary. *Astrophys. J.*, 912(1):30, 2021. doi: 10.3847/1538-4357/abe765.
- [129] Alexander Gagliano et al. An Early-time Optical and Ultraviolet Excess in the Type-Ic SN 2020oi. *Astrophys. J.*, 924(2):55, 2022. doi: 10.3847/1538-4357/ac35ec.
- [130] Yuhan Yao et al. SN2019dge: a Helium-rich Ultra-Stripped Envelope Supernova. *Astrophys. J.*, 900(1):46, 2020. doi: 10.3847/1538-4357/abaa3d.
- [131] Kishalay De, U. Christoffer Fremling, Avishay Gal-Yam, Ofer Yaron, Mansi M. Kasliwal, and S. R. Kulkarni. The Peculiar Ca-rich SN2019ehk: Evidence for a Type IIb Core-collapse Supernova from a Low-mass Stripped Progenitor. *Astrophys. J. Lett.*, 907(1):L18, 2021. doi: 10.3847/2041-8213/abd627.
- [132] Wynn V. Jacobson-Gal'an et al. Late-time Observations of Calcium-Rich Transient SN 2019ehk Reveal a Pure Radioactive Decay Power Source. *Astrophys. J. Lett.*, 908(2):L32, 2021. doi: 10.3847/2041-8213/abdebc.
- [133] Wynn V. Jacobson-Gal'an et al. SN 2019ehk: A Double-Peaked Ca-rich Transient with Luminous X-ray Emission and Shock-Ionized Spectral Features. *Astrophys. J.*, 898(2):166, 2020. doi: 10.3847/1538-4357/ab9e66.
- [134] J. Tonry et al. ATLAS Transient Discovery Report for 2019-05-02. *Transient Name Server Discovery Report*, 2019-687:1, May 2019.

- [135] Seo-Won Chang, Christopher A. Onken, Christian Wolf, Lance Luvaul, Anais M'oller, Richard Scalzo, Brian P. Schmidt, Susan M. Scott, Nikunj Sura, and Fang Yuan. SkyMapper optical follow-up of gravitational wave triggers: Alert science data pipeline and LIGO/Virgo O3 run. *Publ. Astron. Soc. Austral.*, 38:e024, 2021. doi: 10.1017/pasa.2021.17.
- [136] G. Theureau, M. O. Hanski, N. Coudreau, N. Hallet, and J. M. Martin. Kinematics of the Local Universe. XIII. 21-cm line measurements of 452 galaxies with the Nanccay radiotelescope, JHK Tully-Fisher relation, and preliminary maps of the peculiar velocity field. *aap*, 465(1):71–85, April 2007. doi: 10.1051/0004-6361:20066187.
- [137] K. Z. Stanek, D. Bersier, and C. S. Kochanek. ASAS-SN Transient Discovery Report for 2019-05-13. *Transient Name Server Discovery Report*, 2019-766:1, May 2019.
- [138] K. Z. Stanek. ASAS-SN Transient Discovery Report for 2019-06-18. *Transient Name Server Discovery Report*, 2019-1030:1, June 2019.
- [139] Kishalay De et al. Palomar Gattini-IR: Survey overview, data processing system, on-sky performance and first results. *Publ. Astron. Soc. Pac.*, 132(1008):025001, 2020. doi: 10.1088/1538-3873/ab6069.
- [140] F. Forster et al. ALeRCE/ZTF Transient Discovery Report for 2020-01-07. *Transient Name Server Discovery Report*, 2020-67:1, January 2020.
- [141] Keiichi Maeda et al. The Final Months of Massive Star Evolution from the Circumstellar Environment around SN Ic 2020oi. *Astrophys. J.*, 918(1):34, 2021. doi: 10.3847/1538-4357/ac0dbc.
- [142] Samaporn Tinyanont et al. Infrared spectropolarimetric detection of intrinsic polarization from a core-collapse supernova. *Nature Astron.*, 5(6):544–551, 2021. doi: 10.1038/s41550-021-01320-4.
- [143] et. al. J. Rho. *The Astrophysical Journal*, 908(2):232, feb 2021.
- [144] David N. Burrows et al. The Swift X-ray Telescope. *Space Sci. Rev.*, 120:165, 2005. doi: 10.1007/s11214-005-5097-2.
- [145] Assaf Horesh et al. A Non-equipartition Shock Wave Traveling in a Dense Circumstellar Environment around SN 2020oi. *Astrophys. J.*, 903(2):132, 2020. doi: 10.3847/1538-4357/abbd38.
- [146] J. Nordin, V. Brinnel, M. Giomi, J. V. Santen, A. Gal-Yam, O. Yaron, and S. Schulze. ZTF Transient Discovery Report for 2020-02-19. *Transient Name Server Discovery Report*, 2020-555:1, February 2020.
- [147] Alexandra Kozyreva, Hans-Thomas Janka, Daniel Kresse, Stefan Taubenberger, and Petr Baklanov. Low-luminosity type IIP supernovae: SN 2005cs and SN 2020cxid as very low-energy iron core-collapse explosions. *Mon. Not. Roy. Astron. Soc.*, 514(3):4173–4189, 2022. doi: 10.1093/mnras/stac1518.

- [148] S. Yang et al. A low-energy explosion yields the underluminous Type IIP SN 2020cxd. *Astron. Astrophys.*, 655:A90, 2021. doi: 10.1051/0004-6361/202141244.
- [149] Daniel A. Perley et al. The Zwicky Transient Facility Bright Transient Survey. II. A Public Statistical Sample for Exploring Supernova Demographics. *Astrophys. J.*, 904(1):35, 2020. doi: 10.3847/1538-4357/abbd98.
- [150] G. Valerin et al. Low luminosity Type II supernovae textendash IV. SN 2020cxd and SN 2021aai, at the edges of the sub-luminous supernovae class. *Mon. Not. Roy. Astron. Soc.*, 513(4):4983–4999, 2022. doi: 10.1093/mnras/stac1182.
- [151] P. Wiggins. Transient Discovery Report for 2020-02-27. *Transient Name Server Discovery Report*, 2020-653:1, February 2020.
- [152] F. Forster et al. ALeRCE/ZTF Transient Discovery Report for 2020-03-31. *Transient Name Server Discovery Report*, 2020-914:1, March 2020.
- [153] Samaporn Tinyanont et al. Progenitor and close-in circumstellar medium of type II supernova 2020fqv from high-cadence photometry and ultra-rapid UV spectroscopy. *Mon. Not. Roy. Astron. Soc.*, 512(2):2777–2797, 2022. doi: 10.1093/mnras/stab2887.
- [154] Kiranjyot Gill, Griffin Hosseinzadeh, Edo Berger, Michele Zanolin, and Marek Szcze panczyk. Constraining the Time of Gravitational-wave Emission from Core-collapse Supernovae. *Astrophys. J.*, 931(2):159, 2022. doi: 10.3847/1538-4357/ac5631.
- [155] S. Karki et al. The Advanced LIGO Photon Calibrators. *Rev. Sci. Instrum.*, 87(11):114503, 2016. doi: 10.1063/1.4967303.
- [156] Craig Cahillane et al. Calibration uncertainty for Advanced LIGO’s first and second observing runs. *Phys. Rev. D*, 96(10):102001, 2017. doi: 10.1103/PhysRevD.96.102001.
- [157] Aaron Viets et al. Reconstructing the calibrated strain signal in the Advanced LIGO detectors. *Class. Quant. Grav.*, 35(9):095015, 2018. doi: 10.1088/1361-6382/aab658.
- [158] Ling Sun, Evan Goetz, Jeffrey S Kissel, et al. Characterization of systematic error in advanced ligo calibration. *Classical and Quantum Gravity*, 37(22):225008, oct 2020. doi: 10.1088/1361-6382/abb14e. URL <https://dx.doi.org/10.1088/1361-6382/abb14e>.
- [159] Ling Sun et al. Characterization of systematic error in Advanced LIGO calibration in the second half of O3. 6 2021.
- [160] F. Acernese et al. Calibration of advanced virgo and reconstruction of the gravitational wave signal $h(t)$ during the observing run o2. *Class. Quant. Grav.*, 35(20):205004, 2018. doi: 10.1088/1361-6382/aadf1a.

- [161] F. Acernese et al. Calibration of advanced virgo and reconstruction of detector strain $h(t)$ during the observing run o3. 7 2021.
- [162] B. P. Abbott et al. Characterization of transient noise in Advanced LIGO relevant to gravitational wave signal GW150914. *Class. Quant. Grav.*, 33(13):134001, 2016. doi: 10.1088/0264-9381/33/13/134001.
- [163] Benjamin P Abbott et al. A guide to LIGO-Virgo detector noise and extraction of transient gravitational-wave signals. *Class. Quant. Grav.*, 37(5):055002, 2020. doi: 10.1088/1361-6382/ab685e.
- [164] Derek Davis et al. LIGO detector characterization in the second and third observing runs. *Class. Quant. Grav.*, 38(13):135014, 2021. doi: 10.1088/1361-6382/abfd85.
- [165] Philippe Nguyen et al. Environmental noise in advanced LIGO detectors. *Class. Quant. Grav.*, 38(14):145001, 2021. doi: 10.1088/1361-6382/ac011a.
- [166] Irene Fiori et al. The hunt for environmental noise in virgo during the third observing run. *Galaxies*, 8(4):82, 2020. doi: 10.3390/galaxies8040082.
- [167] F. Acernese et al. Virgo Detector Characterization and Data Quality: tools. 10 2022.
- [168] F. Acernese et al. Virgo Detector Characterization and Data Quality: results from the O3 run. 10 2022.
- [169] J. C. Driggers et al. Improving astrophysical parameter estimation via offline noise subtraction for Advanced LIGO. *Phys. Rev. D*, 99(4):042001, 2019. doi: 10.1103/PhysRevD.99.042001.
- [170] D. Davis, T. J. Massinger, A. P. Lundgren, J. C. Driggers, A. L. Urban, and L. K. Nuttall. Improving the Sensitivity of Advanced LIGO Using Noise Subtraction. *Class. Quant. Grav.*, 36:055011, 2019. doi: 10.1088/1361-6382/ab01c5.
- [171] B. P. Abbott et al. Characterization of transient noise in advanced ligo relevant to gravitational wave signal gw150914. *Classical and Quantum Gravity*, 33(13):134001, 2016. URL <http://stacks.iop.org/0264-9381/33/i=13/a=134001>.
- [172] Miriam Cabero et al. Blip glitches in Advanced LIGO data. *Class. Quant. Grav.*, 36(15):15, 2019. doi: 10.1088/1361-6382/ab2e14.
- [173] H. Andresen, B. Müller, E. Müller, and H.-Th. Janka. Gravitational wave signals from 3D neutrino hydrodynamics simulations of core-collapse supernovae. *Mon. Not. R. Astron. Soc.*, 468(2):2032–2051, 2017. ISSN 0035-8711. doi: 10.1093/mnras/stx618.
- [174] E. Müller, H.-T. Janka, and A. Wongwathanarat. Parametrized 3D models of neutrino-driven supernova explosions. Neutrino emission asymmetries and gravitational-wave signals. *aap*, 537:A63, January 2012. doi: 10.1051/0004-6361/201117611.

- [175] B. Paxton, L. Bildsten, A. Dotter, F. Herwig, P. Lesaffre, and F. Timmes. Modules for Experiments in Stellar Astrophysics (MESA). *apjs*, 192:3, jan 2011. doi: 10.1088/0067-0049/192/1/3.
- [176] B. Paxton, M. Cantiello, P. Arras, L. Bildsten, E. F. Brown, A. Dotter, C. Mankovich, M. H. Montgomery, D. Stello, F. X. Timmes, and R. Townsend. Modules for Experiments in Stellar Astrophysics (MESA): Planets, Oscillations, Rotation, and Massive Stars. *apjs*, 208:4, sep 2013. doi: 10.1088/0067-0049/208/1/4.
- [177] B. Paxton, P. Marchant, J. Schwab, E. B. Bauer, L. Bildsten, M. Cantiello, L. Dessart, R. Farmer, H. Hu, N. Langer, R. H. D. Townsend, D. M. Townsley, and F. X. Timmes. Modules for Experiments in Stellar Astrophysics (MESA): Binaries, Pulsations, and Explosions. *apjs*, 220:15, sep 2015. doi: 10.1088/0067-0049/220/1/15.
- [178] B. Paxton, J. Schwab, E. B. Bauer, L. Bildsten, S. Blinnikov, P. Duffell, R. Farmer, J. A. Goldberg, P. Marchant, E. Sorokina, A. Thoul, R. H. D. Townsend, and F. X. Timmes. Modules for Experiments in Stellar Astrophysics (MESA): Convective Boundaries, Element Diffusion, and Massive Star Explosions. *apjs*, 234:34, feb 2018. doi: 10.3847/1538-4365/aaa5a8.
- [179] Bill Paxton, R. Smolec, Josiah Schwab, A. Gautschy, Lars Bildsten, Matteo Cantiello, Aaron Dotter, R. Farmer, Jared A. Goldberg, Adam S. Jermyn, S. M. Kanbur, Pablo Marchant, Anne Thoul, Richard H. D. Townsend, William M. Wolf, Michael Zhang, and F. X. Timmes. Modules for Experiments in Stellar Astrophysics (MESA): Pulsating Variable Stars, Rotation, Convective Boundaries, and Energy Conservation. *apjs*, 243(1):10, Jul 2019. doi: 10.3847/1538-4365/ab2241.
- [180] Adam S. Jermyn, Evan B. Bauer, Josiah Schwab, R. Farmer, Warrick H. Ball, Earl P. Bellinger, Aaron Dotter, Meridith Joyce, Pablo Marchant, Joey S. G. Mombarg, William M. Wolf, Tin Long Sunny Wong, Giulia C. Cinquegrana, Eoin Farrell, R. Smolec, Anne Thoul, Matteo Cantiello, Falk Herwig, Odette Toloza, Lars Bildsten, Richard H. D. Townsend, and F. X. Timmes. Modules for Experiments in Stellar Astrophysics (MESA): Time-dependent Convection, Energy Conservation, Automatic Differentiation, and Infrastructure. *apjs*, 265(1):15, March 2023. doi: 10.3847/1538-4365/acae8d.
- [181] Jade Powell and Bernhard M’uller. Gravitational wave emission from 3D explosion models of core-collapse supernovae with low and normal explosion energies. *mnras*, 487(1):1178–1190, July 2019. doi: 10.1093/mnras/stz1304.
- [182] Kuo-Chuan Pan, Matthias Liebend’orfer, Sean M. Couch, and Friedrich-Karl Thielemann. Stellar Mass Black Hole Formation and Multimessenger Signals from Three-dimensional Rotating Core-collapse Supernova Simulations. *apj*, 914(2):140, June 2021. doi: 10.3847/1538-4357/abfb05.
- [183] Takami Kuroda, Tobias Fischer, Tomoya Takiwaki, and Kei Kotake. Core-collapse Supernova Simulations and the Formation of Neutron Stars, Hybrid Stars, and Black Holes. *Astrophys. J.*, 924(1):38, 2022. doi: 10.3847/1538-4357/ac31a8.

- [184] Hideyuki Umeda and Ken'ichi Nomoto. How much Ni-56 can be produced in Core-Collapse Supernovae? Evolution and Explosions of 30-100 Msun Stars. *Astrophys. J.*, 673:1014, 2008. doi: 10.1086/524767.
- [185] D. Lai and S. L. Shapiro. Gravitational radiation from rapidly rotating nascent neutron stars. *apj*, 442:259, 1995.
- [186] J. D. Brown. Rotational Instabilities in post-Collapse Stellar Cores. In *AIP Conf. Proc. 575: Astrophysical Sources for Ground-Based Gravitational Wave Detectors*, page 234, 2001.
- [187] M. Shibata and Y.-I. Sekiguchi. Three-dimensional simulations of stellar core collapse in full general relativity: Nonaxisymmetric dynamical instabilities. *prd*, 71:024014, January 2005. doi: 10.1103/physrevd.71.024014. URL <https://doi.org/10.1103/physrevd.71.024014>.
- [188] M. Rampp, E. Müller, and M. Ruffert. Simulations of non-axisymmetric rotational core collapse. *aap*, 332:969, April 1998.
- [189] Thierry Bugli Matteo, Foglizzo et al. Three-dimensional core-collapse supernovae with complex magnetic structures: II. Rotational instabilities and multimessenger signatures. 10 2022.
- [190] Shota Shibagaki, Takami Kuroda, Kei Kotake, and Tomoya Takiwaki. A new gravitational-wave signature of low-T/W instability in rapidly rotating stellar core collapse. *mnras*, 493(1):L138–L142, March 2020. doi: 10.1093/mnras/laa021.
- [191] C. D. Ott. GWs from Bar-mode Instabilities. Technical Report LIGO-T1000553-v2, LIGO Scientific Collaboration, 2010. URL <https://dcc.ligo.org/LIGO-T1000553-v2/public>.
- [192] Gravitational wave emission from the bar-mode instability in core-collapse supernovae. *Virgo Technical Documentation System*, (VIR-0719C-21), 2021.
- [193] G. Pietrzyński et al. A distance to the large magellanic cloud that is precise to one per cent. *Nature*, 567(7747):200–203, mar 2019. doi: 10.1038/s41586-019-0999-4. URL <https://doi.org/10.1038/s41586-019-0999-4>.
- [194] B. P. et. al. Abbott. All-sky search for continuous gravitational waves from isolated neutron stars using advanced ligo o2 data. *Phys. Rev. D*, 100:024004, Jul 2019. doi: 10.1103/PhysRevD.100.024004. URL <https://link.aps.org/doi/10.1103/PhysRevD.100.024004>.
- [195] Stirling A. Colgate and Richard H. White. The Hydrodynamic Behavior of Supernovae Explosions. *apj*, 143:626, March 1966. doi: 10.1086/148549.
- [196] A. Marek, H. Th. Janka, and E. Mueller. Equation-of-State Dependent Features in Shock-Oscillation Modulated Neutrino and Gravitational-Wave Signals from Supernovae. *Astron. Astrophys.*, 496:475, 2009. doi: 10.1051/0004-6361/200810883.

- [197] J. W. Murphy, C. D. Ott, and A. Burrows. A Model for Gravitational Wave Emission from Neutrino-Driven Core-Collapse Supernovae. *apj*, 707:1173, December 2009.
- [198] Konstantin N. Yakunin et al. Gravitational Waves from Core Collapse Supernovae. *Class. Quant. Grav.*, 27:194005, 2010. doi: 10.1088/0264-9381/27/19/194005.
- [199] M. Rampp, E. Mueller, and M. Ruffert. Simulations of non-axisymmetric rotational core collapse. *Astron. Astrophys.*, 332:969, 1998.
- [200] T. Zwerger and E. Müller. Dynamics and gravitational wave signature of axisymmetric rotational core collapse. *aap*, 320:209, April 1997.
- [201] M. Bugli, J. Guilet, M. Obergaulinger, P. Cerdá-Durán, and M. Á. Aloy. The impact of non-dipolar magnetic fields in core-collapse supernovae. *Mon. Not. Roy. Astron. Soc.*, 492(1):58–71, 2020. doi: 10.1093/mnras/stz3483.
- [202] M. Obergaulinger and M. A. Aloy. Magnetorotational core collapse of possible GRB progenitors textendash I. Explosion mechanisms. *Mon. Not. Roy. Astron. Soc.*, 492(4):4613–4634, 2020. doi: 10.1093/mnras/staa096.
- [203] Kuo-Chuan Pan, Matthias Liebendörfer, Sean M. Couch, and Friedrich-Karl Thielemann. Equation of State Dependent Dynamics and Multi-messenger Signals from Stellar-mass Black Hole Formation. *Astrophys. J.*, 857(1):13, 2018. doi: 10.3847/1538-4357/aab71d.
- [204] Kuo-Chuan Pan, Matthias Liebendörfer, Sean Couch, and Friedrich-Karl Thielemann. Stellar Mass Black Hole Formation and Multi-messenger Signals from Three Dimensional Rotating Core-Collapse Supernova Simulations. 10 2020.
- [205] Jade Powell, Bernhard Müller, and Alexander Heger. The final core collapse of pulsational pair instability supernovae. *arXiv e-prints*, art. arXiv:2101.06889, January 2021.
- [206] James M. Lattimer and F. Douglas Swesty. A Generalized equation of state for hot, dense matter. *Nucl. Phys. A*, 535:331–376, 1991. doi: 10.1016/0375-9474(91)90452-C.
- [207] H. Shen, H. Toki, K. Oyamatsu, and K. Sumiyoshi. RELATIVISTIC EQUATION OF STATE FOR CORE-COLLAPSE SUPERNOVA SIMULATIONS. *The Astrophysical Journal Supplement Series*, 197(2):20, nov 2011. doi: 10.1088/0067-0049/197/2/20. URL <https://doi.org/10.1088/0067-0049/197/2/20>.
- [208] Matthias Hempel and Jurgen Schaffner-Bielich. Statistical Model for a Complete Supernova Equation of State. *Nucl. Phys. A*, 837:210–254, 2010. doi: 10.1016/j.nuclphysa.2010.02.010.
- [209] Andrew W. Steiner, Matthias Hempel, and Tobias Fischer. Core-collapse supernova equations of state based on neutron star observations. *Astrophys. J.*, 774:17, 2013. doi: 10.1088/0004-637X/774/1/17.

- [210] H. Dimmelmeier, J. Novak, J. A. Font, J. M. Ib'anez, and E. Müller. Combining spectral and shock-capturing methods: A new numerical approach for 3D relativistic core collapse simulations. *prd*, 71:064023, March 2005.
- [211] Bernhard Müller, Hans-Thomas Janka, and Harald Dimmelmeier. A new multi-dimensional general relativistic neutrino hydrodynamics code for core-collapse supernovae. I. Method and code tests in spherical symmetry. *Astrophys. J. Suppl.*, 189:104–133, 2010. doi: 10.1088/0067-0049/189/1/104.
- [212] Bruce Fryxell, Ewald Müller, and David Arnett. Instabilities and Clumping in SN 1987A. I. Early Evolution in Two Dimensions. *apj*, 367:619, February 1991. doi: 10.1086/169657.
- [213] Stephen W. Bruenn et al. CHIMERA: A Massively Parallel Code for Core-collapse Supernova Simulations. *Astrophys. J. Suppl.*, 248(1):11, 2020. doi: 10.3847/1538-4365/ab7aff.
- [214] Anshu Dubey, Katie Antypas, Murali K. Ganapathy, Lynn B. Reid, Katherine Riley, Dan Sheeler, Andrew Siegel, and Klaus Weide. Extensible component-based architecture for flash, a massively parallel, multi-physics simulation code. *Parallel Computing*, 35(10):512 – 522, 2009. ISSN 0167-8191. doi: <https://doi.org/10.1016/j.parco.2009.08.001>. URL <http://www.sciencedirect.com/science/article/pii/S0167819109000945>.
- [215] C. D. Ott, E. Abdikamalov, E. O'Connor, C. Reisswig, R. Haas, P. Kalmus, S. Drasco, A. Burrows, and E. Schnetter. Correlated Gravitational Wave and Neutrino Signals from General-Relativistic Rapidly Rotating Iron Core Collapse. *Phys. Rev. D*, 86:024026, 2012. doi: 10.1103/PhysRevD.86.024026.
- [216] H. T. Janka and E. Müller. Neutrino heating, convection, and the mechanism of Type-II supernova explosions. *aap*, 306:167, February 1996.
- [217] Ue-Li Pen, Phil Arras, and ShingKwong Wong. A free, fast, simple and efficient tvd mhd code. *Astrophys. J. Suppl.*, 149:447, 2003. doi: 10.1086/378771.
- [218] Takami Kuroda, Tomoya Takiwaki, and Kei Kotake. A New Multi-Energy Neutrino Radiation-Hydrodynamics Code in Full General Relativity and Its Application to Gravitational Collapse of Massive Stars. *Astrophys. J. Suppl.*, 222(2):20, 2016. doi: 10.3847/0067-0049/222/2/20.
- [219] Takami Kuroda, Kei Kotake, Kazuhiro Hayama, and Tomoya Takiwaki. Correlated signatures of gravitational-wave and neutrino emission in three-dimensional general-relativistic core-collapse supernova simulations. *The Astrophysical Journal*, 851(1):62, dec 2017. doi: 10.3847/1538-4357/aa988d. URL <https://doi.org/10.3847/1538-4357/aa988d>.
- [220] Ken-ichi Oohara, Takashi Nakamura, and Masaru Shibata. Chapter 3. A Way to 3D Numerical Relativity. *Progress of Theoretical Physics Supplement*, 128:183–249, January 1997. doi: 10.1143/PTPS.128.183.

- [221] Lee Samuel Finn and Charles R. Evans. Determining gravitational radiation from Newtonian self-gravitating systems. *apj*, 351:588–600, March 1990. doi: 10.1086/168497.
- [222] Michele Maggiore. *Gravitational Waves. Vol. 1: Theory and Experiments*. Oxford Master Series in Physics. Oxford University Press, 2007. ISBN 978-0-19-857074-5, 978-0-19-852074-0.
- [223] M. J. Szczepańczyk and C. D. Ott. Expressing gravitational waves energy in terms of quadrupole moment. Technical Report LIGO-T1500586, November 2015. URL <https://dcc.ligo.org/LIGO-T1500586>.
- [224] Eanna E. Flanagan and Scott A. Hughes. Measuring gravitational waves from binary black hole coalescences: 1. Signal-to-noise for inspiral, merger, and ringdown. *Phys. Rev. D*, 57:4535–4565, 1998. doi: 10.1103/PhysRevD.57.4535.
- [225] B.P. Abbott et al. Optically targeted search for gravitational waves emitted by core-collapse supernovae during the first and second observing runs of advanced LIGO and advanced Virgo. *Phys. Rev. D*, 101(8):084002, 2020. doi: 10.1103/PhysRevD.101.084002.
- [226] R. Abbott et al. Noise curves used for Simulations in the update of the Observing Scenarios Paper. Technical Report LIGO-T2000012, February 2020. URL <https://dcc.ligo.org/LIGO-T2000012/public>.
- [227] R. Abbott et al. Unofficial sensitivity curves (ASD) for aLIGO, Kagra, Virgo, Voyager, Cosmic Explorer, and Einstein Telescope. Technical Report LIGO-T1500293, January 2020. URL <https://dcc.ligo.org/LIGO-T1500293/public>.
- [228] R. Abbott et al. H1 Calibrated Sensitivity Spectra Jun 10 2017 (Representative Best of O2 – C02, With Cleaning/Subtraction). Technical Report LIGO-G1801950, September 2018. URL <https://dcc.ligo.org/LIGO-G1801950/public>.
- [229] Pietro Antonioli, Richard Tresch Fienberg, Fabrice Fleuret, Yoshiyuki Fukuda, Walter Fulgione, Alec Habig, Jaret Heise, Arthur B McDonald, Corrinne Mills, Toshio Namba, Leif J Robinson, Kate Scholberg, Michael Schwendener, Roger W Sinnott, Blake Stacey, Yoichiro Suzuki, Réda Tafirout, Carlo Vigorito, Brett Viren, Clarence Virtue, and Antonino Zichichi. Snews: the supernova early warning system. *New Journal of Physics*, 6(1):114, 2004. URL <http://stacks.iop.org/1367-2630/6/i=1/a=114>.
- [230] G. Pietrzyński, D. Graczyk, A. Gallenne, W. Gieren, I. B. Thompson, B. Pilecki, P. Karczmarek, M. Górski, K. Suchomska, M. Taormina, B. Zgirski, P. Wielgórski, Z. Kołaczowski, P. Konorski, S. Villanova, N. Nardetto, P. Kervella, F. Bresolin, R. P. Kudritzki, J. Storm, R. Smolec, and W. Narloch. A distance to the Large Magellanic Cloud that is precise to one per cent. *nat*, 567(7747):200–203, March 2019. doi: 10.1038/s41586-019-0999-4.

- [231] S. E. Gossan, P. Sutton, A. Stuver, M. Zanolin, K. Gill, and C. D. Ott. Observing Gravitational Waves from Core-Collapse Supernovae in the Advanced Detector Era. *Phys. Rev. D*, 93(4):042002, 2016. doi: 10.1103/PhysRevD.93.042002.
- [232] Conrad Chan, Bernhard Müller, Alexander Heger, Rüdiger Pakmor, and Volker Springel. Black hole formation and fallback during the supernova explosion of a $40 M_{\odot}$ star. *Astrophys. J. Lett.*, 852(1):L19, 2018. doi: 10.3847/2041-8213/aaa28c.
- [233] Kuo-Chuan Pan, Matthias Liebendörfer, Sean M. Couch, and Friedrich-Karl Thielemann. Equation of State Dependent Dynamics and Multi-messenger Signals from Stellar-mass Black Hole Formation. *Astrophys. J.*, 857(1): 13, 2018. ISSN 0004-637X. doi: 10.3847/1538-4357/aab71d. URL <http://dx.doi.org/10.3847/1538-4357/aab71d>.
- [234] Kuo-Chuan Pan, Matthias Liebendörfer, Sean Couch, and Friedrich-Karl Thielemann. Stellar Mass Black Hole Formation and Multi-messenger Signals from Three Dimensional Rotating Core-Collapse Supernova Simulations. 2020. URL <http://arxiv.org/abs/2010.02453>.
- [235] B. P. Abbott et al. Observation of gravitational waves from a binary black hole merger. *Phys. Rev. Lett.*, 116:061102, Feb 2016. doi: 10.1103/PhysRevLett.116.061102. URL <https://link.aps.org/doi/10.1103/PhysRevLett.116.061102>.
- [236] The LIGO Scientific Collaboration, the Virgo Collaboration, and the KAGRA Collaboration. GWTC-3: Compact Binary Coalescences Observed by LIGO and Virgo During the Second Part of the Third Observing Run. *arXiv e-prints*, art. arXiv:2111.03606, November 2021.
- [237] Kentaro Somiya, Yoichi Aso, Yuta Michimura, and Masaki Ando. *Phys. Rev. D*, 88, 2013. URL <https://journals.aps.org/prd/abstract/10.1103/PhysRevD.88.043007>.
- [238] B. Iyer et al. LIGO-India, Proposal of the Consortium for Indian Initiative in Gravitational-wave Observations (IndIGO). Technical Report LIGO-M1100296-v2, IndIGO and LIGO Scientific Collaboration, 2011. URL <https://dcc.ligo.org/cgi-bin/DocDB/ShowDocument?docid=75988>.
- [239] A. M. Soderberg, S. R. Kulkarni, E. Nakar, E. Berger, P. B. Cameron, D. B. Fox, D. Frail, A. Gal-Yam, R. Sari, S. B. Cenko, M. Kasliwal, R. A. Chevalier, T. Piran, P. A. Price, B. P. Schmidt, G. Pooley, D.-S. Moon, B. E. Penprase, E. Ofek, A. Rau, N. Gehrels, J. A. Nousek, D. N. Burrows, S. E. Persson, and P. J. McCarthy. Relativistic ejecta from X-ray flash XRF 060218 and the rate of cosmic explosions. *nat*, 442:1014, August 2006. doi: 10.1038/nature05087.
- [240] M. Punturo et al. The Einstein Telescope: a third-generation gravitational wave observatory. *Class. Quantum Grav.*, 27:194002, October 2010. doi: 10.1088/0264-9381/27/19/194002.

- [241] E. Berti, V. Cardoso, and C. M. Will. On gravitational-wave spectroscopy of massive black holes with the space interferometer LISA. *Phys. Rev. D*, 73:064030, 2006.
- [242] Reed Essick, Will M. Farr, Maya Fishbach, Daniel E. Holz, and Erik Katsavounidis. (An)isotropy measurement with gravitational wave observations. *Phys. Rev. D*, 107(4):043016, 2023. doi: 10.1103/PhysRevD.107.043016.
- [243] Toshiya Namikawa. Analyzing clustering of astrophysical gravitational-wave sources: Luminosity-distance space distortions. *JCAP*, 01:036, 2021. doi: 10.1088/1475-7516/2021/01/036.
- [244] Ethan Payne, Sharan Banagiri, Paul Lasky, and Eric Thrane. Searching for anisotropy in the distribution of binary black hole mergers. *Phys. Rev. D*, 102(10):102004, 2020. doi: 10.1103/PhysRevD.102.102004.
- [245] B. P. Abbott et al. A Gravitational-wave Measurement of the Hubble Constant Following the Second Observing Run of Advanced LIGO and Virgo. *Astrophys. J.*, 909(2):218, 2021. doi: 10.3847/1538-4357/abdc67.
- [246] R. Abbott et al. Constraints on the cosmic expansion history from GWTC-3. 11 2021.
- [247] John Baker et al. High angular resolution gravitational wave astronomy. *Exper. Astron.*, 51(3):1441–1470, 2021. doi: 10.1007/s10686-021-09712-0.
- [248] Alexander C. Jenkins, Mairi Sakellariadou, Tania Regimbau, and Eric Slezak. Anisotropies in the astrophysical gravitational-wave background: Predictions for the detection of compact binaries by LIGO and Virgo. *Phys. Rev. D*, 98(6):063501, 2018. doi: 10.1103/PhysRevD.98.063501.
- [249] Alexander C. Jenkins, Richard O’Shaughnessy, Mairi Sakellariadou, and Daniel Wysocki. Anisotropies in the astrophysical gravitational-wave background: The impact of black hole distributions. *Phys. Rev. Lett.*, 122(11):111101, 2019. doi: 10.1103/PhysRevLett.122.111101.
- [250] Alexander C. Jenkins and Mairi Sakellariadou. Shot noise in the astrophysical gravitational-wave background. *Phys. Rev. D*, 100(6):063508, 2019. doi: 10.1103/PhysRevD.100.063508.
- [251] Daniele Bertacca, Angelo Ricciardone, Nicola Bellomo, Alexander C. Jenkins, Sabino Matarrese, Alvise Raccanelli, Tania Regimbau, and Mairi Sakellariadou. Projection effects on the observed angular spectrum of the astrophysical stochastic gravitational wave background. *Phys. Rev. D*, 101(10):103513, 2020. doi: 10.1103/PhysRevD.101.103513.
- [252] Nicola Bellomo, Daniele Bertacca, Alexander C. Jenkins, Sabino Matarrese, Alvise Raccanelli, Tania Regimbau, Angelo Ricciardone, and Mairi Sakellariadou. CLASS.GWB: robust modeling of the astrophysical gravitational wave background anisotropies. *JCAP*, 06(06):030, 2022. doi: 10.1088/1475-7516/2022/06/030.

- [253] Gregory Ashton, Moritz Hübner, Paul D. Lasky, Colm Talbot, Kendall Ackley, Sylvia Biscoveanu, Qi Chu, Atul Divakarla, Paul J. Easter, Boris Goncharov, Francisco Hernandez Vivanco, Jan Harms, Marcus E. Lower, Grant D. Meadors, Denyz Melchor, Ethan Payne, Matthew D. Pitkin, Jade Powell, Nikhil Sarin, Rory J. E. Smith, and Eric Thrane. BILBY: A User-friendly Bayesian Inference Library for Gravitational-wave Astronomy. *The Astrophysical Journal Supplement*, 241(2):27, April 2019. doi: 10.3847/1538-4365/ab06fc.
- [254] I M Romero-Shaw, C Talbot, S Biscoveanu, V D’Emilio, and et al Ashton. Bayesian inference for compact binary coalescences with bilby: validation and application to the first LIGO–Virgo gravitational-wave transient catalogue. *Monthly Notices of the Royal Astronomical Society*, 499(3):3295–3319, 09 2020. ISSN 0035-8711. doi: 10.1093/mnras/staa2850. URL <https://doi.org/10.1093/mnras/staa2850>.
- [255] Gregory Ashton et al. BILBY: A user-friendly Bayesian inference library for gravitational-wave astronomy. *Astrophys. J. Suppl.*, 241(2):27, 2019. doi: 10.3847/1538-4365/ab06fc.
- [256] G. Hinshaw, D. N. Spergel, L. Verde, R. S. Hill, S. S. Meyer, C. Barnes, C. L. Bennett, M. Halpern, N. Jarosik, A. Kogut, E. Komatsu, M. Limon, L. Page, G. S. Tucker, J. L. Weiland, E. Wollack, and E. L. Wright. First-year wilkinson microwave anisotropy probe (wmap)* observations: The angular power spectrum. *The Astrophysical Journal Supplement Series*, 148(1):135, sep 2003. doi: 10.1086/377225. URL <https://dx.doi.org/10.1086/377225>.
- [257] Stefano Camera, José Fonseca, Roy Maartens, and Mário G. Santos. Optimized angular power spectra for spectroscopic galaxy surveys. *Mon. Not. Roy. Astron. Soc.*, 481(1):1251–1261, 2018. doi: 10.1093/mnras/sty2284.
- [258] Matias Zaldarriaga and Uros Seljak. Gravitational lensing effect on cosmic microwave background polarization. *Phys. Rev. D*, 58:023003, 1998. doi: 10.1103/PhysRevD.58.023003.
- [259] Marco Cavaglia and Ashini Modi. Two-dimensional correlation function of binary black hole coalescences. *Universe*, 6(7):93, 2020. doi: 10.3390/universe6070093.
- [260] Martin White, Douglas Scott, and Joseph I. Silk. Anisotropies in the cosmic microwave background. *Annual Review of Astronomy and Astrophysics*, 32:319–370, 1994.
- [261] Colm Talbot and Eric Thrane. Measuring the binary black hole mass spectrum with an astrophysically motivated parameterization. *The Astrophysical Journal*, 856(2):173, apr 2018. doi: 10.3847/1538-4357/aab34c. URL <https://doi.org/10.3847/1538-4357/aab34c>.
- [262] Colm Talbot and Eric Thrane. Determining the population properties of spinning black holes. *prd*, 96(2):023012, July 2017. doi: 10.1103/PhysRevD.96.023012.

- [263] Daniel Wysocki, Jacob Lange, and Richard O’Shaughnessy. Reconstructing phenomenological distributions of compact binaries via gravitational wave observations. *prd*, 100(4):043012, August 2019. doi: 10.1103/PhysRevD.100.043012.
- [264] Maya Fishbach, Daniel E. Holz, and Will M. Farr. Does the black hole merger rate evolve with redshift? *The Astrophysical Journal*, 863(2):L41, aug 2018. doi: 10.3847/2041-8213/aad800. URL <https://doi.org/10.3847/2041-8213/aad800>.
- [265] Derek Davis et al. LIGO detector characterization in the second and third observing runs. *Class. Quant. Grav.*, 38(13):135014, 2021. doi: 10.1088/1361-6382/abfd85.
- [266] Mark Hannam, Patricia Schmidt, Alejandro Bohé, Leila Haegel, Sascha Husa, Frank Ohme, Geraint Pratten, and Michael Pürrer. Simple Model of Complete Precessing Black-Hole-Binary Gravitational Waveforms. *prl*, 113(15):151101, October 2014. doi: 10.1103/PhysRevLett.113.151101.
- [267] Patricia Schmidt, Frank Ohme, and Mark Hannam. Towards models of gravitational waveforms from generic binaries: II. modelling precession effects with a single effective precession parameter. *Phys. Rev. D*, 91:024043, Jan 2015. doi: 10.1103/PhysRevD.91.024043. URL <https://link.aps.org/doi/10.1103/PhysRevD.91.024043>.
- [268] Joshua S. Speagle. DYNesty: a dynamic nested sampling package for estimating Bayesian posteriors and evidences. *mnras*, 493(3):3132–3158, April 2020. doi: 10.1093/mnras/staa278.
- [269] Allen Craig Robert Hogg, Joseph McKean. *Introduction to Mathematical Statistics*. Pearson, 2012.
- [270] Linqing Wen and Yanbei Chen. Geometrical expression for the angular resolution of a network of gravitational-wave detectors. *Phys. Rev. D*, 81:082001, Apr 2010. doi: 10.1103/PhysRevD.81.082001. URL <https://link.aps.org/doi/10.1103/PhysRevD.81.082001>.
- [271] William G. Cochran. The χ^2 test of goodness of fit. *The Annals of Mathematical Statistics*, 23(3):315–345, 1952. ISSN 00034851. URL <http://www.jstor.org/stable/2236678>.
- [272] Martin White, Douglas Scott, and Joseph Silk. Anisotropies in the cosmic microwave background. *Annual Review of Astronomy and Astrophysics*, 32(1):319–370, 1994. doi: 10.1146/annurev.aa.32.090194.001535. URL <https://doi.org/10.1146/annurev.aa.32.090194.001535>.
- [273] Y. Wang, R. J. Brunner, and J. C. Dolence. The SDSS Galaxy Angular Two-Point Correlation Function. *Mon. Not. Roy. Astron. Soc.*, 432:1961, 2013. doi: 10.1093/mnras/stt450.

- [274] R. Abbott et al. Search for anisotropic gravitational-wave backgrounds using data from Advanced LIGO and Advanced Virgo's first three observing runs. *Phys. Rev. D*, 104(2):022005, 2021. doi: 10.1103/PhysRevD.104.022005.
- [275] R. Abbott et al. All-sky, all-frequency directional search for persistent gravitational waves from Advanced LIGO's and Advanced Virgo's first three observing runs. *Phys. Rev. D*, 105(12):122001, 2022. doi: 10.1103/PhysRevD.105.122001.
- [276] Arianna I. Renzini, Joseph D. Romano, Carlo R. Contaldi, and Neil J. Cornish. Comparison of maximum-likelihood mapping methods for gravitational-wave backgrounds. *Phys. Rev. D*, 105(2):023519, 2022. doi: 10.1103/PhysRevD.105.023519.
- [277] Ken K. Y. Ng, Salvatore Vitale, Will M. Farr, and Carl L. Rodriguez. Probing multiple populations of compact binaries with third-generation gravitational-wave detectors. *Astrophys. J. Lett.*, 913(1):L5, 2021. doi: 10.3847/2041-8213/abf8be.

VITA

In December 2023, Yanyan Zheng received her doctoral degree in Physics from Missouri University of Science and Technology. She worked under the supervision of Dr. Marco Cavaglià on gravitational-wave detections. Before embarking on her Ph.D., Yanyan honed her expertise in Optical Engineering, earning her Master's degree from Shantou University in China. Her foundational education in Physics was acquired at Liaocheng University, in China, where she completed her Bachelor's degree.